Texture Modeling: Temperature Effects on Markov/Gibbs Random Fields

by

Rosalind Wright Picard

B.E.E., Georgia Institute of Technology (1984)
M.S., Massachusetts Institute of Technology (1986)

Submitted to the Department of Electrical Engineering and Computer Science
in partial fulfillment of the requirements for the degree of

Doctor of Science

at the

MASSACHUSETTS INSTITUTE OF TECHNOLOGY

June 1991

Signature redacted

Author .....
Department of Electrical Engineering and Computer Science
May 15, 1991

Signature redacted

Certified by .....
Alex P. Pentland
Associate Professor, M.I.T. Media Laboratory
Thesis Supervisor

Signature redacted

Accepted by .....
Arthur C. Smith
Chairman, Departmental Committee on Graduate Students

Texture Modeling: Temperature Effects on Markov/Gibbs Random Fields

by
Rosalind Wright Picard

Submitted to the Department of Electrical Engineering and Computer Science
on May 15, 1991, in partial fulfillment of the
requirements for the degree of
Doctor of Science

Abstract

Temperature is a key parameter in the original physical formulation of the Markov/Gibbs random field (MRF) model; however, it has been neglected in most applications of these models to image processing and computer vision. This thesis studies the effect of temperature on texture and develops new characterizations of textures that are synthesized with the MRF. The main contributions are as follows:

- We develop a new "aura" framework which describes the neighborhood dependency of the MRF as morphological dilation. The "aura matrix" is used to write the Gibbs energy as a linear combination of its co-occurrence matrices; this is the first time that an MRF has been shown to be specified by a set of its co-occurrences.
- A new interpretation of MRF pattern formation based on the physical mechanisms of mixing and separation is presented. For small neighborhoods we relate this mechanism to boundary length optimization. These results generalize the boundary length behavior known to characterize the Ising model of statistical mechanics.
- New relationships between graylevel, temperature, and MRF equilibrium are identified. These indicate that many of the textures in the literature may have not been in equilibrium. In particular, increasing the number of graylevels behaves similarly to lowering the temperature; both require longer times to reach equilibrium.
- We derive a new interpretation of the MRF bonding parameters as annealing rate constants which control the graylevel mixing and separation in different directions.
- Aura matrix features (related to co-occurrence features) are shown to exhibit temperature dependent behavior similar to a phase transition.
- The idea of "transition temperature," analogous to critical temperature, is developed for an MRF texture. The peaked region of the specific heat is related to the bandwidth transitions of the aura matrix.
- We develop the first characterization of texture produced by an MRF in its ground state. The result shows how energy minimization for an MRF may restrict the model from producing large and important classes of natural textures.

Thesis Supervisor: Alex P. Pentland
Title: Associate Professor, M.I.T. Media Laboratory

Acknowledgments

Tis done tis done! At last it's time to say where credit's due,
For I might not have finished this if it were not for you:

First I want to thank Pentland – above all for his caring;
He's pulled for me, shared bright ideas, and shown understanding.
With balance, breadth, and insight that's the best I've ever seen,
He's helped me sort my good from bad, and reach this once mere dream.

To my readers – Lim and Mitter – I owe you both a lot;
You've asked me what's important, redirecting random thought.
Lim has shown enduring kindness, and has let me run free;
Mitter's emphasis on physics and rigor challenged me.

'Twas Musicus inspired me to make this expedition.
Oppenheim gave wise advice at points of phase transition.

Deb and Cindy often E-mailed a cheerful thought my way;
Friendship, warmth and sharing came from Michelle and Avideh.
To all the folks who were a part of the DSPG,
Especially Steve, Jim, and Mike, for their comradery.

I am indebted to the Media Lab and Vismod–
Their acceptance nonpareil, though my ideas often odd.
Lots of smiles and support have come from Laureen and from Bea,
And friendly interaction from Dave, Martin, and Bradley.

Thanks to Ted and to Eero for helpful and fine advice,
Stephen for questions, Trevor for making the systems nice,
And for lots of good discussions, also Bill and Matthew,
Stanzi, John, Stan and Irfan – I'm impressed by all of you.

With Elfadel it's been my privilege to collaborate,
O'er sonnets, fields, and patterns do our ideas percolate;
Inshallah, may our friendship endure the changing weather.
To Wyatt – for kind interest, and bringing us together.

To Yong Li and Roland Netz for talks of gels and physics;
To Adriaan and friends at Bell who've warmed all my visits.

To best friends in Boston – Cheryl, Beth, Sarah, Don, Barry,
GCF friday group, especially Hojoon and Mary.
Park Street and Paulist folks have challenged me to grow within,

Unselfishly they've shared with me and become "God in Skin."

There are dear friends who, although far, have had lasting impact.
They have cheered me and pulled off more than one Southern "CLLAST" act.
Thanks to Charlene's dear friendship and Dr. Lisa's phone calls,
Lynda, Anita, Sarah, Teresa, and Betsy – "all y'all."

And finally, let all praise be to our God who knows all things,
Including vision, all our needs, and what the future brings.

> "For now we see as through a glass, dimly, but then face to face.
> Now I know in part, but then I shall know fully,
> even as I have been fully known." 1 Corinthians 13:12

This research was supported in part by the National Science Foundation under Grant Nos. MIP 87-14969 and IRI-8719920, in part by the Defense Advanced Research Projects Agency (DARPA) monitored by the Office of Naval Research under Grant No. N00014-89-J-1489, and in part by the Rome Air Development Center (RADC) of the Air Force System Command and DARPA under contract No. F30602-89-C-0022.

Dedicated to
my great great uncle,
Dillon O. Raffo
9/3/93 - 2/7/90
who was inventive, curious,
joyful, full of charity,
wanted to learn about black holes at age 93,
reminded me often of the size of the universe,
to keep things in perspective,
and of the Omniscience behind it all;

and

to my beloved and supportive family
and imaginative, loving, fun, and patient husband,
Len,
with all my love

Contents

Chapter 1

Introduction

1.1 What is texture?

Texture is ubiquitous; it is felt on the tiny surface of a shriveled pea, can be heard in the interwoven melodies of a fugue, and is a visual hallmark of deconstructivist architecture. Eluding precise definition, texture is distinguished by being tactile, patterned, rhythmic, or noisy.

Images are full of texture – everyone agrees on this; but, there is little agreement on what exactly defines a texture. An idea from studies of early vision is helpful in characterizing texture. These studies emphasize the measurement of various image properties such as orientation, color and motion – "stuff" that involves a collective measurement as opposed to "things" like objects with form and a name [1]. Texture tends to be a "stuff" problem – a weave of fibers, the pattern of windows on a tall skyscraper, a suspension of particles, even the motion of a colorful cheering crowd.

It is generally an ill-posed problem to say "find the texture in this picture." Texture eludes precise definition. In images it has been suggested that texture generally has the following properties. First, texture does not contain a lot of specific information; there should exist more efficient representations for it. Second, texture usually contains high frequencies – especially edges of primitive structuring elements or random components. The third basic property is shift invariance; two textures can be visually the same and yet differ in every position. Fourth, texture exists only over

a certain range of scale, e.g., at long distance the brick wall is smooth red; closer it is a regular staggered pattern; under the microscope it is a rugged terrain. It often exhibits some form of similarity over this range of scale.

Typical texture property: low information content

The first property is illustrated by considering the following three sequences:

YippeeYippeeYippeee

sh ysSTehtignaSio m

This Says Something

The first is analogous to a periodic texture. It has a basic primitive, a set of rules for replication of the primitive, and allowance for some minor perturbation. It may take a lot of information to represent the primitive, but this is averaged out over the whole pattern and the net information is low. Regular patterns like this show up in physical materials such as nylon and crystals.

The second sequence is analogous to a stochastic texture generated with a random number generator or filtered noise; again, it takes little information to model a random sequence. Nature's examples are random polymers and nucleic acids.

The third sequence, like the structure of DNA and proteins, is distinguished by its specific ordering. Although it is an anagram of the second, its specificity gives it a lot more information.

The first two sequences are 1-D versions of texture, distinguished by having relatively little information content. In fact 2-D textures are popularly grouped into categories corresponding to the first two sequences – "regular and random" , or "structural and statistical" [29]. The "stuff" analogy for texture also works for the first two sequences. They can be characterized by the substance that comprises them – the primitive "Yippee" or a random letter. The third pattern fits the "thing" characterization – it is not merely a string of letters or primitives, but it is a specific ordering

that makes a sentence, a complete thought.

Typical texture properties: high frequency and shift invariance

The first property indicates that there should be a more efficient model for representing texture. The second and third properties of texture, however, make texture a nemesis to most traditional image models. For example, standard image coding methods assume that the image data is highly correlated and dominated by low frequency information; hence, textures are not compressed efficiently. Moreover, the most common optimality criterion in image coding is pixel mean squared error which is not at all appropriate for comparing two textures given their second property.

Similarly, implicit in many image models for computer vision is the assumption of the image as a piecewise constant, e.g., Mondrian-style painting, where regions are smooth and separated by definite boundaries. The presence of edges within a texture ruins the ability of these models to treat the texture as one region.

Typical texture property: scaling

The theme of scale as the fourth property of textures is exemplary in the work of Mandelbrot [40] who emphasizes the presence of self-similarity over scale as a feature of fractals. Pentland [50] showed that a fractal model was able to distinguish between certain kinds of textures and smooth regions in an image, and Peleg *et. al.* [49] used scaling properties for texture discrimination. In some kinds of random textures, e.g. fractal Brownian motion, there is statistical self-similarity over all scales. In many textures, there is only self-similarity or self-affinity over a discrete number of scales.

Self-similarity is of course related to redundancy and reduced information. Its presence indicates that there is something fundamental that can be extracted from a texture, and which can be used to succinctly model it.

Scaling similarity shows up in another way – across patterns at different scales. In his delightful book on patterns in nature, Stevens [59] shows pictures of a variety of phenomenon over different scales that produce similar texture patterns: gas clouds and milk poured into a black slate sink, a box turtle shell and a regular cluster of

bubbles. These are all different materials and different scales, but they all share something that allows them to produce visually similar patterns. Stevens examines many of the common behaviors of natural patterns, including close packing, spirals, branching, shrinking surfaces, and turbulence.

1.2 Markov/Gibbs random field texture modeling

One ideal goal for texture modeling then is to find all the "basic pattern mechanisms" that operate in the space of natural patterns and develop ways to control them. This lofty aim is not new – it is alive in biological morphogenesis, non-equilibrium thermodynamics, and a host of material studies. We will certainly not solve it here! However, with it as inspiration, we undertake the study of a model that is very versatile and which lies in a space that can theoretically contain any pattern – the Markov/Gibbs random field model (MRF).

Unlike most texture models, the MRF is capable of generating random, regular, and even highly structured patterns. It does not just describe some characteristics for distinguishing textures, but it can be used for both texture analysis and synthesis.

The MRF has simultaneous roots in the Gibbs distribution of statistical mechanics and the Markov models of probability. The Gibbs distribution has a rich history of applications in physics including the modeling of lattice gases, molecular interactions in magnets, and ordering processes in condensed matter. In computer vision and image processing, the MRF is touted for its ability to relate the Markov conditional probabilities to the Gibbs joint probability. It can be easily incorporated into a Bayesian framework.

Hassner and Sklansky [30] appear to have been the first to suggest the use of Markov/Gibbs models for image texture. Cross and Jain [16, 17] conducted the first explorations of the MRF for graylevel texture modeling and showed that it generated random natural textures well. A Gaussian MRF was applied to texture classification and modeling by Chellappa and Chatterjee [9, 10] and Cohen *et. al.* [13].

Though mostly used for statistical textures, the MRF has also been combined with low frequency Fourier information to successfully model clouds which include both structural and statistical components [26]. As part of a Bayesian framework, the MRF has been used primarily as a prior statistical model for image restoration and segmentation [64, 27, 38, 12, 19, 43, 70, 6, 34], and image estimation [34]. The flexibility of the MRF has also been exploited to combine texture, stereo, motion and color for labeling discontinuities [25]. An excellent review of the use of the MRF in image analysis can be found in Dubes and Jain [20].

The MRF is able to combine local internal interactions with global external influences. The interplay between microscopic dynamics and macroscopic force, such as that associated with a phase transition is an important factor in natural pattern formation [3].

1.3 Temperature and texture

In applications to images the physical origins of the MRF have been noted but not directly considered. The concept of temperature has been used with MRF's as part of simulated annealing, a Monte Carlo optimization method which uses temperature to sort out things according to scale [37]. However, the effect of the temperature on the underlying texture has not been explicitly studied.

It is instructive to begin by considering examples of texture formation in real materials before examining the role of temperature in MRF's. We mention two physical situations where temperature is important for pattern formation. Analogies will be made to these at appropriate points during the thesis.

Crystallization

Temperature is an important control in chemistry for purifying substances and forming crystals. Two basic principles are at work in this process that we will see later with MRF's.

The first principle takes advantage of the different solubilities of substances at

different temperatures. At high temperature all substances are dissolved. As the temperature is lowered, different substances precipitate out of solution and form crystals. Temperature is useful for regulating the separation of different substances [44].

The second principle involves the formation of a *regular* crystal. At high temperatures, molecules are free to move any distance; they mix easily. At some low temperature, the desired crystalline substance begins to solidify. To obtain a pure regular crystal the lowering of temperature in this range must proceed very slowly, spending lots of time where the molecules can make adjustments at small scales.

Gel pattern formation

Gels exhibit many useful properties; these have led to diverse applications such as drug capsules, prosthetics, polymer separation, and diaper wetness control. In addition, Tanaka *et. al.* have shown that beautiful patterns form on the gel as it undergoes extensive swelling.

The gel is smooth when it is initially placed in a petri dish and immersed in water. As the gel soaks up water it expands and an extremely fine pattern forms on its surface. The unit size of the pattern increases with time and swelling. Eventually, the gel reaches equilibrium where it is a smooth swollen ball and the pattern has completely disappeared. This final equilibrium state, devoid of all texture, is its minimum energy state.

In this example the formation of patterns is a characteristic of the *non-equilibrium* states and not of the lowest energy state. In the vision research literature, however, texture research using MRF's has been conceptualized as the study of the minimum energy states. As this example shows, interesting natural patterns can be missed if only minimum energy states are studied.

There is another principle at work in the gel pattern formation that we will also see in the MRF: a certain temperature is required before any distinct patterns appear. Actually, the swelling and pattern formation can be regulated by a number of factors: ionization, voltage, pH level, and enzyme content are other possibilities. We will see analogies to these behaviors in the MRF.

1.4 Thesis overview and contributions

Although temperature has been used with MRF's in Bayesian optimization, this thesis appears to be the first direct study of temperature on texture formation. The basic framework of MRF's and of their use for texture modeling is given in Chapter 2. The basics of MRF texture analysis and synthesis, as well as many common assumptions made when using the model will also be discussed.

The first new contributions of this thesis are in Chapter 3. There we establish some new relations between the MRF model, mathematical morphology, and co-occurrence matrices. The co-occurrence relation is particularly interesting because co-occurrences and MRF's are often cited in the same paper, and always treated as two different methods. These relationships are the consequence of a new notational "aura" framework, developed jointly with I. M. Elfadel. This framework also allows the energy function of the MRF to be written in a new way that is more useful for some applications. Chapter 3 also introduces the new physically-motivated miscibility and boundary minimization interpretations of the MRF behavior. These generalize the previously known boundary length behavior for a binary MRF.

Chapter 4 begins the study of the effects of temperature on MRF texture formation. We show several behaviors to indicate that the MRF bonding parameters do not characterize a texture as previously implied in the literature. Using the aura framework we derive a new interpretation of the bonding parameters as annealing rate constants. We proceed to develop a characterization of several features of the aura matrix and Gibbs energy at different temperatures. This characterization is especially important for patterns not at zero temperature, i.e., patterns which are not in their minimum energy configuration.

The temperature characterization problem is complicated by the nonlinearity of the model's dependence on temperature. In particular, we show that there are regions where the model undergoes abrupt changes which have an analogy to phase transitions. In Chapter 5 we mark these points by their "transition temperatures" and show evidence that suggests multiple transitions for graylevel textures. We also

suggest a new method based on the aura matrix for characterizing these points of transition. The new method is compared to a method from physics which uses the specific heat of the field. We also describe the transition temperatures as the points where different substances precipitate out of solution; we make a new analogy between this behavior and crystallization.

The MRF texture undergoes a process of energy minimization during synthesis which is analogous to the surface minimization that often occurs in natural pattern formation. The minimum energy pattern, or ground state, is the solution to a difficult nonlinear optimization problem. In Chapter 6 we develop a new characterization of the ground state patterns by deriving the structure of the aura matrix as the energy is minimized. This structure has important new implications for the kinds of texture patterns that the MRF can model in its minimum energy state. In particular, we show that under reasonable assumptions, large classes of desirable patterns can *not* be represented by the ground state of an auto-binomial MRF.

With the new ability to characterize textural features at different temperatures, and with the new result showing severe limitations of ground state patterns, we argue for non-minimum energy and non-equilibrium texture formation. This is discussed in Chapter 7, along with a summary of the new contributions of the thesis.

Future research suggestions which relate to this work are provided in Chapter 8.

Chapter 2

Background: Markov/Gibbs texture modeling

2.1 Introduction

For texture modeling it is important to understand the basic framework of the Markov/Gibbs random field (MRF) model, the assumptions inherent in this framework, and the mechanics of synthesizing and analyzing the model parameters. This chapter gathers together the portion of this background information which is needed for this thesis.

Basic theory and notation for the Markov/Gibbs model are provided in Section 2.2. We also delineate the key assumptions typically made when using the model. Section 2.3 covers methods for the synthesis of MRF textures. The analysis of MRF's is only explained briefly in Section 2.4 as it does not bear directly on our results. I describe how the temperature and texture problem occurs in Bayesian optimization in Section 2.5.

2.2 Markov/Gibbs framework

2.2.1 Notation

Let an image be represented by a finite rectangular $M \times N$ lattice $\mathcal{S}$ with a neighborhood structure $\mathbf{N} = \{\mathcal{N}_s, s \in \mathcal{S}\}$ where $\mathcal{N}_s \subseteq \mathcal{S}$ is the set of sites which are neighbors of the site $s \in \mathcal{S}$. Every site has a graylevel value $x_s \in \Lambda = \{0, 1, \ldots, n-1\}$. Let $\mathbf{x}$ be the vector $(x_s, 1 \leq s \leq |\mathcal{S}|)$ of site graylevel values and Ω be the set of all configurations taken by $\mathbf{x}$. A neighborhood structure is said to be *symmetric* if $\forall s, r \in \mathcal{S}$, $s \in \mathcal{N}_r$ if and only if $r \in \mathcal{N}_s$.

For the finite periodic lattice $\mathcal{S}$ with a symmetric neighborhood structure $\mathbf{N}$, we define the Gibbs energy,

$$E(\mathbf{x}) = \sum_{s \in \mathcal{S}} V_s(x_s) + \sum_{s \in \mathcal{S}} \sum_{r \in \mathcal{N}_s} V_{sr}(x_s, x_r), \tag{2.1}$$

where the V_s's are the single-site potentials and the V_{sr}'s are the two-site potentials. In the physics literature the single-site potentials are called the *external field* while the two-site potentials define the interaction of the so-called *internal field.* To a Gibbs energy such as (2.1) we can assign a joint probability distribution, also called a measure, or a *random field*,

$$P(\mathbf{x}) = \frac{1}{Z} \exp\left(-\frac{1}{T} E(\mathbf{x})\right), \tag{2.2}$$

where Z is a positive normalizing constant known in the physics literature as a *partition function*[1] and T is the "temperature" of the field.

Technically, to make the right side unitless the T should be written as $k_B T$ where k_B is the Boltzmann constant having the units of entropy, $\mathbf{J/K°}$, and T has units $\mathbf{K°}$. As is conventional in the image processing and computer vision literature we absorb k_B into T and treat all the quantities as unitless.

[1] Z is a linear combination of terms having the same energy; hence, it *partitions* Ω into regions with the same energy.

Temperature

A precise definition of temperature is difficult since the definition must be formulated indirectly via the notion of equality of temperature. Two systems are said to have equal temperatures if there are no changes in their properties when they are brought into contact [39]. An example is when a hot and a cold body, both isolated from all other bodies, come into contact. Both bodies may undergo property changes. When all changes cease, the bodies are said to be in *thermal equilibrium*, i.e., there are no temperature gradients; the two systems have a common temperature.

To measure the temperature of a system, one needs the *Zeroth law of thermodynamics* which states that "if two systems are each equal in temperature to a third, they are equal in temperature to each other." Then, by reference to reproducible temperatures such as the ice point and steam point, the temperature of any system in thermal equilibrium can be determined.

Order and neighborhood

The MRF model is often defined by its *order*, p, which determines the neighborhood that the MRF depends on. Using terminology of mathematical morphology we will see that $\mathcal{N}_s$ functions as a *structuring element*. In Figure 2-1 (a) the neighborhoods corresponding to MRF's of orders $p = 1, 2, 3, 4$ are shown. These are the only orders used in this paper although extension to higher orders is straightforward.

Auto-binomial model

Different distributions can be obtained by specifying the potentials in (2.1). One popular choice, the auto-binomial model, was introduced as part of a class of "auto-models" by [5]. This is the model which has been most extensively studied for texture [16, 17, 26]. The auto-binomial model receives its name because its conditional probabilities are binomial. Its Gibbs energy is

$$E(\mathbf{x}) = -\sum_{s\in\mathcal{S}} \left(\alpha_s x_s + T \ln \left[\frac{(n-1)!}{x_s!(n-1-x_s)!} \right] + \sum_{r\in\mathcal{N}_s} \beta_{sr} x_s x_r \right), \qquad (2.3)$$

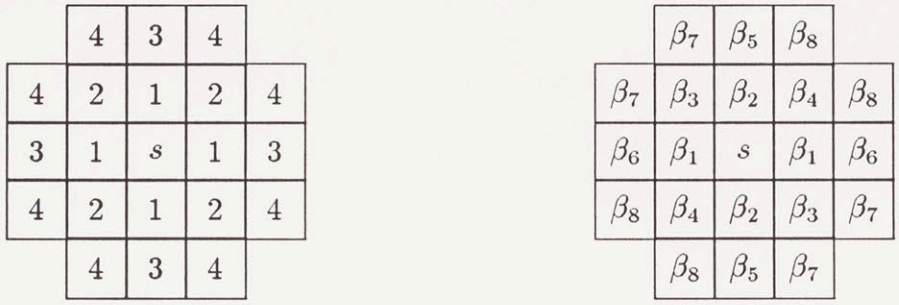

(a) (b)

Figure 2-1: (a) Neighbors of the site s for model orders 1-4. The neighborhood of order p contains all points with labels $\leq p$. (b) The auto-binomial bonding parameter β_k corresponding to each neighbor.

---

where the middle term comes from the binomial coefficient "$n-1$ choose x_s". In the homogeneous case $\alpha_s = \alpha$ (site-independent), and the auto-binomial *bonding parameters* $\beta_{sr} = \beta_r$ (site-independent but possibly dependent on the position of the neighbor). The bonding parameters are *isotropic* when $\beta_r = \beta$, $\forall\, r \in \mathcal{N}$. In Figure 2-1 (b) the auto-binomial "bonding parameter" which multiplies each neighbor is shown.

Potts model

Another popular energy function for general image processing [27, 19] is the homogeneous Potts model [72], for which

$$E(\mathbf{x}) = -\sum_{s\in\mathcal{S}} \left(\alpha_s x_s + \sum_{r\in\mathcal{N}_s} \beta_r (2\delta_{x_s x_r} - 1) \right), \tag{2.4}$$

where $\delta_{x_s x_r}$ is the Kronecker δ symbol. In the homogeneous isotropic case, the auto-binomial and Potts models are both equivalent to the Ising model of statistical mechanics.

Ising model

The energy function of the Ising model [32] is given for comparison purposes since it has the best studied temperature and boundary length behavior, and is a special case of the above two models. The Ising model has energy function,

$$E(\mathbf{x}) = -\sum_{s\in\mathcal{S}} \left(mH\sigma_s + \frac{J}{2} \sum_{|s-r|=1} \sigma_s\sigma_r \right), \tag{2.5}$$

where the $\sigma_s \in \{1, -1\}$, $\forall s \in \mathcal{S}$ are the "up and down spins", J and m are constants due to the material properties, and H is the intensity of an external magnetic field.

For the Ising model with $H = 0$, the partition function Z is solved analytically [2].

Subneighborhoods

It is helpful to define a *subneighborhood*, $\mathcal{N}_s^k \subset \mathcal{N}_s$ as the subset of neighbors having the same bonding parameter, β_k. Since each neighbor has only one bonding parameter, each neighborhood can be written as a union of disjoint subneighborhoods,

$$\mathcal{N}_s = \bigcup_{k=1}^{K} \mathcal{N}_s^k, \quad \text{and} \quad \mathcal{N}_s^k \cap \mathcal{N}_s^l = \emptyset, \ \ \forall l \neq k, \ \ \forall s \in \mathcal{S}. \tag{2.6}$$

Markov/Gibbs equivalence

From the Hammersley-Clifford theorem, we have the following result [5, 27].

Theorem 2.1 *Let* $\mathbf{N}$ *be a neighborhood system. Then* X *is an MRF with respect to* $\mathbf{N}$ *if and only if* $P(X)$ *is a Gibbs distribution with respect to* $\mathbf{N}$.

This result effectively relates the MRF conditional probability distributions to the Gibbs joint probability specification. We caution that the equivalence does not imply that every Gibbs distribution is an MRF, nor that every MRF is a Gibbs distribution.

For the $p = 1$ binary case Spitzer [57] gives a proof of this equivalence, along with equations which relate the parameters of the two models.

2.2.2 Assumptions

We make the standard assumptions for MRF's, but wish to do so explicitly. We also briefly discuss the significance of each assumption.

Pairwise cliques, auto-models

In the physics literature the summation in (2.1) is taken over the *cliques*. A clique, C, is a subset of the lattice for which each element of C is a neighbor of all the other elements of C. In the computer vision and image processing literature only cliques containing two elements have been studied. MRF's over these pairwise cliques are termed *auto*-models, e.g., auto-normal, auto-binomial, etc. [5].

The energy in (2.1) is the energy for any auto-model, where V_{sr} is defined to be equal to one half times the potential of the two-site clique, {s,r}. The restriction to using two-site cliques is similar to that of using second-order statistics. This thesis assumes auto-models, but the theoretical results can be extended to larger clique sizes in the same way that second order statistics can be extended to higher order ones.

Homogeneity and isotropy

As typical in the MRF literature we assume a homogeneous random field so that the model does not vary with position. Occasionally we will also assume isotropy so that the MRF parameters are all the same; this will be stated when it applies. Most natural textures are anisotropic. In most of the theory we present we are able to derive the anisotropic results from the isotropic case.

MRF neighborhoods

We assume use of the standard MRF neighborhoods as shown in Figure 2-1 (a). These neighborhoods are defined to be both symmetric and local. The notation we adopt in this thesis is extensible to *any* shape neighborhood, even non-local and disconnected neighborhoods. Some creative extensions are possible – but because of the many possible choices, and the non-linearity of the different possible neighborhoods,

the theory for *any* neighborhood rapidly becomes full of special cases. Though occasionally applicable to other neighborhoods, the results we develop in this thesis are only stated for the standard MRF neighborhoods.

Note that with the MRF neighborhoods a correspondence between order and *neighborhood width*, ω, is implied. For example, $\omega = 1$ for $p = 1, 2$, and $\omega = 2$ for $p = 3, 4$.

Lattice connectivity and periodic boundary

We represent an image as a lattice with each pixel corresponding to a node. When the image is modified only the values at lattice nodes may change. This representation implicitly assumes a connected lattice. We do not allow deformations or breaking of the lattice, both of which could happen in real-world 3-D texture formation, and to which the model could conceivably be extended.

A rectangular lattice with periodic boundary conditions is assumed. With this assumption the neighborhood $\mathcal{N}_s$ can be assumed to be site-independent and equal to the translate of a basic neighborhood, denoted $\mathcal{N}$. In this case the neighborhood size is constant, $|\mathcal{N}_s| = \nu$. If boundary conditions other than periodic are made then careful specification must be made for neighborhoods that intersect lattice boundaries. In particular, the size of the neighborhood will vary along the boundaries and will differ from the size of the inside neighborhoods.

Histograms, image and neighborhood sizes

Without any histogram constraints the optimum state of the MRF may have a trivial patternless solution. Although real textures can have any histogram we will often assume that the histogram is constrained to be uniform throughout the pattern formation. This assumption gives the maximum entropy prior distribution when nothing is known about the initial distribution.

We generally assume that the image size is large compared to both the neighborhood size and number of graylevels. These relative sizes are important in establishing how the different graylevels can configure.

2.3 Synthesis of Markov/Gibbs texture

We have implemented several different methods for synthesizing MRFs. The basic idea behind MRF texture synthesis is to find a sample of the MRF which globally minimizes the Gibbs energy. This can be posed as a nonlinear integer programming problem involving a search over $|\Omega|$ configurations. The minimization used here is based on a Monte Carlo algorithm. Monte Carlo methods can be divided into two categories: exchange and single-flip.

The basic difference between the two categories is as follows: In the exchange methods a new state is formed by "exchanging" pairs of values in the current state. No new values can be created and none are removed, they are only moved around. Thus, the system is "closed" – its histogram remains constant[2]. In contrast, the single-flip methods allow each site to take on any value in Λ. The system is "open" – its histogram will probably vary.

To reconcile the two categories, one can take the function that is being optimized by the open system and add to it a penalty function that constrains the histogram. The penalty function can then be increased so that the results of the single-flip and the exchange algorithms will be the same.

2.3.1 Exchange algorithms

The exchange algorithm we use is the Metropolis exchange which was introduced in [45], and used by [17, 26] for texture synthesis. This algorithm randomly selects two different lattice sites and computes the Gibbs energy for the lattice in its current state, E_1, and again in the state with the graylevels at the two sites exchanged, E_2. If $\Delta E = E_2 - E_1$ is the energy change, then the sites are exchanged with probability $\min(1, \exp[-\Delta E/T])$.

For the auto-binomial model synthesized with the Metropolis exchange, let the graylevels at the two sites, x_1 and x_2, be considered for swapping, and let $P(X)$ and

[2]A closed system in thermodynamics does not exchange mass with its surroundings, while an open system can.

$P(Y)$ be the distributions before and after the exchange respectively. The Metropolis algorithm evaluates

$$\frac{P(Y)}{P(X)} = \frac{\binom{n-1}{x_2} e^{\alpha_1 x_2 + x_2 \sum_{r \in \mathcal{N}_1} \beta_r x_r} \binom{n-1}{x_1} e^{\alpha_2 x_1 + x_1 \sum_{r \in \mathcal{N}_2} \beta_r x_r}}{\binom{n-1}{x_1} e^{\alpha_1 x_1 + x_1 \sum_{r \in \mathcal{N}_1} \beta_r x_r} \binom{n-1}{x_2} e^{\alpha_2 x_2 + x_2 \sum_{r \in \mathcal{N}_2} \beta_r x_r}}. \tag{2.7}$$

This ratio has the notable side effect of cancelling out all terms that appear as constants in the Gibbs energy function, in particular the binomial coefficients, and the external field if it is assumed to be homogeneous, i.e., $\alpha_s = \alpha$.

Since $\mathcal{N}$ is symmetric for an MRF, if $x_1 \in \mathcal{N}_2$, then $x_2 \in \mathcal{N}_1$. If the elements being exchanged are not in each other's neighborhoods, i.e., if $x_1 \notin \mathcal{N}_2$, then we can fix $\varepsilon_1 = \alpha_1 + \sum_{r \in \mathcal{N}_1} \beta_r x_r$ and $\varepsilon_2 = \alpha_2 + \sum_{r \in \mathcal{N}_2} \beta_r x_r$ so that (2.7) reduces to

$$\frac{P(Y)}{P(X)} = \frac{e^{(x_2 \varepsilon_1 + x_1 \varepsilon_2)}}{e^{(x_1 \varepsilon_1 + x_2 \varepsilon_2)}} = e^{(x_2 - x_1)(\varepsilon_1 - \varepsilon_2)}. \tag{2.8}$$

Suppose that each graylevel $x_s \in \mathcal{S}$ is replaced with color $n - 1 - x_s$. Then the expression in (2.8) is not affected. This was called the *reversibility* property in [26].

2.3.2 Single-flip algorithms

We have used two single-flip methods, the Metropolis single-flip and the Gibbs Sampler [27]. The Metropolis single-flip uses the same rule as the Metropolis exchange but compares the energy of the current configuration with the energy due to replacing the site with a randomly selected element of Λ. Thus, a maximum of one site is modified at each attempted exchange and the histogram is unconstrained. The Gibbs Sampler [27] uses a different update rule. It changes a site to color $g \in \Lambda$ with probability $P(x_s = g \mid \mathcal{N}_s)$. Theoretically, all these algorithms should converge to the same ground state; they should vary only in rate of convergence and runtime.

2.3.3 Iterating and temperature annealing

Both exchange and single-flip algorithms are iterated to synthesize a texture sample. If the image size is $M \times N$ then one iteration is counted as MN attempted exchanges or flips. In studies of texture modeling, the expression (2.2) was posed without the temperature term and temperature effects were completely ignored. This is equivalent to iterating at a constant temperature, $T = 1$.

In many applications of MRF's, especially where they are used as a prior image model in a Bayesian optimization framework, the temperature parameter is lowered gradually during the iterations. This is called "annealing" after the physical process with the same name. The typical annealing schedule is

$$T = \frac{c}{\log(1 + \lfloor i/i_{eq} \rfloor)}, \tag{2.9}$$

where $i = 0, 1, \ldots$ is the iteration number, i_{eq} is the number of iterations it takes for the distribution to reach equilibrium at the current temperature, i.e., to approximate a sample of the Gibbs distribution at that temperature, and $\lfloor\ \rfloor$ indicates truncation. The scale factor in the numerator is typically chosen in the range $c \in (0, 10]$. Though its choice is ad hoc, its behavior is understood as a rate constant that is proportional to how slow the annealing progresses.

In some papers, e.g., [23], iterating at constant temperature is called annealing; in this thesis, annealing will only refer to iterating while lowering the temperature.

2.3.4 Stochastic relaxation vs. deterministic relaxation

If ΔE is negative in the Metropolis exchange then the swap always occurs. However, if ΔE is positive, i.e., the energy increases, the exchange is only accepted with probability $\exp(-\Delta E/T)$. It is the presence of this second condition that basically distinguishes a *stochastic relaxation* algorithm like the Metropolis exchange from the computer vision *relaxation* algorithms such as [54].

Note that only the second condition is affected by temperature. When $T = \infty$, the exchange always occurs – all configurations are equally likely and Z equals the

number of configurations. When $T = 0$, only changes which decrease energy are made. The latter case is equivalent to the deterministic relaxation and gradient-descent style algorithms.

2.4 Analysis of Markov/Gibbs texture

For texture modeling it is important to be able to estimate the parameters of the model. For the energy functions given in (2.3) and (2.4) the β's are the parameters to be estimated. For estimation we implemented the following maximum likelihood (ML) method which was used by [17, 26], and which is based on the idea of Besag Codings [5].

A Besag coding partitions the lattice into colors $\mathcal{S} = \bigcup_i \mathcal{C}_i$, $\mathcal{C}_i \bigcap \mathcal{C}_j = \emptyset$ unless $i = j$, so that all sites of color $\mathcal{C}_i$ have conditional probabilities that are independent of each other. For example, when $p = 1$ the Besag coding partitions the lattice into a checkerboard of two colors; hence, all sites on the white squares will only be conditioned on the black squares, and vice-versa. For $p = 2$ there are four colors in the Besag coding, and for $p = 3, 4$ there are nine colors.

2.4.1 Maximum likelihood with Besag codings

For a given color in the Besag coding, $\mathcal{C}_j \subset \mathcal{S}$, we estimate the parameters by maximizing the log likelihood,

$$\mathcal{L}(\mathbf{x}) = \sum_{s \in \mathcal{C}_j} \ln P(x_s = g \mid \mathcal{N}_s). \tag{2.10}$$

Newton's method [60] is applied to estimate the vector $\mathbf{b}$ of parameters, β_k, $k = 1, ..., K$,

$$\mathbf{b}^{i+1} = \mathbf{b}^i - \mathbf{J}^{-1}\mathbf{g}^i,$$

where i is the iteration,

$$\mathbf{J}(k) = \frac{\partial^2 \mathcal{L}}{\partial \mathbf{b}(k) \partial \mathbf{b}(k')},$$

and

$$\mathrm{g}(k) = \frac{\partial \mathcal{L}}{\partial \mathrm{b}(k)}.$$

For the auto-binomial model the conditional probabilities are

$$p(x_s = g \mid x_r, r \neq s) = \binom{n-1}{g} \theta_s^g (1-\theta_s)^{n-1-g},$$

where

$$\theta_s = \frac{e^{\varepsilon_s}}{1+e^{\varepsilon_s}} \quad \text{and} \quad \varepsilon_s = \frac{1}{T}(\alpha_s + \sum_{k=1}^{K} \beta_k \sum_{r \in \mathcal{N}_s^k} x_r).$$

the estimation method calculates

$$\mathbf{J}(k) = \sum_{s \in \mathcal{C}_j} \frac{[\sum_{r \in \mathcal{N}_s^k} x_r][\sum_{r \in \mathcal{N}_s^{k'}} x_r](1-n)e^{\varepsilon_s}}{T^2(1+e^{\varepsilon_s})^2},$$

and

$$\mathbf{g}(k) = \sum_{s \in \mathcal{C}_j} \frac{[\sum_{r \in \mathcal{N}_s^k} x_r][g + e^{\varepsilon_s}(g-n+1)]}{T(1+e^{\varepsilon_s})}.$$

the estimates of **b** from each coding are typically averaged to give the final estimate.

This ML method was used in [16, 17, 26] without annealing, i.e., $T = 1$. It worked reasonably well over some ranges of parameters, but has some problems due to the estimation over one coloring which only uses part of the data (which means even more data is needed to obtain a good estimate) and the fact that the estimate may not exist. A good review and discussion of other analysis methods can be found in [70].

We do not elaborate on the problem of estimating the bonding parameters because it will be shown soon that the bonding parameters do not uniquely characterize the desired texture patterns. This point will be clarified in Section 4.2.1 and in Chapter 6.

2.5 Bayesian formulation with Markov/Gibbs prior

Bayesian and essentially equivalent minimum description length (MDL) methods have emerged as a popular and flexible framework for posing a variety of computer vision and image processing problems. We consider a typical scenario, and show how

it relates to temperature and texture.

The image restoration of [27] is based on the following MAP (maximum a posteriori) estimation. Let the observation (degraded image) be represented by G and the original image be represented by X. Now maximize the conditional probability distribution of the undegraded image given the observed image by finding the mode of the *posterior* distribution,

$$P(X = \mathbf{x} \mid G = \mathbf{g}) = \frac{P(G = \mathbf{g} \mid X = \mathbf{x})P(X = \mathbf{x})}{P(G = \mathbf{g})}. \tag{2.11}$$

Differentiating the log of the posterior with respect to X eliminates the denominator so we need only consider the two numerator terms.

The *prior* model for the image, $P(X = \mathbf{x})$, is assumed to be a Gibbs distribution having some exponent U_X. The degradation is assumed to be an invertible function of X combined with white Gaussian noise that is independent of X. Based on this model the conditional probability for $P(G \mid X)$ is Gaussian with some exponent U_G. The posterior then has exponent $U_X + U_G$ which yields a valid Gibbs distribution under suitable assumptions on the neighborhood structure.

Bayesian optimization using the Gibbs model is thus a problem of maximizing the sum $U_X + U_G$ subject to a set of constraints. This is equivalent to minimizing the Gibbs energy under the constraints. When the prior image is textured, the energy function contained in U_X may take the form of (2.1). Whatever the form of the posterior energy function, it contains U_X in this additive fashion.

The solution to the energy minimization is typically implemented using an annealing schedule as in (2.9). When annealing is used for Bayesian optimization the temperature divides the prior, scaling its energy in a time varying way. While it is known that annealing sharpens the peaks of the objective function, the effect of temperature on the texture is not well understood. Although one may be able to use different temperatures for the prior and for the overall system, it is important to understand these temperature induced effects on the prior.

Chapter 3

Aura framework, linear energy, and physical texture behavior

3.1 Introduction

The Markov/Gibbs (MRF) models have been studied for texture modeling but much is still unknown about what kinds of texture patterns they will produce. We will make progress toward solving this problem by using a new framework for reformulating the MRF. From this, we relate the MRF to morphological dilation, co-occurrence statistics, and a new physical description of its texture behavior. The new formulation is linear; this property will be exploited in subsequent chapters to analyze temperature effects and ground states.

The new framework is based on the neighborhood dependent idea of an aura. The aura has its foundation in the idea of a neighborhood structure; its intuitive meaning can be described as "the presence of set B in the *neighborhood* of set A". The aura can be formulated using simple set theory or using dilations from mathematical morphology; we show how to define it from both. The useful new tools of aura measure and aura matrix are defined in Section 3.2. In Section 3.3 the popular texture analysis tool of the co-occurrence matrix is related to the new aura matrix.

The new aura framework is used in Section 3.4 to reformulate the nonlinear Gibbs energy as a linear combination of aura measures. Applying this reformulation, I show

how the visual behavior of the MRF textures can be described in terms of physical notions such as separation/mixing and minimum/maximum boundary length. These behaviors are also illustrated in Section 3.5. The relations developed in this chapter are the first we know of which bring together co-occurrences, morphology, and MRF's into one notational framework. The miscibility and boundary length behavior also appears to be the first generalization of the boundary length behavior of the Ising model.

3.2 Definitions

3.2.1 Notation

Recall that each site s of the lattice $\mathcal{S}$ has assigned to it an integer $x_s \in \Lambda = \{0, 1, \ldots, n-1\}$ which represents the graylevel value of a pixel at site s. The graylevel sets of the lattice are defined as follows:

$$\mathcal{S}_g = \{s \in \mathcal{S} | x_s = g\}, \ \forall g \in \Lambda. \tag{3.1}$$

Note that the graylevel sets $\mathcal{S}_g, g \in \Lambda$, constitute a partition of $\mathcal{S}$, i.e., $\bigcup_{g\in\Lambda} \mathcal{S}_g = \mathcal{S}$ and $\mathcal{S}_g \bigcap \mathcal{S}_{g'} = \emptyset$, $\forall g, g' \in \Lambda$, $g \neq g'$. When the uniform histogram assumption is made, then

$$|\mathcal{S}_g| = \frac{|\mathcal{S}|}{n} = \gamma, \ \ \forall g \in \Lambda.$$

3.2.2 Aura sets and morphology

The following simple definition is the basic concept that underlies the new framework.

Definition 3.1 *Let $\mathcal{S}_g, \mathcal{S}_{g'}$ be two subsets $\subseteq \mathcal{S}$. Then the aura of $\mathcal{S}_g$ with respect to $\mathcal{S}_{g'}$ for the neighborhood structure $\{\mathcal{N}_s, s \in \mathcal{S}\}$ is a subset of $\mathcal{S}$ defined by*

$$\bigcup_{s\in\mathcal{S}_g} (\mathcal{N}_s \cap \mathcal{S}_{g'}).$$

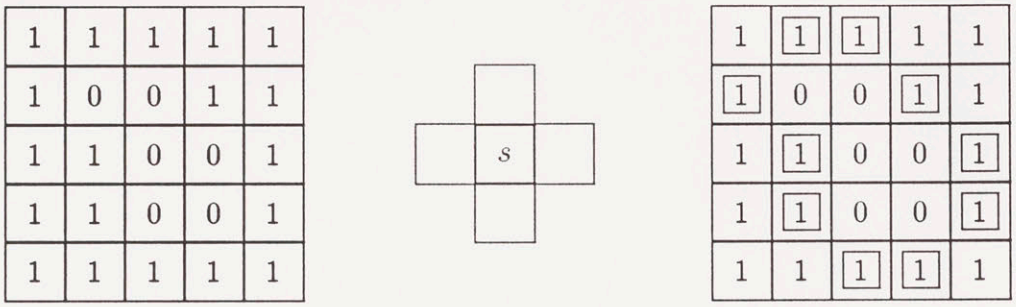

(a) (b) (c)

Figure 3-1: Example of an aura on a binary lattice with the four nearest-neighbors. (a) Sample binary lattice. (b) Structuring element $\mathcal{N}_s$ consists of the four nearest-neighbors of site s. (c) The set of double-boxed sites is the aura of the set of all 0's with respect to the set of all 1's. Notice the "aura-like" shape from which the set takes its name.

The aura of a set $\mathcal{S}_g$ with respect to a set $\mathcal{S}_{g'}$ will be denoted by

$$\mathcal{O}_{\mathcal{S}_{g'}}(\mathcal{S}_g, \mathrm{N}). \tag{3.2}$$

The aura of a set with respect to itself will be called the self-aura.

The original definition and naming of the aura set is due to Elfadel. In [21], the aura is defined for any two sets and several of its properties are stated.

It is very important to understand that the aura depends on the neighborhood structure chosen for the lattice. In this thesis the structure **N** is given by the order of the model and the periodic lattice assumptions; thus, we choose to omit the notational dependency on **N** from (3.2) and use for the aura the simplified notation $\mathcal{O}_{\mathcal{S}_{g'}}(\mathcal{S}_g)$.

Example 3.2 *An example of an aura is shown in Figure 3-1. In (a) is shown a binary 5×5 lattice, $\mathcal{S}$. Let $\mathcal{S}_0 = \{x_s \mid x_s \in \mathcal{S}, x_s = 0\}$ and $\mathcal{S}_1 = \{x_s \mid x_s \in \mathcal{S}, x_s = 1\}$. Let $\mathcal{N} = \{x_r \mid r \in \mathcal{N}_s\}$ as shown in (b). Then $\mathcal{O}_{\mathcal{S}_1}(\mathcal{S}_0)$ are the elements marked by the double-boxes in (c).*

Morphological construction of aura

Mathematical morphology has been applied to a rapidly expanding variety of image processing tasks including nonlinear filtering, pattern analysis, and fractal dimension estimation [41]. In this section we show how the aura can be constructed using the basic morphological operation of dilation.

Following the notation of [41], we have the following definition from mathematical morphology, where $A, B \subseteq \mathcal{S}$ and $A \cap B = \emptyset$:

Definition 3.3 *Let A and B be two sets. Then the dilation, denoted by $\oplus$, of A by B is*

$$A \oplus B = \{a + b \mid a \in A,\ b \in B\} = \bigcup_{b \in B} A_b \,.$$

We say A_b is the *translate* of the set A by the vector b. Note that $A \oplus B = B \oplus A$. If $\hat{B}$ represents the set B after planar rotation by 180°, then $A \oplus B = \{z \mid (\hat{B} + z) \cap A \neq \emptyset\}$, i.e., the set of points where translated $\hat{B}$'s intersect A.

Proposition 3.4 *Let $\mathcal{N}$ be the structuring element of which the neighborhoods $\mathcal{N}_s$ are the translates. Then the aura of A with respect to B on a lattice with neighborhood structure* **N** *is equivalent to the dilation of A followed by intersection with B,*

$$\mathcal{O}_B(A) = (\mathcal{N} \oplus A) \cap B.$$

Proof:

$$\begin{aligned} \mathcal{O}_B(A) &= \bigcup_{a \in A} (\mathcal{N}_a \cap B) \\ &= (\bigcup_{a \in A} \mathcal{N}_a) \cap B \\ &= (\mathcal{N} \oplus A) \cap B. \end{aligned}$$

■

Those familiar with mathematical morphology may wish to note that we construct a graylevel aura set using binary dilation.

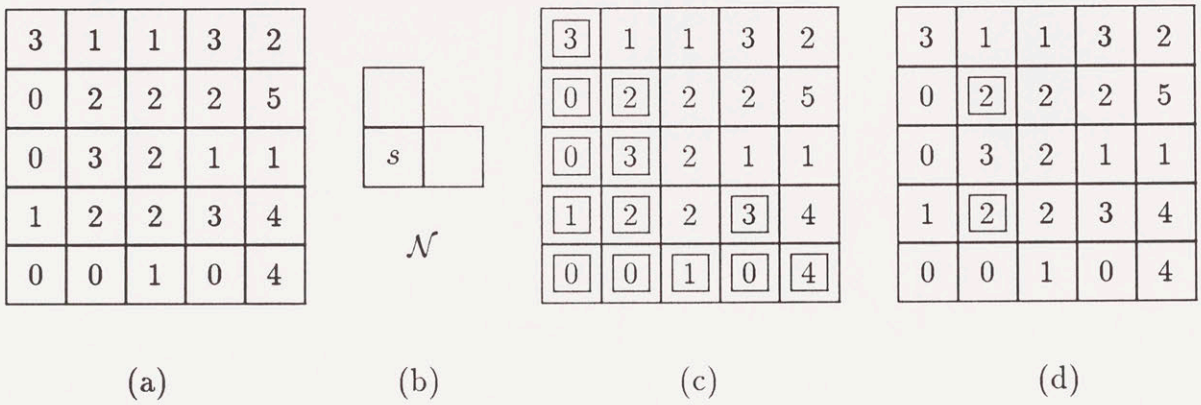

Figure 3-2: Example of forming an aura using morphological dilation. (a) Graylevel lattice. (b) Structuring element $\mathcal{N}$ consists of two neighbors of site s. (c) The double-boxed sites are the dilation of the set of all 0's with $\mathcal{N}$. (d) The double-boxed sites are the aura of the 0's with respect to the 2's.

Example 3.5 *In Figure 3-2 we show an example of forming an aura using dilation. In (a) is shown a* 5×5 *lattice,* $\mathcal{S}$*, in which the sites are assigned values in* $\{0, 1, 2, 3\}$*. Let* $A = \mathcal{S}_0$*,* $B = \mathcal{S}_2$*, and* $\mathcal{N}$ *be the structuring element as shown in (b). The dilation,* $A \oplus \mathcal{N}$*, is given in (c). Intersecting this set with* B *gives the aura with respect to* B*,* $\mathcal{O}_B(A)$*, shown in (d).*

The morphological approach to image processing is based on geometric primitives called structuring elements and on various set operations such as dilation and erosion which use these primitives. In the conclusions of [17], one of the disadvantages of the MRF model was stated, "the textural primitives of the Markov random field are nongeometric." What we will see in the next sections is that a *measure* over the aura set, formed from a geometric primitive, appears directly in the MRF energy function.

3.2.3 Aura measures

The easiest way for measuring the size of the aura of a set A with respect to a set B is by counting the number of elements, $|\mathcal{O}_B(A)|$. Note that we have from the

definition and from the known properties of sets,

$$|\mathcal{O}_B(A)| \leq \sum_{s \in A} |\mathcal{N}_s \cap B|. \tag{3.3}$$

The right side appears more frequently in problems involving image synthesis or processing. In particular, we will show that the right side relates to image co-occurrence statistics. The following definition of the measure of an aura, due to Elfadel [21], is adopted:

Definition 3.6 *The aura measure of two sets $\mathcal{S}_g, \mathcal{S}_{g'}$ is denoted by $m(\mathcal{S}_g, \mathcal{S}_{g'})$ and defined by*

$$m(\mathcal{S}_g, \mathcal{S}_{g'}) = \sum_{s \in \mathcal{S}_g} |\mathcal{N}_s \cap \mathcal{S}_{g'}|.$$

Since a graylevel set $\mathcal{S}_g$ is completely defined by g we will typically shorten $m(\mathcal{S}_g, \mathcal{S}_{g'})$ to $m(g, g')$.

Example 3.7 *For the sets in Example 3.2, $m(0,1) = 12$, and $|\mathcal{O}_{\mathcal{S}_1}(\mathcal{S}_0)| = 10$.*

Note that in general $m(g, g') \neq m(g', g)$. However, for MRF's the neighborhood structure is always symmetric and we have the following result.

Proposition 3.8 *If $\{\mathcal{N}_s, s \in \mathcal{S}\}$ is a symmetric neighborhood structure, then*

$$m(g, g') = m(g', g), \qquad \forall \mathcal{S}_g, \mathcal{S}_{g'} \subseteq \mathcal{S}.$$

The proof of this along with several properties of the aura measure are given in [22].

3.2.4 Aura matrices

We now introduce a useful tool for image processing, the *aura matrix*. The aura matrix is a collection of the aura measures for all the sets of interest on the lattice. Here we define it for graylevel sets which partition the image.

Definition 3.9 *Let $S_i \subseteq \mathcal{S}$, $\bigcup_{i\in\Lambda} S_i = \mathcal{S}$, and $S_i \cap S_j = \emptyset$ unless $i = j$, $\forall i, j \in \Lambda$. Then the aura matrix, $\mathbf{A}$, is the $n \times n$ integer matrix defined by*

$$\mathbf{A} = \begin{bmatrix} m(0,0) & \dots & m(0,n-1) \\ \vdots & & \vdots \\ m(n-1,0) & \dots & m(n-1,n-1) \end{bmatrix}.$$

Proposition 3.10 *(Aura Matrix Properties) Let $\mathbf{A}$ be an aura matrix. Then,*

(a) Each row sum satisfies:

$$\sum_{j=0}^{n-1} a_{ij} = |S_i||\mathcal{N}|,\ i = 0, \dots, n-1;$$

(b) Each column sum satisfies:

$$\sum_{i=0}^{n-1} a_{ij} = |S_j||\mathcal{N}|,\ j = 0, \dots, n-1;$$

(c) If $\mathcal{N}$ is symmetric, then $\mathbf{A}$ is symmetric, and

$$\sum_{j=0}^{n-1} a_{kj} = \sum_{i=0}^{n-1} a_{ik} = |S_k||\mathcal{N}|,\ \ k = 0, \dots, n-1;$$

Proof: For (a) we have

$$\begin{aligned} \sum_{j=0}^{n-1} a_{ij} &= \sum_{j=0}^{n-1} m(S_i, S_j) \\ &= m(S_i, \cup_{j=0}^{n-1} S_j) \\ &= m(S_i, \mathcal{S}) \\ &= |S_i||\mathcal{N}|, \end{aligned}$$

and similarly for (b). The proof of (c) comes directly from Proposition 3.8 together with (a) and (b). ∎

Note that if we did not assume periodic boundary conditions, then the right-hand sides would become upper bounds on the left hand sides in (a)-(c).

Aura matrix irreducibility

Because the lattice is connected one can move to any graylevel in the image from any other graylevel. Equivalently, from any row i of the aura matrix, there is a path of non-zero elements, a_{ik}, a_{kj}, a_{jl}, etc., which eventually reaches all the rows. This "reachability" property is equivalent to the constraint that the aura matrix be irreducible. An example of an irreducible matrix is one that has $a_{ij} \neq 0$ for $|i-j| = 1$; an example of a reducible matrix is one that is block diagonal. This property will be used in Chapter 6 when aura matrix structure is derived. It is also important when this work is generalized to a graph theory framework.

3.3 Co-occurrence and aura matrices

The significance of pairwise graylevel information for visual texture discrimination was advocated in 1962 by Julesz [35]. Since then, co-occurrence matrices and their features have become very popular for a variety of texture analysis problems [29, 14, 67, 66, 4]. We now define the co-occurrence matrix and show how it is related to the aura matrix.

Definition 3.11 *Let d be a lattice vector and let $C_{gg'}(d)$ be the set of site pairs defined by*

$$C_{gg'}(d) = \{(s,r) \in \mathcal{S} \times \mathcal{S}, \mid s - r = d, \; x_s = g, \; x_r = g' \; \}.$$

Let $c_d(g,g')$ denote the number of elements in the set $C_{gg'}(d)$. Then the co-occurrence matrix is defined by $\mathbf{C}(d) = [c_d(g,g')]$.

The literature is not consistent in its definition of co-occurrence matrices. In some places $C_{gg'}(d)$ is normalized by the sum of its elements; in other places the above "pairwise" Definition 3.11 is replaced with a "symmetric co-occurrence" definition which also may or may not be normalized. The symmetric co-occurrence combines two of the pairwise co-occurrences at a given distance and angle θ, $\theta + 180°$, giving $\mathbf{C}^\theta = \mathbf{C}(d) + \mathbf{C}(-d)$.

An alternate way of writing Definition 3.11 comes from noticing that

$$c_d(g, g') = \sum_{s \in \mathcal{S}_g} |(s + d) \cap \mathcal{S}_{g'}|. \tag{3.4}$$

Thus, if a neighborhood consists of a single site, $\mathcal{N}_s = (s + d)$, then

$$\begin{aligned} c_d(g, g') &= \sum_{s \in \mathcal{S}_g} |\mathcal{N}_s \cap \mathcal{S}_{g'}| \\ &= m(g, g'). \end{aligned}$$

The aura matrix which is equivalent to $\mathbf{C}^\theta$ can be constructed by letting $\mathcal{N}_s$ be the sites $\{s + d, s - d\}$, giving

$$c_\theta(g, g') = c_d(g, g') + c_{-d}(g, g') = \sum_{s \in \mathcal{S}_g} |\mathcal{N}_s \cap \mathcal{S}_{g'}| = m(g, g'), \tag{3.5}$$

so that $\mathbf{A} = \mathbf{C}^\theta$. Indeed, by choosing $\mathcal{N}_s$ to be some desired geometric primitive, one can obtain "co-occurrences" over any neighborhood structure.

Letting the desired geometric primitive be the MRF subneighborhoods defined in (2.6) we have

$$m(g, g') = \sum_{k=1}^{K} m^k(g, g'), \tag{3.6}$$

where $m^k(g, g')$ is the aura measure over a two element symmetric neighborhood, $\mathcal{N}_s^k = \{s + d_k,\ s - d_k\}$. Forming an aura matrix over the subneighborhood k defines $\mathbf{A}^k = [m^k(i, j)]$ for $i, j \in \Lambda$. In this case, $\mathbf{A}^k$ is just a symmetric co-occurrence matrix. From (3.6),

$$\mathbf{A} = \sum_{k=1}^{K} \mathbf{A}^k. \tag{3.7}$$

In summary, the MRF aura matrices are equivalent to a sum of symmetric co-occurrence matrices taken over the subneighborhoods, $\mathcal{N}^k$. Equivalently, the MRF aura matrices are a sum of pairwise co-occurrence matrices taken over each element in the neighborhood,

$$\mathbf{A} = \sum_{s+d \in \mathcal{N}_s} \mathbf{C}(d).$$

The aura matrix generalizes the pairwise and symmetric co-occurrence matrices by allowing the counts to occur over any geometric primitive. We adopt the new name "aura matrix" instead of "linear combination of co-occurrence matrices over geometric neighborhood" because it is shorter and because it makes explicit the geometric dependence of the statistic.

The utility of the aura matrix is further supported by the claims of [18, 55] where excellent results were obtained from features that combined co-occurrences from different displacements. Another example in support of the aura matrix is [28] where texture features are made from a combination of symmetric co-occurrences averaged over the four directions, $\theta = 0°, 45°, 90°, 135°$ to "remove directional biases." Their resulting matrix of statistics is an aura matrix for a second order MRF.

Co-occurrences and Markov/Gibbs random fields

For Markov fields the aura/co-occurrence relationship aids in the choice of which co-occurrence displacements are important, a problem examined by Zucker and Terzopolous [73] for general textures. In Section 3.4 the MRF energy will be written as a function of the aura matrix. Thus, the co-occurrences which lie in the Markov neighborhood completely characterize the pattern.

Relating the expected values of the aura measures to the MRF bonding parameters is still a difficult problem. For the Ising model where Z is known this has been done by Cross [16] for positive parameters in the range $\beta = 0 \ldots 1$. When temperature effects are characterized in Chapter 4, we confirm his isotropic results and extend them empirically.

Co-occurrence matrix, correlation, and entropy

The aura measures and co-occurrences have a special relation to the autocorrelation even though they are different. Observe that aura matrices need not be positive semidefinite like correlation matrices. In tests by Conners and Harlow [14] comparing discrimination abilities of texture analysis tools, the co-occurrences performed much better than the power spectrum, which is the Fourier transform of the correla-

tions. Conners and Harlow concluded that the co-occurrences contain more "textural information" than the correlations.

The precise relationship between co-occurrences and correlation can be made as follows. To compute the autocorrelation at a given lag d, one forms the sum of products,

$$\sum_{s \in \mathcal{S}} x_s x_{s+d}.$$

This can be equivalently written as

$$\sum_{g \in \Lambda} \sum_{s \in \mathcal{S}_g} g x_{s+d}$$

or

$$\sum_{g \in \Lambda} \sum_{s \in \mathcal{S}_g} g \sum_{g' \in \Lambda} g' \sum_{(s+d) \in \mathcal{S}_{g'}} 1.$$

Regrouping and evaluating the right-most sum gives

$$\sum_{g,g' \in \Lambda} g g' \sum_{s \in \mathcal{S}_g} |(s+d) \cap \mathcal{S}_{g'}|,$$

which by the alternate form of the co-occurrence definition (3.4) reduces to

$$\sum_{g,g' \in \Lambda} g g' c_d(g, g'). \tag{3.8}$$

Thus the correlation at a particular lag, d, is the weighted sum of co-occurrences at the displacement d.

Based on (3.8), a "correlation feature" of the co-occurrence matrices can be defined. This feature has been used extensively in texture analysis in the literature. In the literature it is defined on the normalized pairwise co-occurrence matrix, but we define it here on the normalized aura matrix.

Definition 3.12 *Let*

$$\mathbf{m}(i,j) = \frac{m(i,j)}{\sum_{i=0}^{n-1} \sum_{j=0}^{n-1} m(i,j)},$$

then the correlation feature of the aura matrix is

$$\frac{\sum_{i=0}^{n-1}\sum_{j=0}^{n-1}(i-\mu_i)(j-\mu_j)\mathbf{m}(i,j)}{\sigma_i\sigma_j},$$

where

$$\mu_i = \sum_{i=0}^{n-1} i \sum_{j=0}^{n-1} \mathbf{m}(i,j),$$

$$\mu_j = \sum_{j=0}^{n-1} j \sum_{i=0}^{n-1} \mathbf{m}(i,j),$$

$$\sigma_i^2 = \sum_{i=0}^{n-1}(i-\mu_i)^2 \sum_{j=0}^{n-1} \mathbf{m}(i,j),$$

and

$$\sigma_j^2 = \sum_{j=0}^{n-1}(j-\mu_j)^2 \sum_{i=0}^{n-1} \mathbf{m}(i,j).$$

This weighted sum of aura measures will show up in a special way in Section 3.4.

In the texture analysis literature the correlation feature is often used in conjunction with an entropy feature of the co-occurrence matrix. Here we define the same entropy feature on the normalized aura matrix.

Definition 3.13 *Let*

$$\mathbf{m}(i,j) = \frac{m(i,j)}{\sum_{i=0}^{n-1}\sum_{j=0}^{n-1} m(i,j)},$$

then the entropy feature of the aura matrix is

$$-\sum_{i=0}^{n-1}\sum_{j=0}^{n-1} \mathbf{m}(i,j)\log \mathbf{m}(i,j).$$

This is a "second order entropy" and will be useful for measuring change in a texture pattern as it is synthesized. In contrast the "first order entropy" will be constant during texture synthesis as the histogram is preserved. The first order entropy is maximized by the uniform histogram assumption where each graylevel occurs with probability $1/n$.

In comparing entropies for different graylevels we will employ the *normalized entropy*, which is the above feature normalized by the maximum aura matrix entropy, $n \log n$.

In [18] co-occurrences were generalized to provide statistics of features instead of just graylevels. The same could be done with the aura matrix, providing geometric "mixing" measures for any feature.

3.4 Linear reformulation of energy

3.4.1 General anisotropic Gibbs case

In this section we show how a homogeneous nonlinear Gibbs energy can be formulated as a linear combination of aura measures. The reformulation shown here is a straightforward generalization of the one originally conceived by Elfadel and given for the auto-binomial MRF in [21].

Proposition 3.14 *Let $\{\mathcal{S}_g, g \in \Lambda\}$ be a partition of $\mathcal{S}$ where $x_s = g$ if $s \in \mathcal{S}_g$. Let the symmetric neighborhood $\mathcal{N}$ be partitioned into K isotropic subneighborhoods. Then any anisotropic nonlinear function of the form,*

$$\sum_{s\in\mathcal{S}} \sum_{r\in\mathcal{N}_s} V_r(x_s, x_r), \tag{3.9}$$

can be rewritten as a linear function of aura measures,

$$\sum_{k=1}^{K} \sum_{g,g'\in\Lambda} V^k(g,g')m^k(g,g'). \tag{3.10}$$

Proof: Using the assumption that $\mathcal{S}_g$ partitions $\mathcal{S}$, we can rewrite (3.9) as

$$\sum_{g\in\Lambda} \sum_{s\in\mathcal{S}_g} \sum_{r\in\mathcal{N}_s} V_r(g, x_r).$$

Let $V^k(g, x_r)$ be the value of $V_r(g, x_r)$ in subneighborhood k where the interaction $V_r(x_s, x_r)$ is assumed to be isotropic. Then we obtain

$$\sum_{g\in\Lambda} \sum_{s\in\mathcal{S}_g} \sum_{k=1}^{K} \sum_{r\in\mathcal{N}_s^k} V^k(g, x_r).$$

Now we partition $\mathcal{N}_s^k$ into its different graylevels. When $r \in S_{g'}$, we have $x_r = g'$, giving,

$$\sum_{g\in\Lambda}\sum_{s\in\mathcal{S}_g}\sum_{k=1}^{K}\sum_{g'\in\Lambda}\sum_{r\in\mathcal{N}_s^k\cap\mathcal{S}_{g'}} V^k(g,g'),$$

which after rearranging, becomes

$$\sum_{k=1}^{K}\sum_{g,g'\in\Lambda}\sum_{s\in\mathcal{S}_g}\sum_{r\in\mathcal{N}_s^k\cap\mathcal{S}_{g'}} V^k(g,g').$$

This is equivalent to

$$\sum_{k=1}^{K}\sum_{g,g'\in\Lambda} V^k(g,g')\sum_{s\in\mathcal{S}_g}|\mathcal{N}_s^k\cap\mathcal{S}_{g'}|,$$

which gives, finally,

$$\sum_{k=1}^{K}\sum_{g,g'\in\Lambda} V^k(g,g')m^k(g,g').$$

■

3.4.2 Special cases

Proposition 3.14 works for any homogeneous function $V_r(x_s, x_r)$, e.g., the isotropic or anisotropic auto-binomial and Potts models given below.

Auto-binomial

The anisotropic auto-binomial function to be maximized is

$$\sum_{k=1}^{K}\beta_k\sum_{g,g'\in\Lambda} gg'm^k(g,g'). \tag{3.11}$$

Letting $\mathbf{g} = [0,1,\ldots,n-1]^T$, this is more compactly written in terms of aura matrices over subneighborhoods as

$$\sum_{k=1}^{K}\beta_k\mathbf{g}^T\mathbf{A}^k\mathbf{g}. \tag{3.12}$$

Therefore, the anisotropic energy will be a linear sum of isotropic energy terms with weights equal to the bonding parameters.

For the auto-binomial case an interesting new observation can be made by combining (3.11) with (3.5) and (3.8). This combination yields an alternate form of (3.11),

$$\sum_{k=1}^{K} \beta_k \sum_{g,g' \in \Lambda} gg'(c_{d_k}(g,g') + c_{d_{-k}}(g,g')).$$

In effect, we have that the nonlinear energy is equivalent to a linear combination of aura measures, which is equivalent to a linear combination of symmetric co-occurrences over the isotropic neighborhoods, which is also equal to a linear combination of the autocorrelation function over the lags which lie in the MRF neighborhood. Thus, the bonding parameters have another new interpretation as weights for combining correlation lags.

Potts

Similarly, the anisotropic Potts model gives the function to be maximized,

$$\sum_{k=1}^{K} \beta_k \sum_{g,g' \in \Lambda} (2\delta_{gg'} - 1) m^k(g,g').$$

Bunks

Even the model used by Bunks [7] for representing striated geological sediments can be put into this linear framework. This model required the periodic structure of a sinusoid and used the energy function

$$-\frac{1}{2} \sum_{s \in \mathcal{S}} x_s \sum_{r \in \mathcal{N}_s} x_r \cos(\lambda \pi |d \cdot (s-r)|),$$

where d is the unit dip vector, λ is the bed frequency, $x_s, x_r \in \{-1, 1\}$, and $\mathcal{N}_s$ is a square of fixed size which is large enough to contain some sites that are more than $1/\lambda$ apart. This is an auto-model, but at first glance, the function $V_{sr}(x_s, x_r) = \cos(\lambda \pi |d \cdot (s-r)|)$ appears dependent on s. However, since V_{sr} is only evaluated for $x_r \in \mathcal{N}_s$, then the distance $(s-r)$ will only take on a small number of values which depend on the shape of $\mathcal{N}_s$. Since the neighborhood is a translate of a fixed $\mathcal{N}$

and d, λ are constants, then V_{sr} can be predetermined for each symmetric neighbor, $x_r \in \mathcal{N}_s^k$ and treated as an anisotropic parameter similar to the β_k's.

3.5 Physical texture behavior

Now we apply the aura measures to explain the behavior of synthesized MRF texture patterns. This will give us intuition which will help characterize what the patterns will look like near their minimum-energy states. The simulations here assume a rectangular $M \times N$ lattice with periodic boundary conditions and the auto-binomial MRF energy function described in Section 2.2.1, though similar analysis applies to any combination of aura measures.

The textures illustrated in this section have been synthesized by the Metropolis exchange method with log annealing according to the schedule

$$T = \frac{c}{\log(\lfloor i/i_{eq} \rfloor + 1)},$$

where $i = 0, 1, \ldots, 10000$ is the iteration number, the rate constant $c = 2.7$, and $i_{eq} = 10$ iterations. The initial state for all these simulations was a random noise image with uniform histogram. Because of the exchange operation the histogram is preserved throughout the texture synthesis and the (assumed constant) external field can be ignored.

3.5.1 Miscibility: separation and mixing

The aura measures have a physical interpretation as "miscibilities." When $m(g, g')$ is large, graylevel sets g and g' "mix"; when $m(g, g')$ is small, the sets "separate." This miscibility behavior also describes the behavior of the MRF texture patterns.

For positive isotropic parameters the behavior is described by the separation of the different colors, or graylevels. In Figure 3-3 are shown four texture samples which are typical of first-order positive isotropic MRF's. All of these have identical parameters $\beta = 1$; the only difference is that the number of graylevels in (a)-(d) changes from

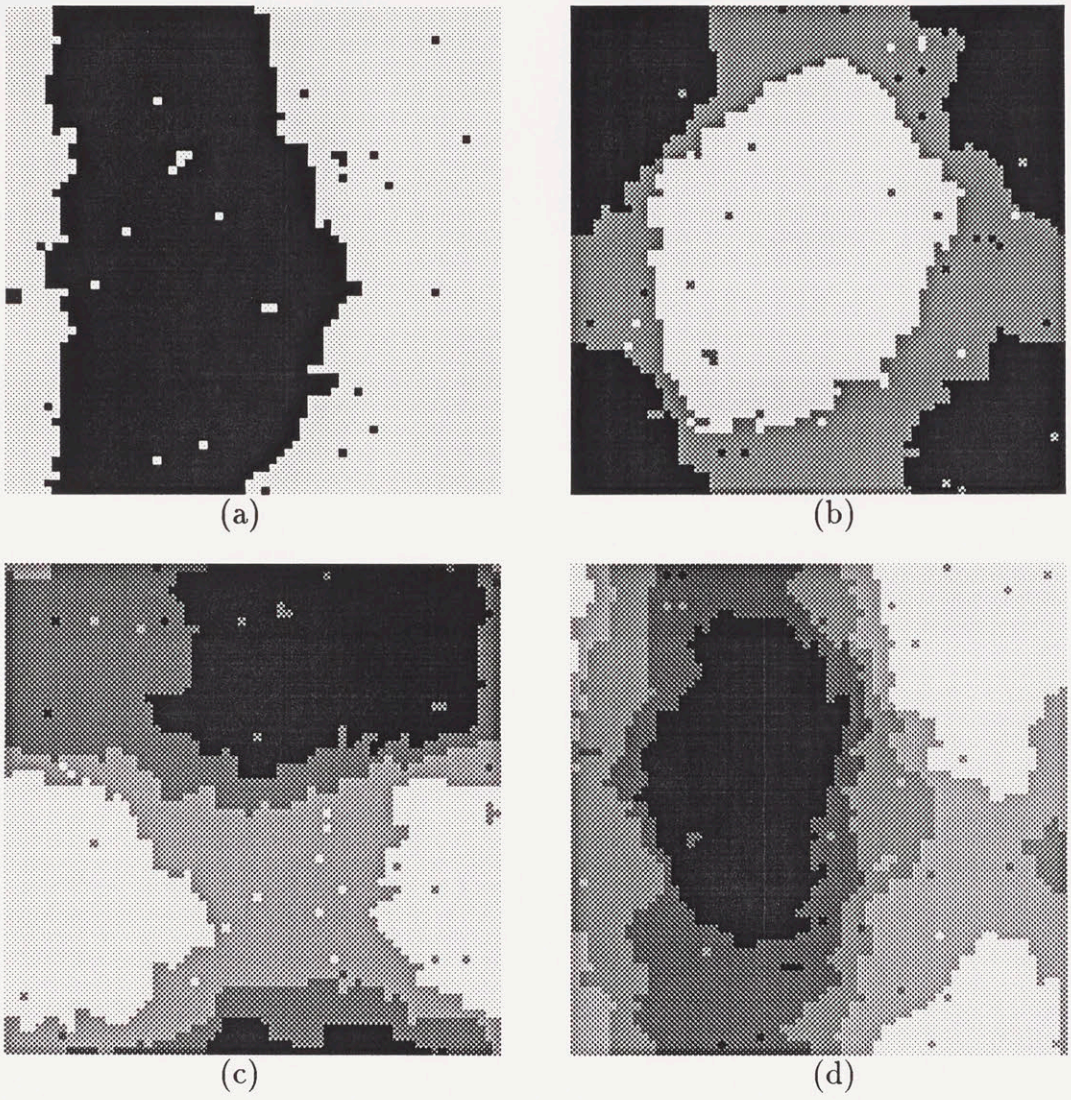

Figure 3-3: Examples of near-minimum-energy patterns for first-order MRF's with postive isotropic bonding parameters. Images (a), (b), (c), (d) correspond to 2, 3, 4, 5 graylevels respectively. Each image is 64×64.

---

2 to 5. These patterns are close to their ground states in appearance so that the minimum energy miscibility behavior is easily seen.

In (a) the blacks and whites separate as $m(1,1)$ is maximized. As white mixes only with white, black is forced to mix only with black. If the synthesis of this energy function were done using a non-exchange method such as the Gibbs Sampler with no histogram constraints, the ground state would be solid white. The black remains only because the uniform histogram is enforced by the Metropolis exchange.

In (b) the sum of $m(1,1)$, $4m(2,2)$, and $4m(1,2)$ is maximized. Graylevel 2 forms a blob while maximizing the presence of graylevel 1 along its boundary. Graylevel

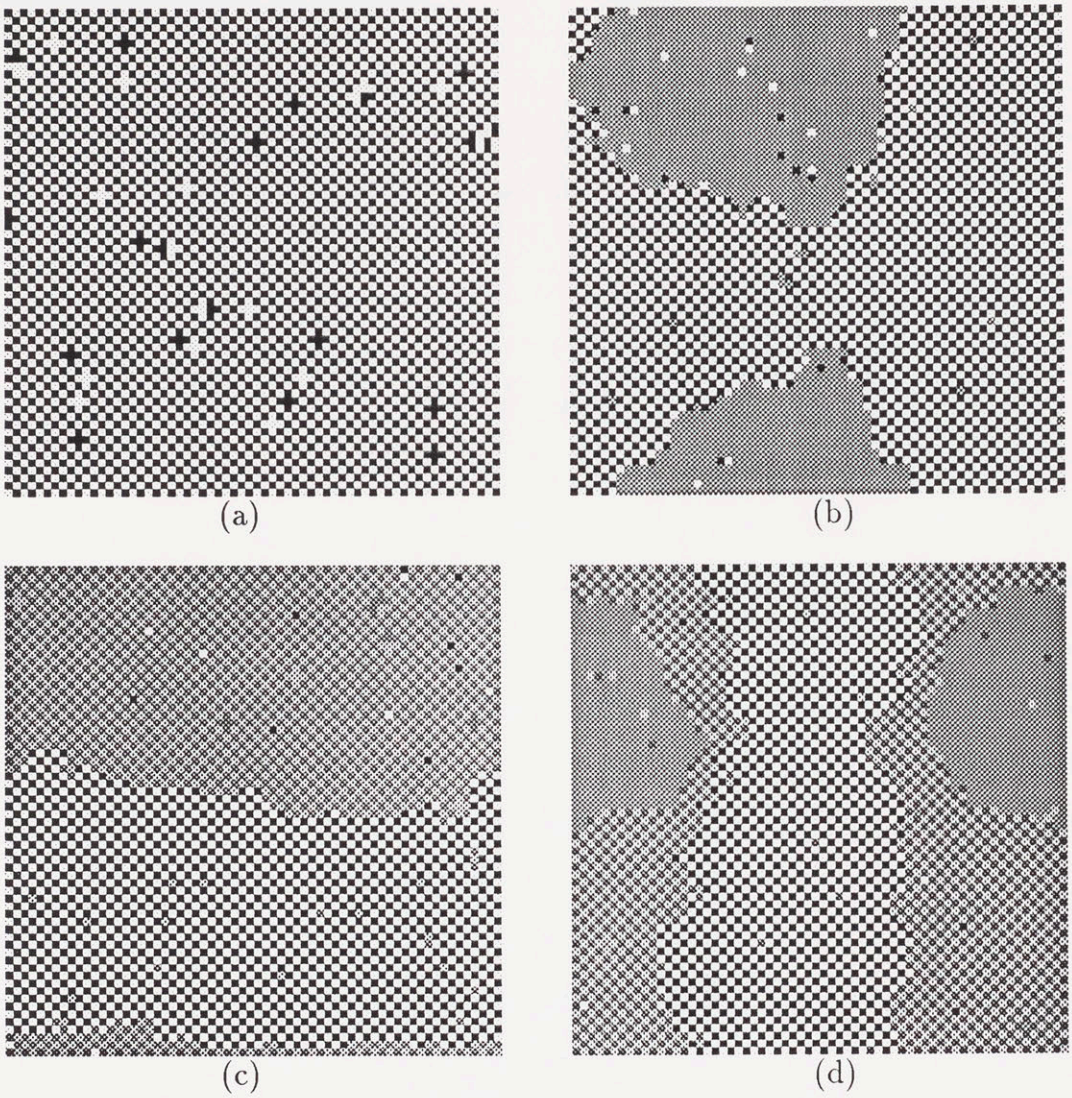

Figure 3-4: Examples of near-minimum-energy patterns for first-order MRF's with negative isotropic bonding parameters. Images (a), (b), (c), (d) correspond to 2, 3, 4, 5 graylevels respectively. Each image is 64×64.

---

0 has no other choice but to form a blob. The image in (c) and images made with higher numbers of graylevels have similar explanations which derive from intuition about separation.

For negative isotropic parameters, the behavior of the auto-binomial MRF is easily described by graylevel mixing. Consider Figure 3-4 which is identical to that of Figure 3-3 with the exception of the sign of β.

In (a) a checkerboard is being made to minimize $m(1,1)$ (white self-miscibility). The terms $m(0,0)$ and $m(0,1)$ are multiplied by zero and can be ignored. The optimal configuration is to move blacks between all the whites so that the miscibility of the

whites goes to zero.

In (b) the sum of $m(1,1)$, $4m(2,2)$, and $4m(1,2)$ is minimized. The last two terms have the greatest weight and can be interpreted as color 2 (white) trying to form a mixture, but not with itself or color 1 (gray). This leaves the configuration of a checkerboard between colors 0 (black) and 2, with color 1 forming a blob off by itself. There is an apt saying for this behavior: "if you're not part of the solution, then you're part of the precipitate."

The term $m(1,1)$ can be further minimized if there is a fourth color to mix with it. This happens in (c). The image in (d) and images made with higher numbers of graylevels have similar explanations, all deriving from intuition about mixing.

In Section 2.3.1 we mentioned that for the auto-binomial fields synthesized with the Metropolis exchange, if exchanges do not occur within the neighborhoods, then the pattern is reversible in the sense that when graylevels of value g are replaced with those of value $n-g-1$, they do not affect the overall pattern. Though we did not restrict exchanges from occurring in neighborhoods, we counted that very few (less than 1%) did occur. Thus, one would expect an approximate graylevel reversibility to show up in the texture patterns. This is the case, and it can be seen in the miscibility behavior. For example, the colors 0 (black) and $n-1$ (white) have essentially the same mixing behavior in all the samples shown in this section.

3.5.2 Boundary minimization and maximization

For the Ising model of statistical mechanics (Section 2.2.1) it is known that measuring boundary length leads to an intuitive explanation of the system's behavior [36]. The Ising model operates so as to minimize an energy function which is essentially $m(A,B)$. In the case of "spontaneous magnetization" where all spins are oriented the same way, either up or down, the boundary between A and B is minimized by becoming zero. Thus, the lattice is full of elements of the same spin; this is the *ferromagnetic* state. The opposite case, where $m(A,B)$ is maximized, corresponds to the *antiferromagnetic* state. This is the checkerboard pattern, where spins alternate and the boundary between A and B is maximized.

The cases of ferromagnetism and antiferromagnetism in the Ising model are also analogous to the separation and mixing of two fluids [56]. In aura notation, the miscibility of two fluids is represented by $m(A, B)$ [1]. For immiscible fluids $m(A, B)$ is minimized; for miscible, $m(A, B)$ is maximized. When $m(A, B)$ is normalized over some unit area, it gives a measure of the interfacial energy driving the separation of the two phases A and B [69].

The miscibility behavior of MRF's described in the previous section has another interpretation in terms of the principle of graylevel boundary length. The behavior that was described for the Ising model is an example of the boundary length optimization for the binary case. The examples in Figure 3-3 are examples of minimizing boundary length for a general number of graylevels. Similarly, Figure 3-4 gives examples of maximizing graylevel boundary length.

Since the aura measure is valid on a general lattice with any number of fluids (graylevels) $A_i, i = 0, 1, \ldots, n-1$, and any neighborhood structure, it generalizes both the boundary length and miscibility concepts.

When the lattice geometry is not square, the boundary minimization manifests itself in a slightly different way. Note that there is a geometry-dependent lower bound for the miscibility measures. Of all the configurations that separate white and black, the optimal one will minimize total boundary length. On a 32×64 lattice, this yields a left-right separation with boundary length proportional to 2×32. (There are two boundaries since the lattice is periodic).

An example of this optimization is illustrated in Figure 3-5 for graylevels 2 and 3. The parameters used to synthesize these patterns are identical to those used in Figure 3-3 (a) and (b) but the model order has been increased to fourth. The higher order neighborhood is responsible for the less noisy appearance of these patterns. Interestingly, the random fields in (a) and (b) have formed geometric objects – squares and circles.

The "minimum boundary" or in general, "minimum surface" principle is an active

[1] For two fluids, one would intuitively expect them to mix symmetrically, i.e., $m(A, B) = m(B, A)$. Note that even if this equivalence holds, it does not imply a symmetric neighborhood structure.

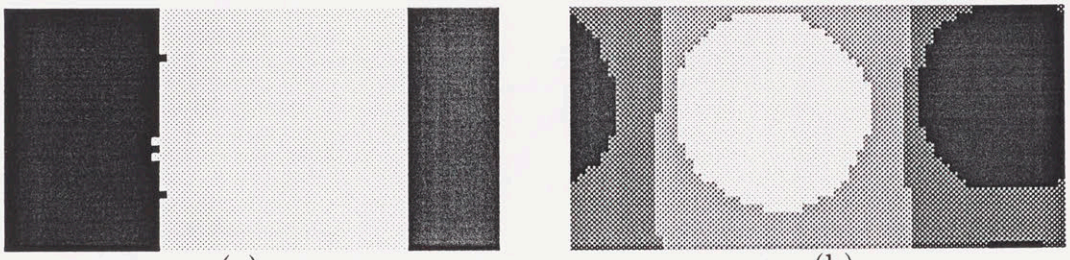

(a) (b)

Figure 3-5: Lattice geometry affects the equilibrium pattern by constraining the miscibilities between different graylevels. In (a) the separation will always make a vertical boundary since that dimension is the shortest in this 32×64 lattice. Observe that this pattern is only two exchanges from being at its minimum energy state. Similarly in (b), the two gray regions try to separate with vertical boundaries.

---

mechanism in natural texture formation. Stevens [59] illustrates many examples such as soap film partitions that minimize surface tension, melting snow on grass that clings to itself to minimize surface area, and minimum boundary arrangements of the the scales of an armadillo. We quote Stevens,

> But surface tension, close packing, cracking, and wrinkling – do they not have something in common that explains why they all produce the same pattern? In a sense, yes. The common element is that they all produce minimum surfaces. ... The technical description for all those processes is the minimization of work or energy.

We emphasize the basic mechanism at work in the minimization of the auto-MRF energy is simply boundary minimization (or maximization, depending on the sign).

3.5.3 Aura matrices: isotropic fields

The notions of boundary length and miscibility are numerically stated by the aura matrices. Aura matrices for the texture samples of Figure 3-3 (a)-(d) are shown

$$\mathbf{A} = \begin{bmatrix} 7878 & 314 \\ 314 & 7878 \end{bmatrix}$$

(a)

$$\mathbf{A} = \begin{bmatrix} 5174 & 286 & 0 \\ 286 & 4904 & 270 \\ 0 & 270 & 5194 \end{bmatrix}$$

(b)

$$\mathbf{A} = \begin{bmatrix} 3850 & 246 & 0 & 0 \\ 246 & 3598 & 252 & 0 \\ 0 & 252 & 3594 & 250 \\ 0 & 0 & 250 & 3846 \end{bmatrix}$$

(c)

$$\mathbf{A} = \begin{bmatrix} 3072 & 204 & 0 & 0 & 0 \\ 204 & 2828 & 244 & 0 & 0 \\ 0 & 244 & 2794 & 238 & 0 \\ 0 & 0 & 238 & 2836 & 202 \\ 0 & 0 & 0 & 202 & 3078 \end{bmatrix}$$

(d)

Figure 3-6: Aura matrices corresponding to textures in Figure 3-3 (a) – (d).

---

in Figure 3-6, and those of Figure 3-4 (a)-(d) are shown in Figure 3-7. Note that the auras were all formed with first order neighborhoods ($|\mathcal{N}| = 4$) as the texture samples are all first order MRF's. The Aura Matrix Properties are easily checked for the $|\mathcal{S}| = 64 \times 64$ lattices used here. Observe that all of the aura matrices are tridiagonal for the positive case, and anti-tridiagonal for the negative case. This characteristic behavior is derived mathematically in Chapter 6.

Following (3.7), the aura matrices in these figures are a sum of four co-occurrence matrices with $|\mathbf{d}| = 1$. The diagonal dominance of co-occurrence matrices has long been understood to relate to texture clumpiness [55] though no precise relation has ever been formulated. Here we have a precise formulation of this clumpiness in the aura measures. One can also conclude because of the nonnegativity of co-occurrences, that the four co-occurrences with $|\mathbf{d}| = 1$ will be tridiagonal (positive case) or anti-tridiagonal (negative case). These are the first relationships we know of that relate a particular model to co-occurrence matrix structure.

$$\mathbf{A} = \begin{bmatrix} 138 & 8054 \\ 8054 & 138 \end{bmatrix}$$

(a)

$$\mathbf{A} = \begin{bmatrix} 0 & 170 & 5290 \\ 170 & 5116 & 174 \\ 5290 & 174 & 0 \end{bmatrix}$$

(b)

$$\mathbf{A} = \begin{bmatrix} 0 & 0 & 159 & 3937 \\ 0 & 34 & 3903 & 159 \\ 159 & 3903 & 34 & 0 \\ 3937 & 159 & 0 & 0 \end{bmatrix}$$

(c)

$$\mathbf{A} = \begin{bmatrix} 0 & 0 & 0 & 140 & 3136 \\ 0 & 0 & 100 & 3032 & 144 \\ 0 & 100 & 3072 & 104 & 0 \\ 140 & 3032 & 104 & 0 & 0 \\ 3136 & 144 & 0 & 0 & 0 \end{bmatrix}$$

(d)

Figure 3-7: Aura matrices corresponding to textures in Figure 3-4 (a) - (d).

3.5.4 Aura matrices: anisotropic fields

An important consequence of the linear formulation of (3.10) is that the aura matrices of anisotropic texture patterns will be a sum of the aura matrices for the isotropic sub-neighborhoods. An example of the superposition of aura matrices in the anisotropic case is shown in Figure 3-8. Here, the magnitudes of the bonding parameters are equal, $|\beta_k| = 1$, but the signs vary. Note that $\mathbf{A} = \mathbf{A}^1 + \mathbf{A}^2$.

The superposition result imposes additional constraints on the types of structure that can appear in co-occurrence matrices of these textures. More significantly, the patterns which can exist in textures modeled by the ground states of the MRF may be severely constrained. For example when $n = 5$, $m(0,2) = m(2,0)$ and $m(2,4) = m(4,2)$ may be forced to be zero in the ground state. These important issues are discussed in more detail in Chapter 6.

The previous anisotropy was with equal magnitudes, varying signs. Now consider anisotropy with β_k of varying magnitude. As the relative magnitudes of the parameters are changed the relative weights of the miscibilities change. Figure 3-9 shows

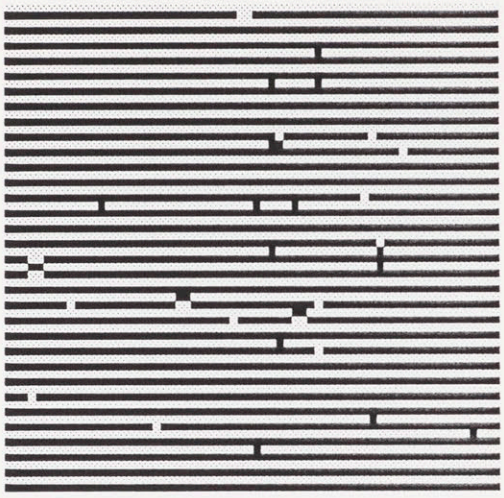

$$\mathbf{A}^1 = \begin{bmatrix} 4030 & 66 \\ 66 & 4030 \end{bmatrix}$$

$$\mathbf{A}^2 = \begin{bmatrix} 64 & 4032 \\ 4032 & 64 \end{bmatrix}$$

$$\mathbf{A} = \begin{bmatrix} 4094 & 4098 \\ 4098 & 4094 \end{bmatrix}$$

Figure 3-8: The pattern on the left was synthesized using a binary MRF with $\beta_1 = 1$ (horizontal) and $\beta_2 = -1$ (vertical). The aura matrices for the two isotropic sub-neighborhoods are shown to illustrate that their superposition gives the anisotropic aura matrix.

---

patterns with parameters $\beta_1 = 1$, $\beta_2 = 1$ on the left, and $\beta_1 = 1$, $\beta_2 = 2$ on the right. The stronger vertical clustering is apparent on the right.

The anisotropy has an analogous influence in the negative case. In Figure 3-10, the parameters are $\beta_1 = -1$ (horizontal), $\beta_2 = -1$ (vertical) on the left and $\beta_1 = -1$, $\beta_2 = -2$ on the right. Here the stronger vertical parameter is manifested as vertical crystal defects. These result because the repulsion between vertical pairs is stronger than the repulsion between horizontal pairs.

In the next chapter we take a closer look at the behavior of the bonding parameters with respect to temperature, and show how they can be interpreted as miscibility rates.

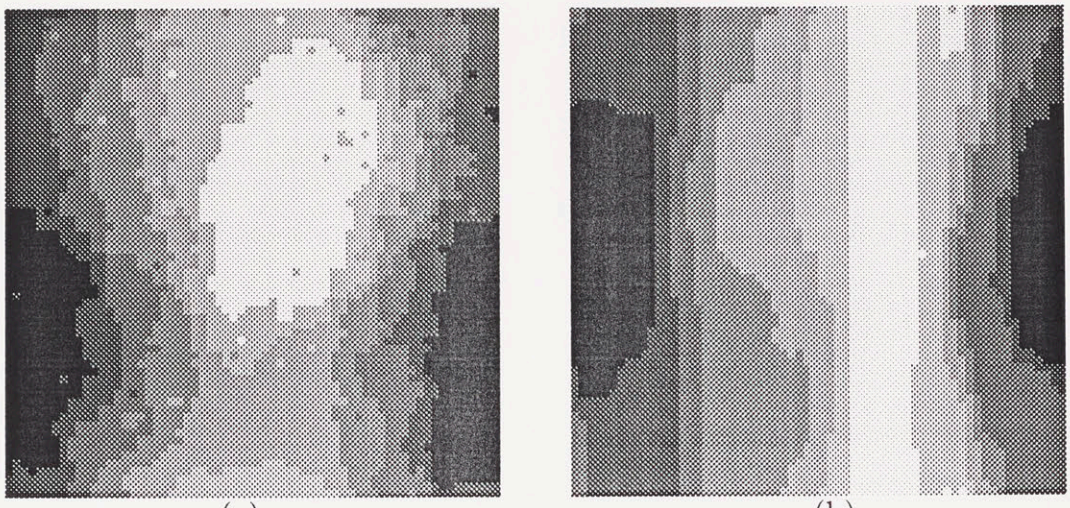

(a) (b)

Figure 3-9: Comparison of isotropic (a) and anisotropic (b) positive parameters. The vertical parameter in (b) has twice the value of the horizontal parameter. Both images have 7 graylevels and are 64×64.

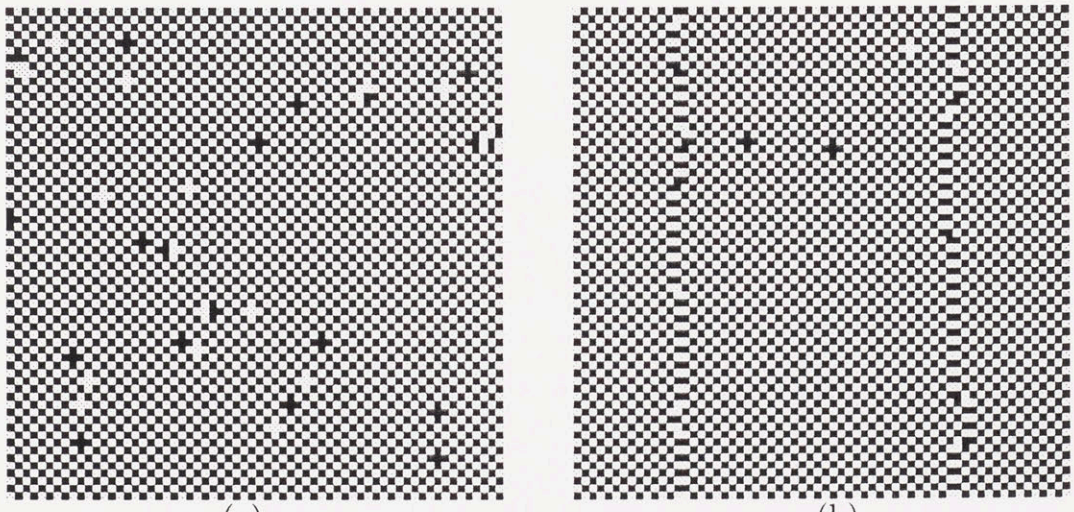

(a) (b)

Figure 3-10: Comparison of isotropic (a) and anisotropic (b) negative parameters. The vertical parameter in (b) has twice the value of the horizontal parameter so its defects favor vertical repulsion. Both images have 2 graylevels and are 64×64.

Chapter 4

Temperature and texture parameters

4.1 Introduction

A herringbone fabric looks textured from only a certain range of distances. If too close, you see threads; if too far it looks smooth. In general textures are characterized by behavior at different scales.

A separation into different scales can be achieved by varying temperature. This ability of temperature is the key motivation behind the use of simulated annealing for solving large optimization problems. Kirkpatrick *et. al.* [37] state, "the temperature distinguishes classes of rearrangements, so that rearrangements causing large changes in the objective function occur at high temperatures, while the small changes are deferred until low temperatures."

The process of annealing to obtain a regular crystal structure without defect requires very slow lowering of temperature. The intuition is that at high temperature the components of the crystal can move freely over large scale, whereas at low temperature the mobility is less and restricts changes to small scales.

The indirect use of temperature in Markov/Gibbs random fields (MRF)'s for image restoration, compression, segmentation, and classification has been widespread. In these applications it is typically assumed that the MRF is a prior for the original

image, which may have texture. The resulting posterior distribution is then maximized using some variation of simulated annealing. The effects of temperature on the optimization have been studied, but the effects of temperature on the underlying texture have been mostly ignored. Marroquin [42] comments that temperature controls average cluster size and density but does not elaborate.

This chapter begins the investigation of the effects of temperature on MRF texture formation. We use the aura matrix developed in the previous chapter to characterize the textures. In Section 4.2 several behaviors of the MRF are illustrated which indicate that the MRF bonding parameters do not uniquely characterize a texture pattern. Next, in Section 4.3 the anisotropic MRF energy function is rewritten to show that the bonding parameters can be interpreted as annealing rate constants. The rates are not easy to determine though – they vary depending on what temperature range the MRF is in. In Section 4.4 texture formation at a given constant temperature is examined. An application of temperature to synthesizing smoothly varying periodic patterns is discussed in Section 4.5.

4.2 Texture description without temperature

Studies of MRF's as texture models have not included the effects due to temperature changes. The bonding parameters, β_k, have been assumed to be the parameters which characterize a texture. In this section we illustrate behavior indicating that these parameters do not characterize a texture pattern in the way that has been assumed in the literature. Moreover, we show that the texture may also vary when the number of graylevels is changed. The observations in this section are supported empirically; more formal analysis will follow.

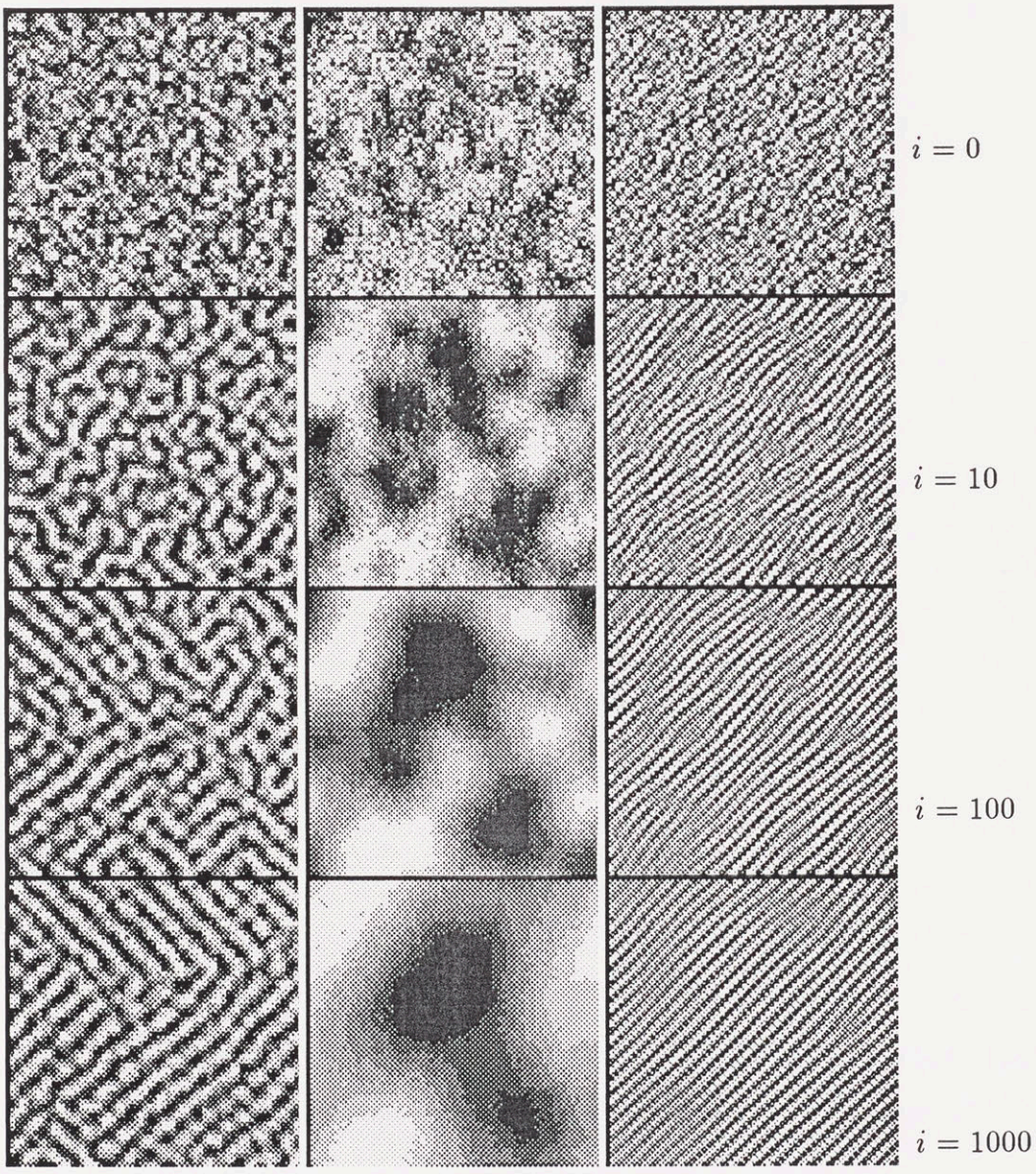

Figure 4-1: In each column, four 64×64 samples of an MRF are shown. The parameters in (a) are $\beta_1 = \beta_2 = \beta_3 = \beta_4 = 0.2$, and $\beta_5 = \beta_6 = \beta_7 = \beta_8 = -0.1$, (b) $\beta = 0.5$, and (c) $\beta_1 = \beta_2 = \beta_3 = \beta_5 = \beta_6 = -0.4$, $\beta_4 = 0.4$.

4.2.1 Observation: one set of parameters and many patterns

We first illustrate texture formation using three different sets of parameters. In Figure 4-1 twelve 64×64 samples with $n = 8$ are shown. Within a column all the samples have the same set of parameters. Each was also synthesized at a constant temperature, $T = 1$ (no annealing). The rows correspond to sampling after the 0, 10, 100, and 1000 iterations of the Metropolis exchange algorithm.

The first row shows the effect of one iteration of the synthesis on an initial uniform random image. In the second row are textures which were said to have "converged" according to the criteria of [16, 17, 26]. Patterns synthesized with about 10-15 iterations, like those in the second row, have been shown to correspond nicely to stochastic natural texture patterns. It has been assumed that the values of the MRF bonding parameters correspond to textures formed at this stage of the synthesis process.

What we have done that is new in this example is simply to run the synthesis process a couple orders of magnitude longer. Although the patterns are changing quite slowly, after 100 and 1000 iterations (rows three and four) the patterns are perceptually different. That is, in each column, one set of parameters is generating more than one type of texture pattern.

This example indicates that the textures which were believed to have "converged" have not stopped changing. In Section 5.3 criteria for convergence will be addressed. For now let us consider the other side of the uniqueness issue: can the same pattern be generated from more than one set of parameters?

4.2.2 Observation: one pattern from many sets of parameters

Consider a defective checkerboard pattern, analogous to the pattern which forms when a regular crystal is cooled too fast. In Figure 4-2 two examples of this structure made with an auto-binomial MRF are shown. The one on the left is the same as the

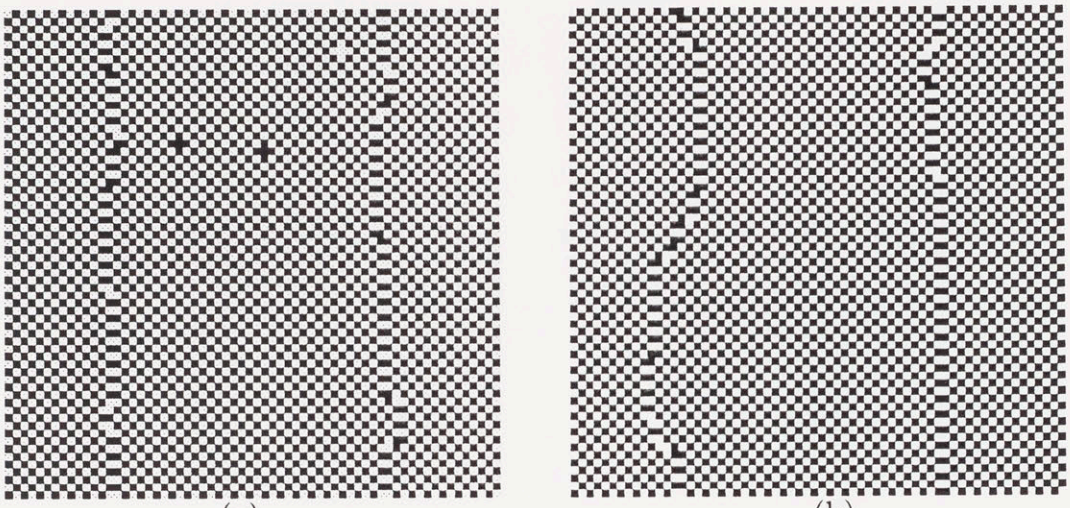

(a) (b)

Figure 4-2: The pattern in (a) is the same as the anisotropic case in Figure 3-10(b); its parameters are $\beta_1 = -1$, $\beta_2 = -2$. The pattern in (b) was made with *isotropic* parameters, $\beta_1 = \beta_2 = -1$. The only other difference in their synthesis is the annealing rate; in (a) it is $c = 2.7$ and in (b) it is $c = 0.27$. Both images have 2 graylevels and are 64×64.

---

anisotropic case of Figure 3-10, having parameters $\beta_1 = -1$, $\beta_2 = -2$. One might expect the pattern in (b) was made with the same parameters; however, it is actually made with isotropic parameters, $\beta_1 = \beta_2 = -1$. The only other difference in these two patterns is the annealing rate; in (a) it is $c = 2.7$ and in (b) it is $c = 0.27$. The isotropic aura matrices differ by less than 0.1 % for the two patterns.

Thus we have a set of isotropic parameters and a set of anisotropic parameters which generate the same type of pattern. Consider the functions being maximized for each of these sets of parameters. Using the linear aura measure formulation of (3.12), the energy minimized for (a) is

$$m^1(1,1) + 2m^2(1,1), \tag{4.1}$$

and for (b) is:

$$m^1(1,1) + m^2(1,1). \tag{4.2}$$

With the uniform histogram constraint a checkerboard can be formed so that $m^1(1,1) =$

$m^2(1,1) = 0$. Hence the checkerboard configuration minimizes both (4.1) and (4.2). In other words the checkerboard will be the ground state for both; the two different sets of parameters lead to the same ground state pattern.

It follows that neither of the patterns shown in Figure 4-2 is a minimum energy pattern. Notice that the energy in (4.1) is lower than it would be if the defects in Figure 4-2 (a) were horizontal instead of vertical. The vertical defects are favored by the non-optimal state, and were probably caused because the rate of mixing in the vertical direction exceeded that in the horizontal direction. (This explanation will be justified in Section 4.3.) In Figure 4-2 (b) there is no reason to favor any one orientation of the defects. Their structure is unpredictable; the defects are caused by the rapid quenching of the temperature which is performed homogeneously.

For arbitrary large n and anisotropic patterns it is generally very difficult to determine if a pattern is in its ground state. Theoretically, using stochastic relaxation the pattern can never get stuck in a local minima while $T > 0$; thus it will get to its ground state provided one waits what is sometimes an impossible length of time. This means that *eventually* both the defective checkerboard patterns will become perfect checkerboards.

The lack of unique correspondence between bonding parameters and texture pattern should be no surprise. In the equilibrium MRF there is a condition of *positivity* which states that for all configurations, $\mathbf{x}$, the probability $P(\mathbf{x}) > 0$. Thus, unless we are in the ground state, *all configurations are possible* even though some are more likely than others.

In summary we have constructed examples to make the following points:

- One set of parameters may produce a variety of patterns simply by iterating longer;
- A single ground state can correspond to more than one set of parameters;
- A non-ground state can correspond to more than one set of parameters.

This difficulty in matching bonding parameters to a given texture continues in the next section where it is shown that changing the number of graylevels can also alter

the texture.

4.2.3 Observation: different graylevels and different patterns

Many texture models work with a reduced number of graylevels. Fewer graylevels means fewer possible configurations and can vastly shrink the space over which an optimizing search is being conducted. Usually the number of graylevels, n, can be reduced without significantly destroying the percept of the texture – the resolution should only look a little worse. Similarly, increasing n should improve the resolution without changing the basic texture that is perceived.

A texture model that works with a reduced number of graylevels should respond similarly: by allowing more graylevels the resolution should increase but the image texture should stay the same. However, this is not necessarily the behavior when n is changed in the auto-binomial MRF.

In Figure 4-3 all twelve textures were synthesized using the first order isotropic parameters, $\beta = 1$. Samples of the MRF with graylevels $n = 2,\ 4,\ 16$ are plotted left to right at iterations, $i = 0,\ 10,\ 100,\ 1000$, from top to bottom. All of these samples are synthesized with constant temperature, $T = 1$.

For $n = 2$ graylevels the texture does not change appearance, even after a thousand iterations. However, as n is increased the pattern changes with respect to both n and i. For $n = 4$ and $n = 16$ graylevels it looks like the pattern is being zoomed closer to the viewer. It is as if the scale is changing, not the resolution. The $n = 16$ column also appears to be zoomed more than the $n = 4$ one.

In Figure 4-4 the same examples are given for the repulsive fourth order field with isotropic $\beta = -1$. Again, the first column looks identical over time, but the cases for $n = 4, 16$ change with iterations over time.

Previously [17] it was suggested that an increase in graylevel corresponds to an increase in perceived smoothness of the texture. This appears to be true in both Figures 4-3 and 4-4 for $i = 0, 10$. However, by iterating longer, we now show that

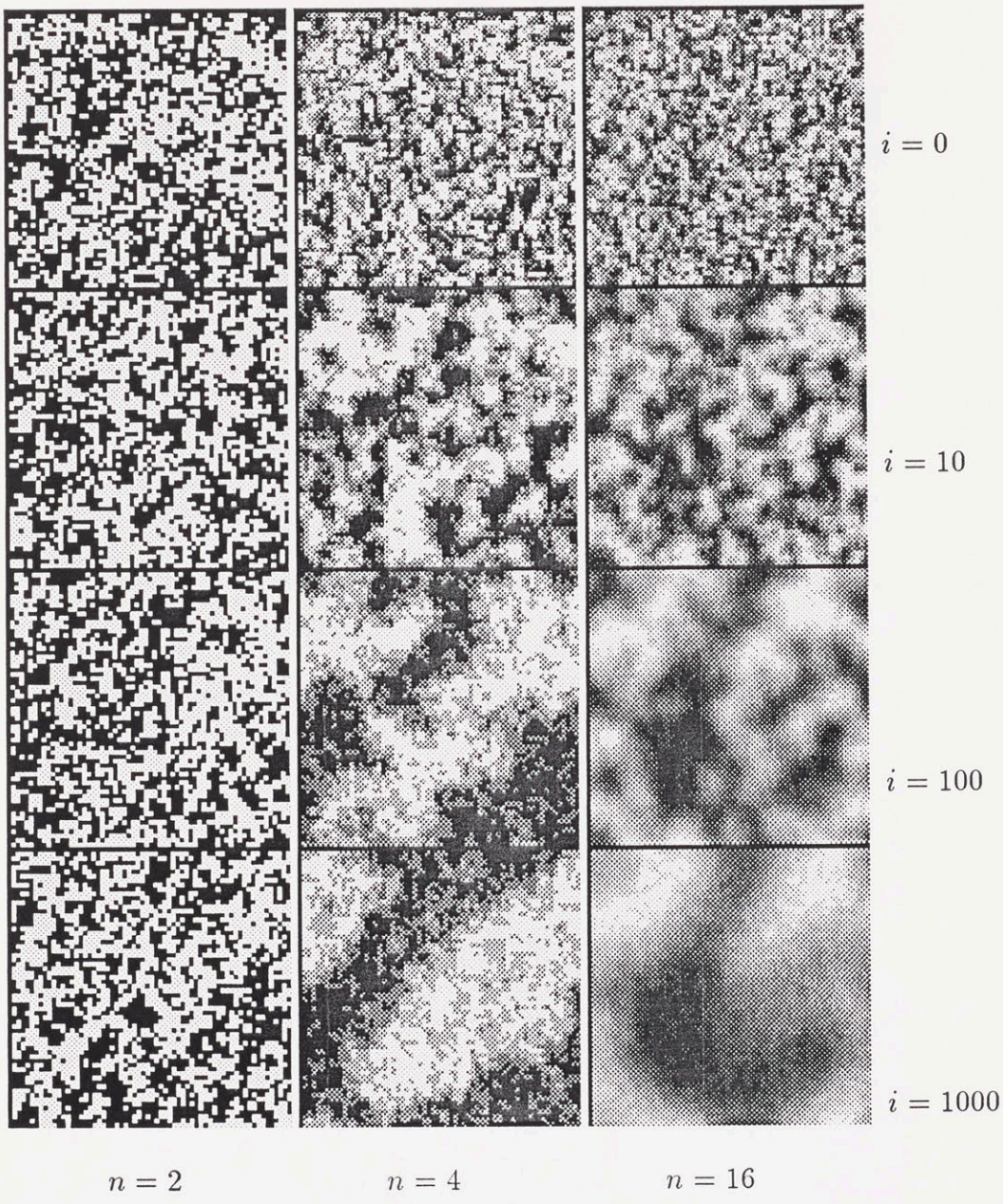

Figure 4-3: Effect of graylevels on texture. All twelve 64×64 textures have isotropic first order parameters $\beta = 1$. The number of graylevels is $n = 2, 4, 16$ from left to right and the number of iterations is $i = 0$, 10, 100, 1000, from the top to the bottom. For $n = 2$ the texture does not change appearance even after a thousand iterations. For $n = 4, 16$ the pattern changes with both graylevel and iteration.

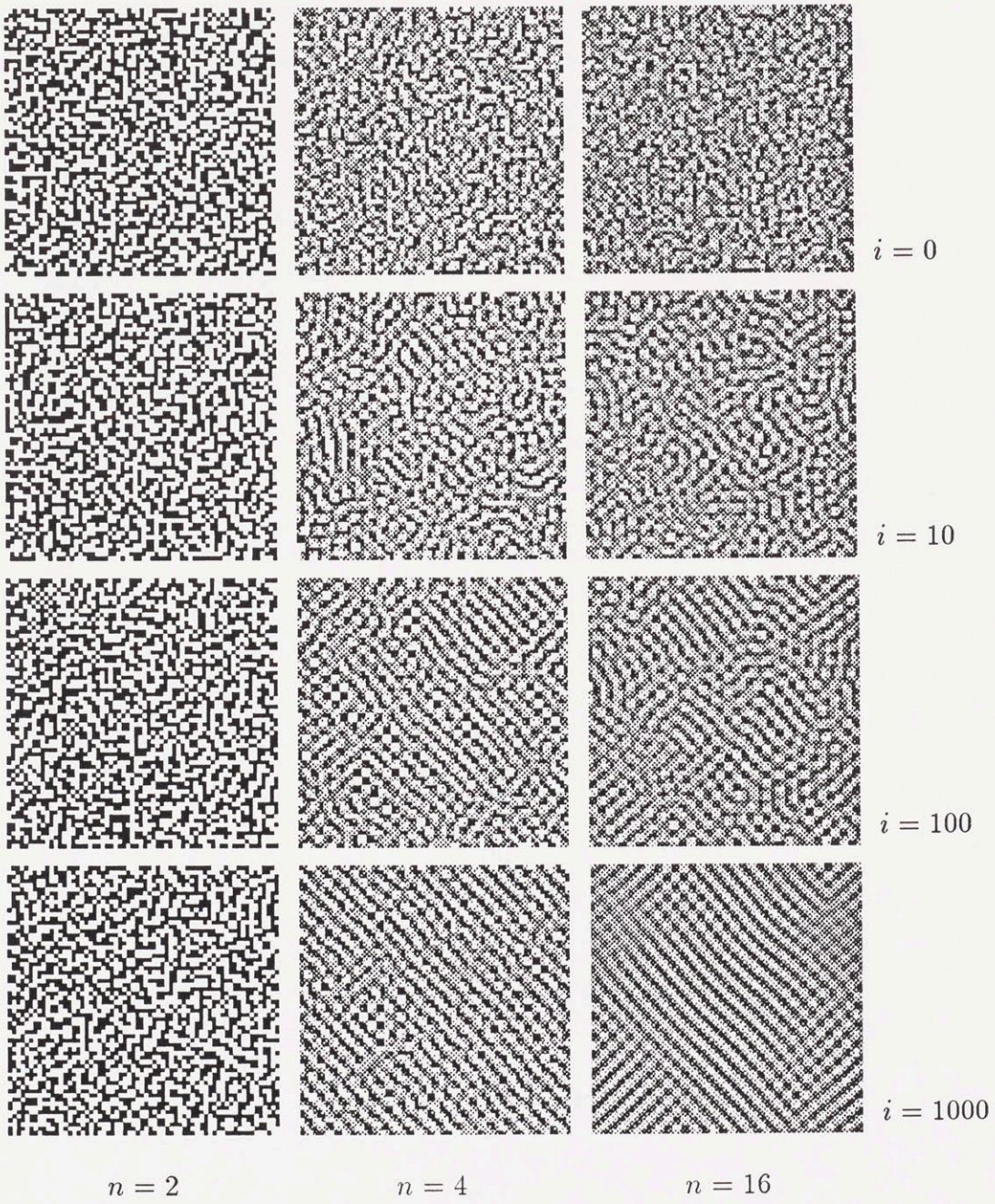

Figure 4-4: Effect of graylevels on texture. This figure is the same as Figure 4-3 except the MRF now has fourth order isotropic parameters, $\beta = -1$.

for $i = 100, 1000$, the pattern changes significantly as the graylevel is varied. Thus, the "increase in smoothness" is not always valid.

We have illustrated two basic behaviors: First, at constant graylevel the pattern changes with respect to iteration for some fixed graylevels, e.g., 16, but not for others, e.g., 2. Second, over some fixed number of iterations, e.g., 10, the pattern looks "smoother" as the graylevel is increased but for other iterations, e.g., 1000, the pattern changes completely.

In summary, these behaviors make it very difficult to describe the effect of a given number of graylevels or iterations on a texture pattern. For anisotropic textures the complexity of the behavior is even greater.

Up until now the role of temperature has been ignored. By including temperature in the model and studying its effects we will develop new explanations for the above phenomena which will help characterize textures. In the rest of this chapter we begin the formulation of these explanations. This formulation is continued in Chapter 5 with the idea of a transition temperature.

4.3 Texture parameters as temperature annealing rates

In the temperature annealing schedule given in (2.9) the constant c is understood to be proportional to how slow the annealing progresses. From substituting the iteration-dependent temperature of (2.9) into (2.2) we obtain,

$$P(\mathbf{x}) = \frac{1}{Z} \exp\left(-\frac{\log(\lfloor \frac{i}{i_{eq}} \rfloor + 1)}{c} E(\mathbf{x}) \right), \tag{4.3}$$

or equivalently,

$$P(\mathbf{x}) = \frac{1}{Z} \left(\frac{1}{(\lfloor \frac{i}{i_{eq}} \rfloor + 1)^{1/c}} \right)^{E(\mathbf{x})} = \frac{B}{Z}^{E(\mathbf{x})},$$

where $B = \exp(-1/T)$ is the new base of the exponent. For a given energy, changing the temperature is merely changing the base of the exponent. As the number of

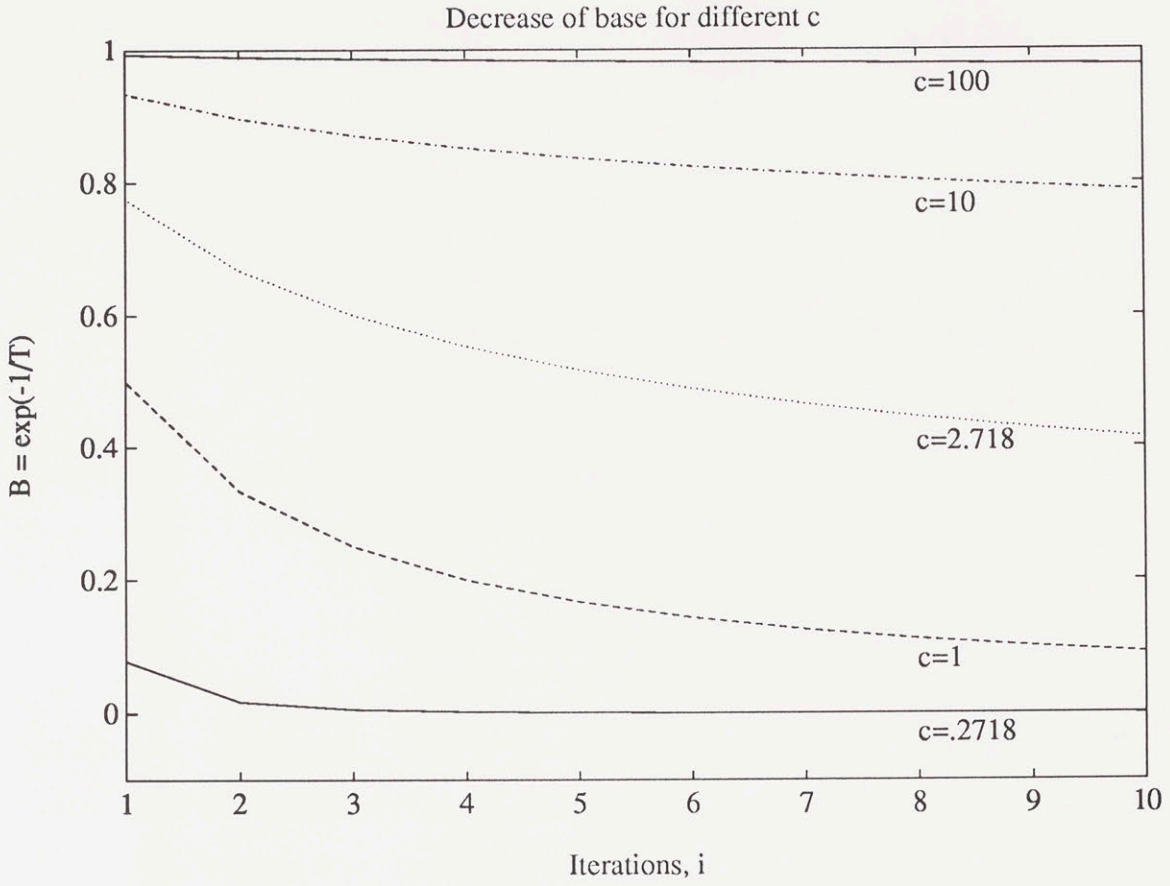

Figure 4-5: As the annealing rate c decreases, $e^{-1/T}$ goes to zero faster.

iterations i increases, T and hence B decrease. The larger the value of c, the slower the base changes and the slower the annealing progresses. For $c < 1$ i.e., very cold temperature, B shrinks rapidly to zero. Values of B at different annealing rates are shown in Figure 4-5.

Now we derive a new interpretation of the MRF bonding parameters as rate constants for the annealing in each of the miscibility directions. Thus, each parameter controls how fast the mixing progresses in each direction.

4.3.1 Formulation

We consider the auto-binomial model although a similar procedure can be followed for the Potts energy and for any other forms of the Gibbs potential, $V^k(g, g')$.

Let $\mathbf{A}^k$ be the matrix of aura measures on the subneighborhood $\mathcal{N}^k$, and let

$\mathbf{g} = [0, 1, \ldots, n-1]^T$. The formulation follows from substituting the auto-binomial energy function into (4.3).

$$P(\mathbf{x}) = \frac{1}{Z} \prod_{k=1}^{K} \exp\left(\frac{\log(\lfloor \frac{i}{i_{eq}} \rfloor + 1)}{c} \beta_k \mathbf{g}^T \mathbf{A}^k \mathbf{g} \right).$$

Now let

$$T_k = \frac{c/\beta_k}{\log(\lfloor \frac{i}{i_{eq}} \rfloor + 1)},$$

and $E^k(\mathbf{x}) = -\mathbf{g}^T \mathbf{A}^k \mathbf{g}$, the portion of energy in the kth isotropic subneighborhood. The anisotropic MRF can then be written as

$$P(\mathbf{x}) = \frac{1}{Z} \prod_{k=1}^{K} \exp\left(-\frac{1}{T_k} E^k(\mathbf{x}) \right). \tag{4.4}$$

Note that the anisotropic bonding parameters, β_k, have been absorbed into the rate constant of T_k. It is unknown whether or not the partition function Z can be factored so that (4.4) becomes a product of independent fields. Except for Z however, each of the k directions acts like an isotropic field: each has its own annealing rate constant, which controls its progress toward its ground state.

4.3.2 Simulations

When the MRF is isotropic all the rates are the same and the pattern changes equally fast in all directions. When the rates have the same magnitude but opposite signs then mixing and separation proceed at the same rate but in different directions. The latter was illustrated by the striped sample in Figure 3-8. When the rates have the same sign but different magnitude, the separation or mixing occurs faster in some directions than in others. Figures 3-9(b) and 3-10(b) illustrate this behavior.

When the rates differ in magnitude the interaction due to the anisotropic rates of mixing and separation is much more complex, and empirically, produces much more varied and interesting textures. We examine some of these interactions later in this chapter.

It is not only the bonding parameters which affect the miscibility rate. Consider again the twelve patterns in Figure 4-3. Observe that increasing the number of graylevels also increases the apparent rate of separation. It can also be shown that increasing the order of the MRF will have this influence.

All of the following changes have similar effects on the texture pattern formation: increasing the magnitude of the bonding parameter, increasing the number of graylevels, increasing the model order (i.e., the neighborhood size), and decreasing the temperature. The common behavior is that each of these increases the absolute value of $\log(P(\mathbf{x}))$, the magnitude of the exponent of the random field.

4.4 Constant temperature texture formation

Characterizing the miscibility "rates," i.e., finding what changes they are proportional to, is very difficult. For example, the two defective checkerboard patterns shown in Figure 4-2 have the same basic textural characteristics even though their annealing rates differ by an order of magnitude. This scenario could be easily explained if both patterns had reached their ground state but this is not the case. Moreover, samples thousands of iterations away may look virtually identical to each of these – thus, the difference between successive samples does not necessarily give us a rate.

In the rest of this section we will show that the miscibility rate behavior is regulated by temperature. We begin the temperature characterization with the simplest case: texture synthesis at constant temperature. We consider first a short range ($i \leq 1000$ iterations) characterization, and then a long range characterization.

4.4.1 Energy and equilibrium

Recall that in Figures 4-4 and 4-3 the different behaviors due to different numbers of graylevel are apparent after only 10 iterations. This magnitude of iterations has also been assumed in the literature to provide the natural looking textures. Let us now consider the behavior of the Gibbs energy over the first 100 iterations of constant temperature texture synthesis.

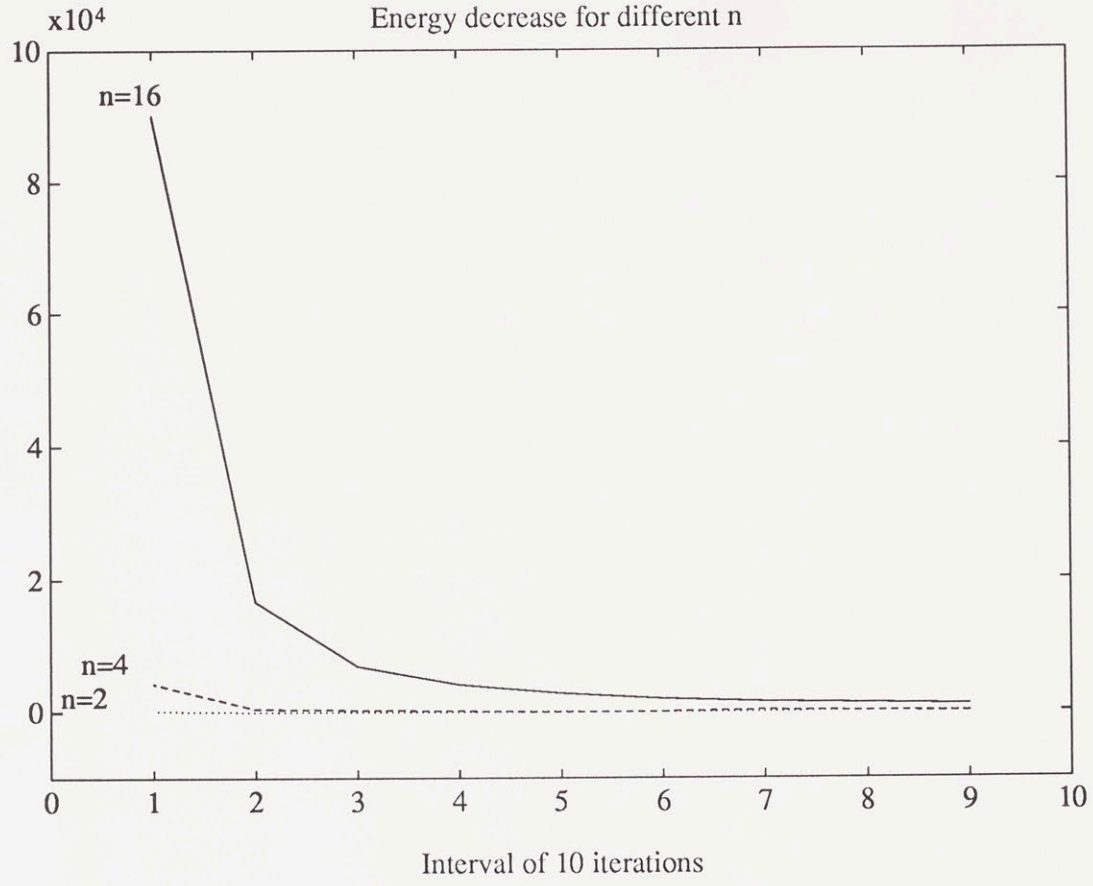

Figure 4-6: The mean energy takes longer to level off with more graylevels. These plots record the difference in mean energy over intervals of 10 iterations, for a total of 100 iterations. The energy values are from the texture samples for $n = 16, 4, 2$ which are pictured in Figure 4-3.

Constant temperature; different graylevels

At a given temperature the energy will decrease more rapidly if more graylevels are present. In Figure 4-6 we show the decrease in Gibbs energy of the three cases in Figure 4-3 over the first 100 iterations.

Each interval in the plot corresponds to ten iterations at constant temperature, $T = 1$. The value of the plot at interval I is formed by subtracting the mean Gibbs energy over interval $I+1$ from the mean Gibbs energy over interval I. For $n = 16$ the difference is large and positive at first indicating that the mean energy is decreasing rapidly over the first four intervals. The decrease is still not zero after 100 iterations, implying that the energy is not level yet. For $n = 4$ there is also an initial energy

decrease, but the energy levels after a few intervals. For $n = 2$ the energy is essentially at a constant level over all the intervals. Thus, the change of energy is consistent with the change of pattern in Figure 4-3.

Recall that i_{eq} is the number of iterations required to allow the pattern to reach equilibrium. In simulated annealing, this "equilibrium" implies that the energy levels off, i.e., the mean energy decrease is zero. In Figure 4-6 the time for the energy to level off is longer for higher n.

Using energy constancy as a measure of equilibrium, it is reasonable to conclude that column $n = 2$ in Figure 4-3 is in equilibrium after 10 iterations, and column $n = 4$ after 100 iterations. After about a thousand iterations the $n = 16$ energy decrease is also near zero, though not shown here. We caution that even if the energy level is constant the texture can still change in appearance; thus, equilibrium does not imply the pattern has stopped changing.

In the simulated annealing literature it has been observed that longer times are needed at low temperature for the field to reach equilibrium. Since increasing the graylevel has a similar effect on energy as does decreasing the temperature, it is reasonable that $n = 16$ should take longer to reach equilibrium than $n = 2$, as is confirmed in this plot. Similarly, we would expect larger neighborhood sizes or larger bonding parameter values to take longer to reach equilibrium.

A precise distance from equilibrium is not measured since it is difficult at best to determine whether or not a given sample is in equilibrium. The best we can state is that if the plot is level, it is probably in equilibrium, and the more sloped it is, the further it probably is from equilibrium.

Energy normalization for different graylevels

The energy goes up greatly with increasing graylevel. We would like to be able to normalize so that all the different graylevel cases can be treated similarly. Recall that the Gibbs energy equals

$$\mathbf{g}^T \mathbf{A} \mathbf{g}, \quad \text{where } \mathbf{g} = [0, 1, \ldots, n-1]^T,$$

so that different numbers of graylevels, n, will result in different ranges of Gibbs energy. These ranges can be brought into the same vicinity by normalizing their values at high temperature.

Assuming uniform histogram level, $|\mathcal{S}|/n$ and constant neighborhood size, $|\mathcal{N}| = \nu$, at high temperature the aura matrix will be uniform. From the Aura Matrix Properties each row or column sum equals $|\mathcal{S}|\nu/n$. Thus, the energy at high temperature has expected value

$$\frac{|\mathcal{S}|\nu}{n^2}\mathbf{g}^T\mathbf{g} = \frac{|\mathcal{S}|\nu}{n^2}\sum_{i=1}^{n-1} i \sum_{i=1}^{n-1} i = \frac{|\mathcal{S}|\nu}{n^2}\frac{(n-1)n}{2}\frac{(n-1)n}{2} = \frac{|\mathcal{S}|\nu(n-1)^2}{4}.$$

Consequently, normalizing the Gibbs energy by $(n-1)^2$ before plotting will match the values at high temperature. If lattices differ in the number of sites, $|\mathcal{S}|$, and neighborhood size, ν, then scaling by these is also necessary to align the ranges.

Constant graylevel; different temperatures

Decreasing the temperature will also cause the system to take longer to reach equilibrium. The mean energy decrease for a fixed graylevel but different values of T is shown in Figure 4-7. Here the interval is 100 iterations instead of 10 to compensate for the longer equilibration time of the data which has $n = 32$ graylevels. The behavior parallels that for Figure 4-6.

Observe that the energy is not monotonically decreasing; for $T = 100, 1000$ in Figure 4-7 the energy plot is especially noisy. Observe also that the behaviors of $T = 0.01, 10$ (and in fact $T = 0.1, 1$ which are not shown here) also cluster more tightly than that of $T = 100, 1000$. Clearly the temperature dependence is nonlinear. We will examine some important behavior of the energy variance with respect to temperature in Chapter 5.

Textures for these energy decrease plots are illustrated in Figure 4-8. Ordinarily by increasing the graylevels the pattern changes very quickly; however, here the change is offset by increasing the temperature. For $n = 32$ and $T = 1000$ the pattern is still

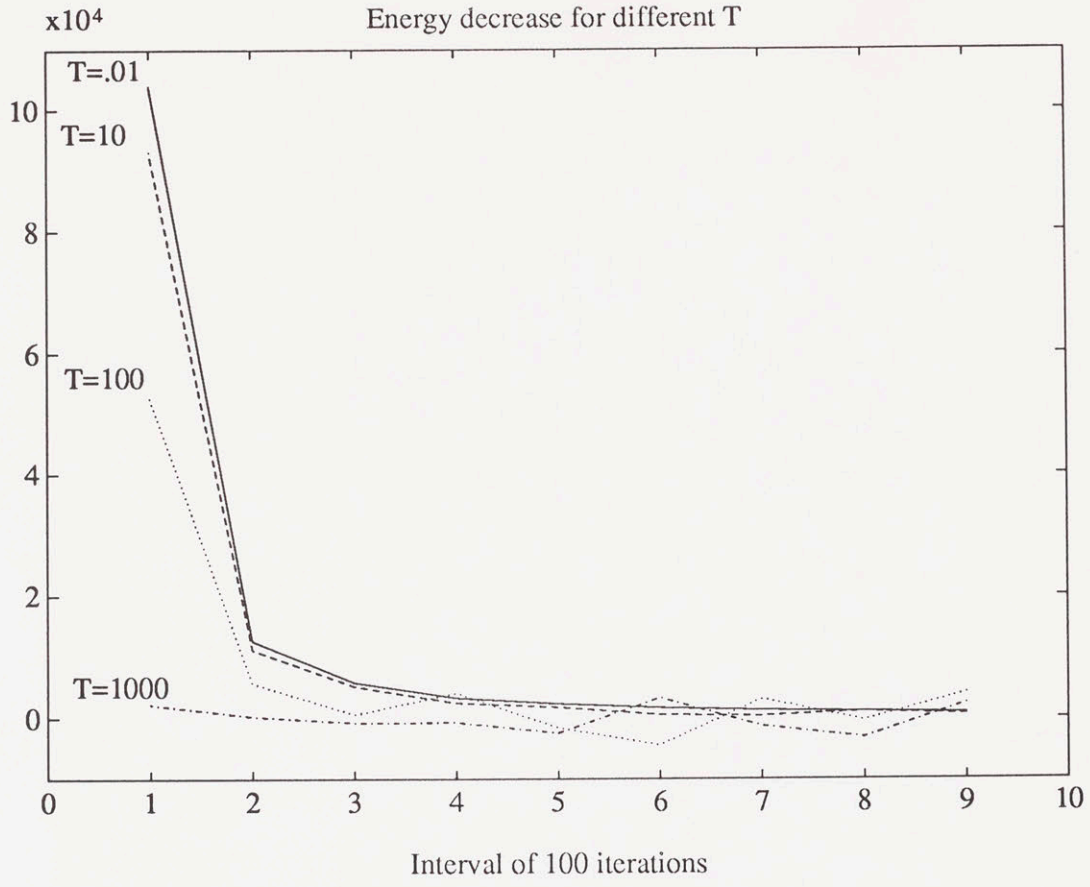

Figure 4-7: The mean energy decreases faster at lower constant temperature. These plots record the mean energy decrease over intervals of 100 iterations, for a total of 1000 iterations. The temperatures are $T = .01, 10, 100, 1000$ for $n = 32$ graylevels.

---

noisy after 1000 iterations, just as it was for $n = 2$ and $T = 1$ in Figure 4-3.

4.4.2 Aura matrix features and equilibrium

The structure of the aura matrix also changes during the equilibrating process. The aura matrix will always change when the energy changes, and may or may not change when the energy is level. The relation between aura matrix structure and energy is made more precise in Chapter 6.

We studied four features of the normalized aura matrix: its entropy and correlation (popular in co-occurrence texture analysis) and its bandwidth and trace. Examples of these for a representative 32 graylevel isotropic MRF with $p = 1$, $\beta = 1$ are discussed below.

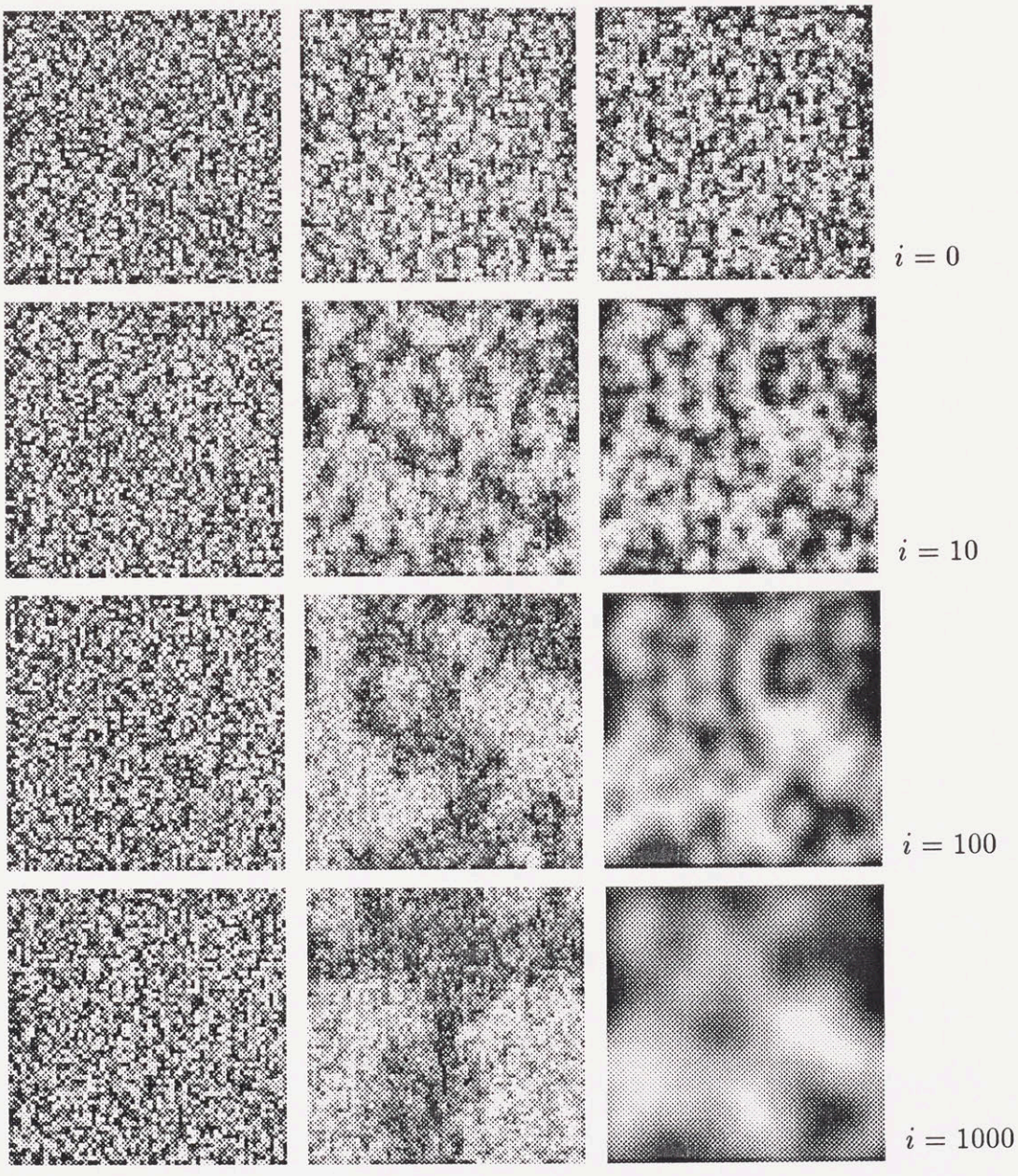

Figure 4-8: A high temperature impedes the pattern formation and a low temperature speeds it. These patterns correspond to three of the energy plots shown in Figure 4-7 at $i = 0, 10, 100, 1000$. All the samples are first order MRF's, 64×64, with $n = 32$ graylevels and $\beta = 1$.

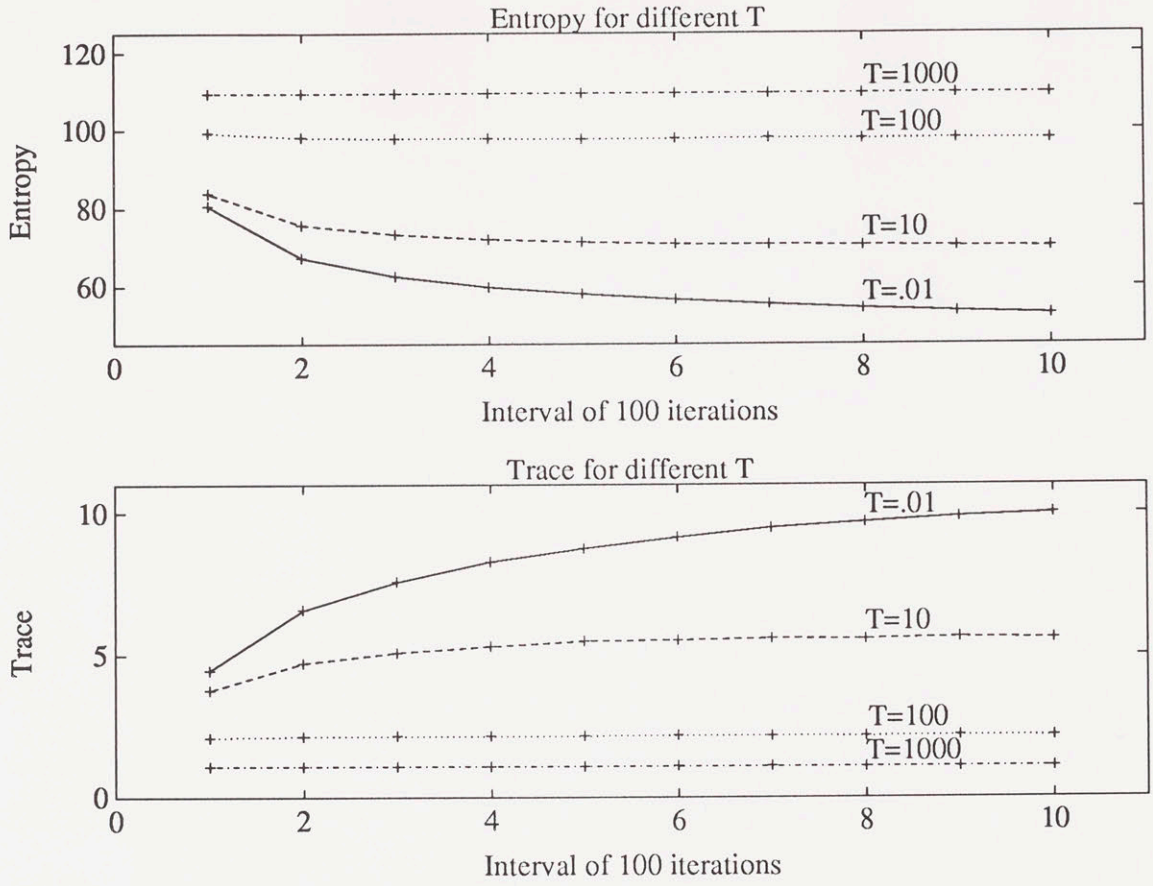

Figure 4-9: Flat curves correspond to equilibrium. The entropy of the aura matrix decreases faster at colder temperature. The aura matrix trace is nearly the reflection of the entropy; it increases faster at colder temperature. Each value shown is averaged over an interval of 100 iterations. The data is from samples of size 64×64 with $n = 32$ graylevels.

Entropy

For a random noise pattern the entropy will be at a maximum. In Figure 4-9 we see that the entropy decreases with decreasing T – this corresponds to our intuition of structure emerging at cold temperature. The height of this plot at each interval is the average entropy for the 100 aura matrices computed during that interval. The entropy is consistent with the energy in that the higher temperature patterns equilibrate fastest.

Trace

Below the entropy plots are shown the plots of the normalized aura matrix trace. Each plot was computed by averaging the traces of the 100 matrices in the interval for the given temperature. For the random initial pattern the trace of the normalized aura matrix is approximately 1 since all elements are uniformly $1/n$. These averages increase monotonically over the intervals, and faster at colder temperature. These plots nearly mirror the entropy plots; their slopes are opposite, but equilibrate after the same number of iterations.

Correlation

The correlation for the normalized aura matrix of the same data rises sharply during the first iteration, quickly approximating its maximum value of 1. The lower the temperature, the faster the rise time. This behavior is illustrated in Figure 4-10. The height at each interval is the average correlation for the 100 normalized aura matrices computed during that interval.

Bandwidth

The aura matrix is symmetric for the MRF so we characterize its bandwidth by the number of consecutive super-diagonals that have an entry greater than some threshold, typically 1% of the maximum.

A full $n \times n$ matrix has bandwidth $n - 1$. This is the most likely case at high temperature where the matrix is uniform and full band. If the element $m(0, n-1)$ is less than the threshold, the bandwidth drops to $n - 2$. If elements $m(0, n-1)$, $m(0, n-2)$ and $m(1, n-1)$ are below threshold, then the bandwidth drops to $n - 3$. For a bandwidth of k, all elements $m(i, j)$ with $|i-j| > k$ must be below the threshold.

Below the correlation plots are shown the bandwidth plots. Each plot was computed by averaging the bandwidths of the 100 aura matrices in the interval for the given temperature. It can be seen that the lower temperature bandwidths are the smallest.

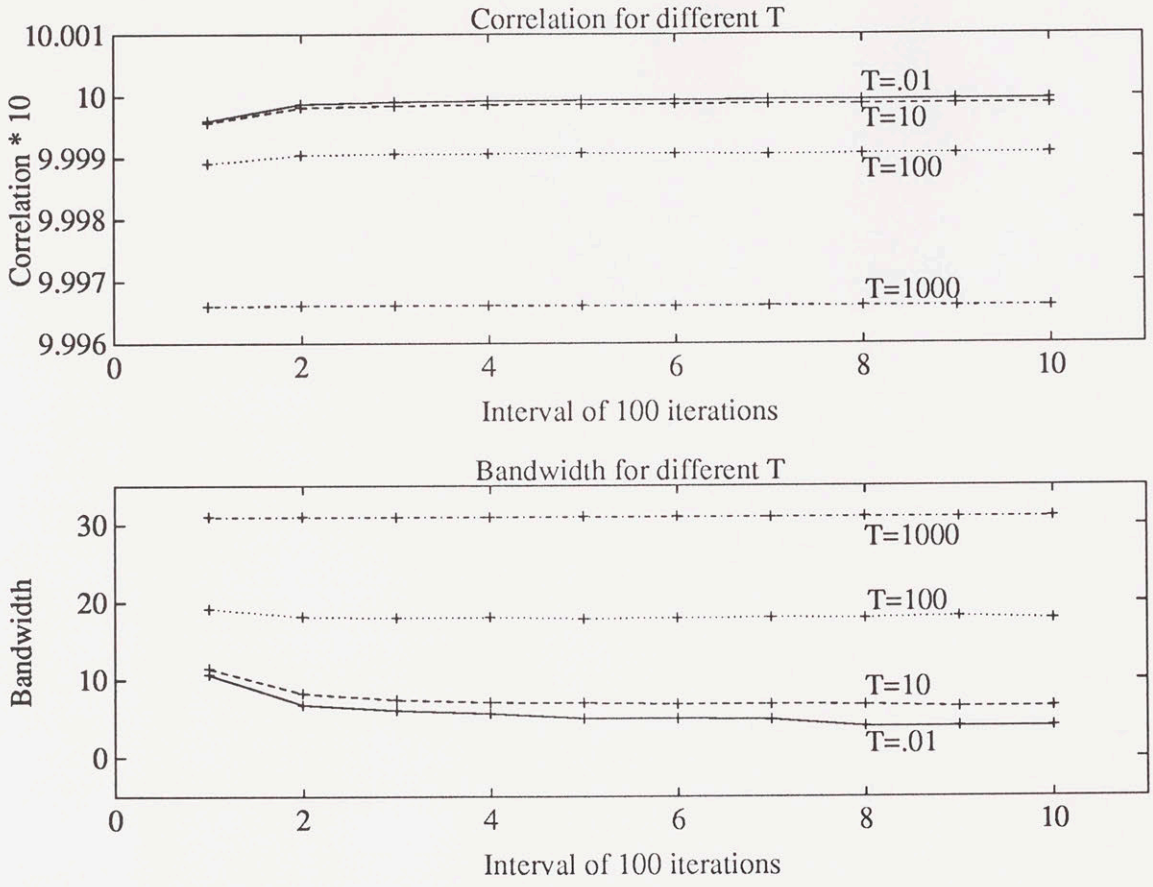

Figure 4-10: Flat curves correspond to equilibrium. The correlation increases faster at lower temperature; the bandwidth decreases faster at lower temperature. Each value shown is an average over an interval of 100 iterations. The data is from samples of size 64×64 with $n = 32$ graylevels.

As the temperature is lowered the bandwidth decreases for the attractive field. This is shown empirically here, and analytically in Chapter 6. The minimum bandwidth is 1 because of the requirement that the matrix be irreducible, i.e., it can not become diagonal. For repulsive fields the same behavior characterizes the anti-diagonal.

4.4.3 Anisotropic interaction

How does anisotropy affect equilibrium? In (4.4) it was noted that the anisotropic field cannot be completely decoupled into isotropic subfields unless Z is factorable. Therefore, we expect interaction between the isotropic fields to produce different

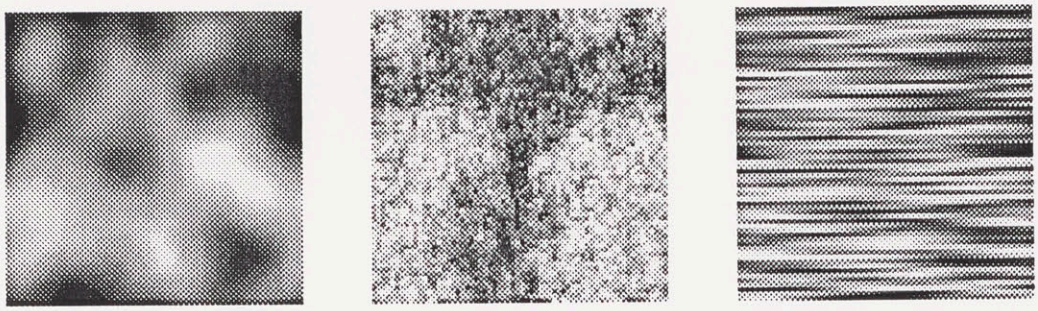

$T = .01$ $T = 100$ $T_h = .01, T_v = 100$

Figure 4-11: The first two patterns are isotropic and synthesized at constant cold $T = .01$ and hotter $T = 100$. The third is anisotropic, with bonding parameters set to simulate $T = .01$ in the horizontal direction and $T = 100$ in the vertical direction. All three are first order MRF's, 64×64, with $n = 32$ graylevels.

---

behavior in the anisotropic case.

Again, since we do not know Z this analysis is difficult and must be conducted empirically. We start with a representative anisotropic example.

Example 4.1 *We wish to compare a combination of directional behavior with its constituent isotropic behaviors. Suppose* $n = 32$ *as before but let us now simulate* $T = 100$ *in the vertical direction and* $T = 0.01$ *in the horizontal. This can be achieved by setting* $T = 1$ *and* $\beta_1 = 100$, $\beta_2 = 0.01$. *We let the synthesis run 1000 iterations without annealing, as was done for the isotropic equilibrium study. The images for the isotropic* $T = 0.01, 100$ *and anisotropic* $\beta_1 = 100, \beta_2 = 0.01$ *are shown in Figure 4-11, and the features are discussed below.*

Aura matrix features

For the isotropic case the entropy, trace, correlation, and bandwidth are computed from one aura matrix. For the anisotropic first order case there are two aura matrices, one each for the vertical and horizontal isotropic subneighborhoods. This gives two sets of features.

Using the same anisotropic data as Example 4.1 we compare the horizontal and vertical entropy and trace with their isotropic counterparts. These are plotted in

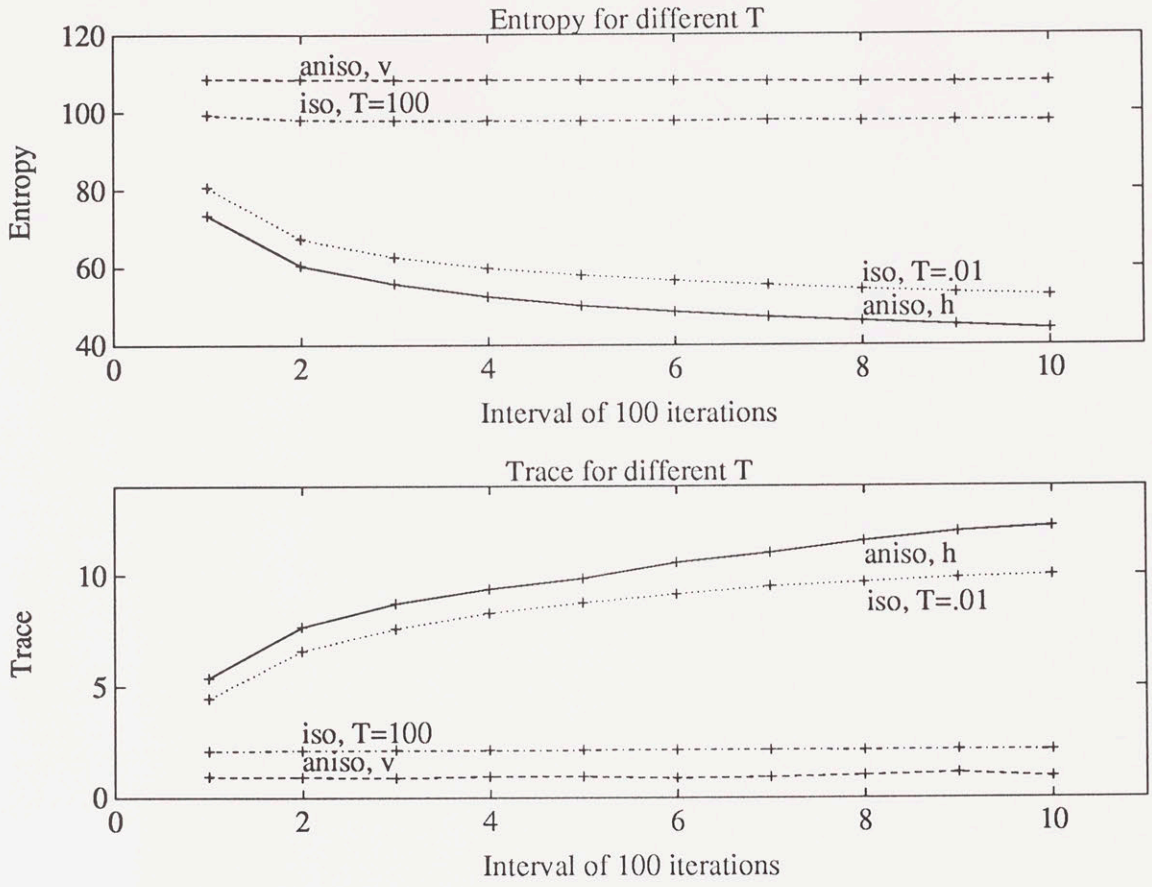

Figure 4-12: Comparison of aura matrix features between isotropic cases $T = 100$, $T = .01$ and the anisotropic case simulating $T = .01$ in the horizontal direction and $T = 100$ in the vertical direction. The simulataneous presence of the two temperatures allows the horizontal component to progress further than its isotropic equivalent.

Figure 4-12. The vertical component has the highest entropy and the horizontal has the lowest, with the two isotropic components falling in between. It is as if the horizontal direction (colder temperature, faster rate) took advantage of the vertical direction (higher temperature, slower rate) in their interaction; the horizontal achieves lower entropy at the expense of the vertical. Indeed, the sum of the two anisotropic components is very close to the sum of the two isotropic components, suggesting that the average entropy is conserved.

The trace behavior is shown below the entropy plot; again its behavior mirrors that of the entropy. The anisotropic vertical component climbs fastest; the anisotropic horizontal component climbs slowest. For both the trace and entropy the horizontal

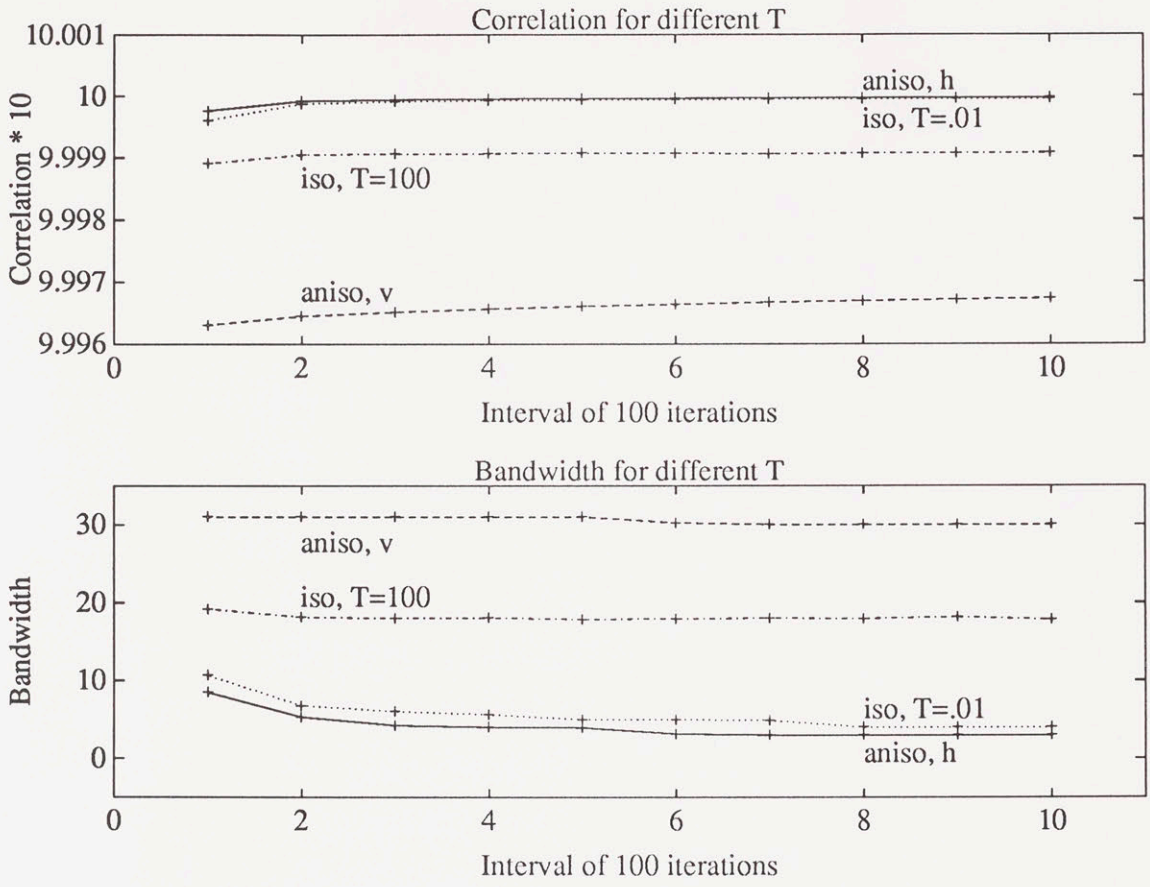

Figure 4-13: Comparison of aura matrix features between isotropic cases $T = 100$, $T = .01$ and the anisotropic case simulating $T = .01$ in the horizontal direction and $T = 100$ in the vertical direction. The simulataneous presence of the two temperatures allows the faster horizontal one to progress slightly further than it does in the isotropic case. The vertical component is, however, impeded.

---

component is less level than the corresponding isotropic component. This indicates that the anisotropic component is probably further from equilibrium.

In Figure 4-10 the correlation feature of the aura matrix is shown. This is nearly 1 for both isotropic and anisotropic cases but the ordering is still apparent with the anisotropic vertical component being the least correlated. The vertical component is also the steepest – indicating it is probably the furthest from equilibrium.

Below the correlation is the bandwidth of the aura matrix. Like the entropy the horizontal component has decreased the greatest, at some sacrifice of the vertical component. Here, however, there is not the conservation that was present with the

entropy – the sacrifice of 10 diagonals by the high temperature direction is much greater than the gain of about 1 diagonal by the low temperature direction.

All of the measures shown, energy, entropy, trace, correlation, and bandwidth exhibit similar regions of flatness which indicate equilibrium. The anisotropic example indicates that this equilibrium can be upset by the interaction of directional components at different rates.

Anisotropic non-minimum energy pattern formation

If the ground states of the textures in Figure 4-11 are analyzed using the results in Chapter 6, it is found that the ground states are all the same. The pattern formation in the anisotropic case arises solely from the different rates of convergence in the different directions. This is a significant example of the new interpretation of pattern formation with bonding parameters as annealing rates.

4.4.4 Long term behavior: average energy

Once a pattern is in equilibrium at a given temperature its average energy should be constant. In this section we study this relationship between energy and temperature. The importance of this study is to see if temperature of a system can be determined from its energy.

The mean energy was measured during long term synthesis of isotropic MRF's. We allowed 10,000 iterations for the system to enter equilibrium, then measured the mean energy over the next 40,000 iterations. The mean energy was normalized by $(n-1)^2$ so that the high temperature values would align for all graylevels. The normalized mean energy is plotted for $T \in \{0.01, 0.1, 0.27, 0.57, 1, 2.7, 10, 100, 1000, 10000\}$ and for $n \in \{2, 4, 8, 16, 32\}$ in Figure 4-14.

To estimate the temperature of a given texture one could compute its number of graylevels, lattice and neighborhood sizes, normalize, and then index into the energy vs. temperature curves. Consider the energy for $n = 2$. Around the values $T = 0.27, 0.57, 1, 2.7$ the plot is monotonic so temperature estimation can occur.

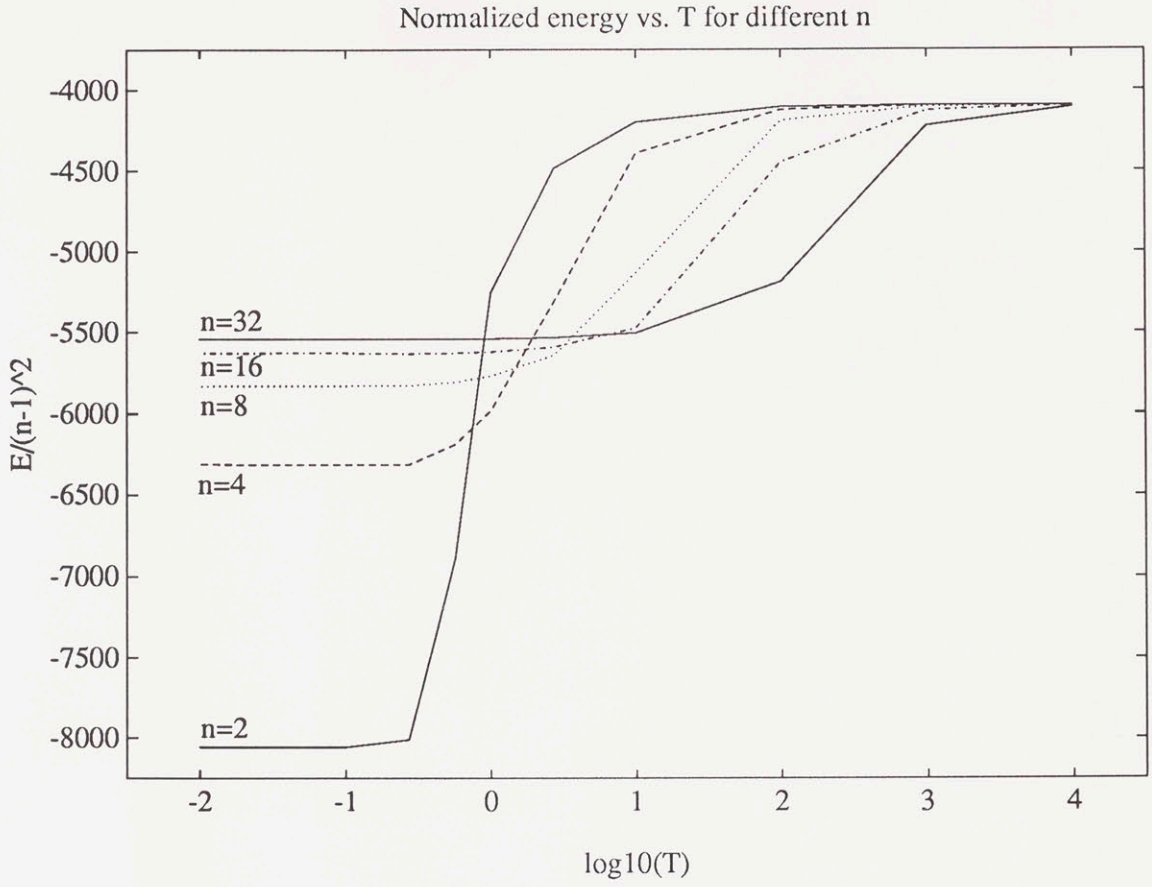

Figure 4-14: Normalized mean energy at each temperature for five different graylevels.

However, for temperatures at the ends of this range, the energy is constant. A similar range is visible for other values of n. Thus, we would expect energy based estimation to work well around the transition region, but not at the plateaus on each end.

4.4.5 Long term behavior: aura matrix features

The basic trends for these features were established in Section 4.4.2. Here we examine their long term behavior with regard to both temperature and graylevel. The goal is to find behavior that could be used to identify temperature and also to understand the way the textural features are influenced by temperature.

The simulations done here parallel those in the previous section. MRF's were synthesized at constant temperature and constant graylevel for $i = 50,000$ iterations. The aura matrix was computed once every 100 iterations. The entropy, trace,

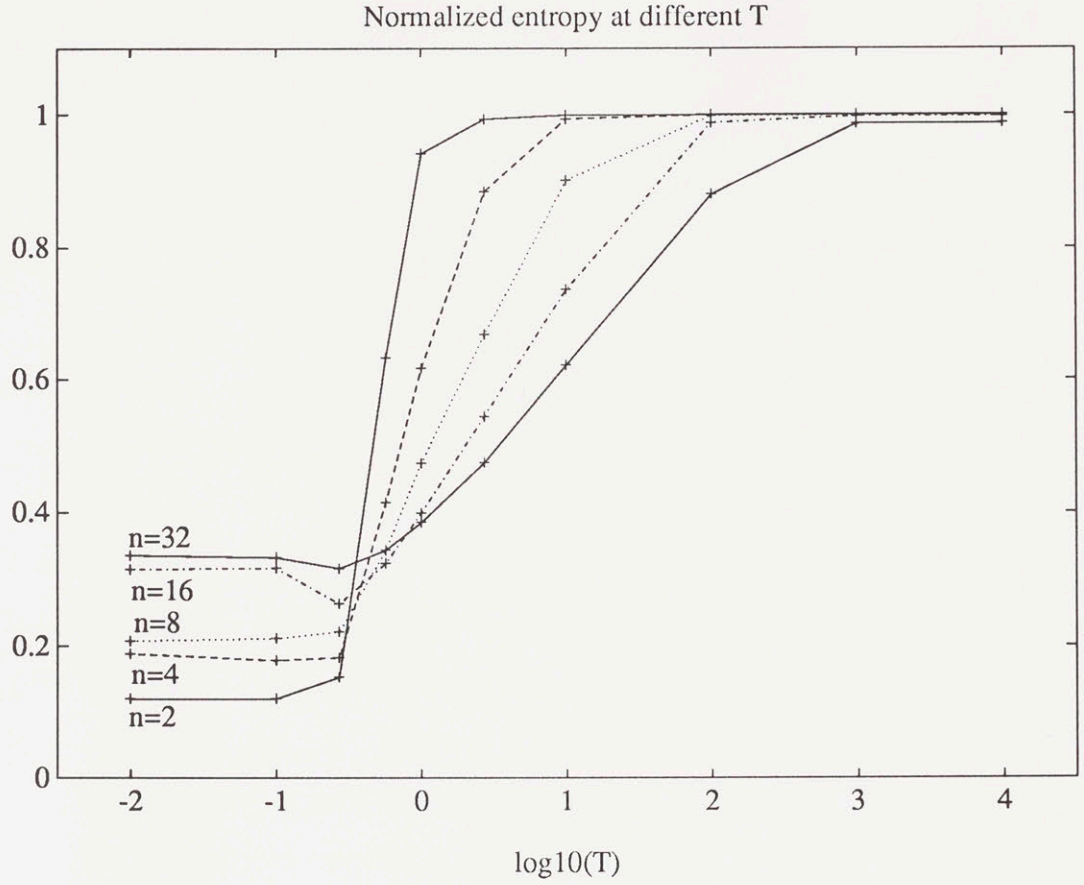

Figure 4-15: The normalized entropy shows a transition from high to low for each graylevel. The transition is slower for higher numbers of graylevels.

---

correlation, and bandwidth of the normalized aura matrices were computed for each graylevel and temperature. Each point plotted in this section is an average over many samples to give a good indication of typical behavior.

Entropy

The entropy for each aura matrix is normalized by $n \log n$ so that its maximum value is 1. Typical values of these are plotted in Figure 4-15. Starting at high temperature on the right it can be seen that each plot begins its descent near $T = (n-1)^2$, the energy normalizing factor. At around $T \leq 0.27$ the entropy ceases descending. The transition happens over a smaller range of T for smaller n.

We caution that flat plots with temperature as the abscissa do not imply equilib-

rium as did plots over an interval of iterations. For example, the flat low temperature region for the entropy of both $n = 16$ and $n = 32$ could get still lower over more iterations. Though not shown here, neither of these high graylevel, low temperature combinations is at equilibrium even after the 50,000 iterations.

Trace

As mentioned the traces are 1 at high temperature. In Chapter 6 we derive their ground state value which is slightly less than n; this corresponds to the value they should reach at $T = 0$ equilibrium. Typical examples of the trace behavior for different temperature are shown in Figure 4-16. As with the entropy the trace exhibits a transition from one plateau to the next.

Notice that cases $n = 2, 4, 8$ are near their optimal value at low temperature, but cases $n = 16, 32$ are not yet. There is also a little bump in $n = 16$ at $T = 0.27$. This is not an artifact; it shows up for different seeds. Rather, the values at lower temperature $T = 0.1, 0.01$ are not as high as they will be when the process reaches equilibrium. As described earlier, these support the hypothesis that $n = 16$ and $n = 32$ are not in equilibrium even at 50,000 iterations.

In Section 3.3 we mentioned that Cross [16] obtained a relationship between the co-occurrence statistics and the bonding parameters over a certain range. Letting $T = 1/\beta$ for the isotropic MRF, the results he obtained are a subset of those in our plot of the trace for $n = 2$. We plotted his results vs. ours in the range $\log_{10}(T) = 1, \ldots, 4$ and found excellent agreement.

Correlation

The long term correlation averages tend to be high at all temperatures for $n > 2$. Examples of these are shown in Figure 4-17. A transition is apparent, especially at $n = 2$. For low graylevels it can also be seen that the low temperature at which the correlation plateaus is the same at which the entropy plateaus.

Correlation has been the subject of much study for these models. Flinn [23] found

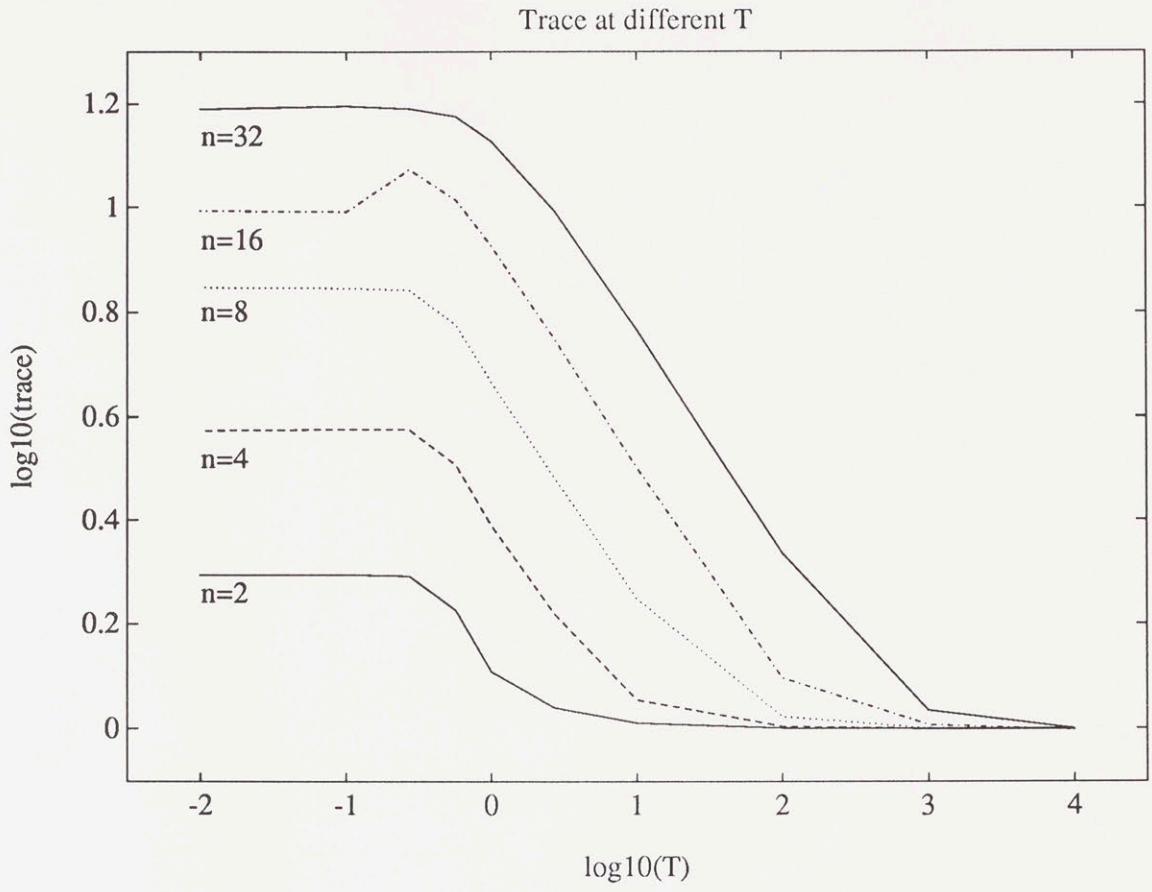

Figure 4-16: The normalized aura matrices are uniform at high T, with trace equal to 1. The traces show a smooth transition over temperature.

---

that the nearest neighbor correlation function is proportional to the energy change in the system for the Ising equiatomic (uniform histogram) model. The plot here for $n = 2$ is indeed inversely proportional to the $n = 2$ energy plot in Figure 4-14, supporting his findings. We remark that the inverse relation is not the same for the other graylevels.

Bandwidth

The bandwidths share a similar transition region with the other features with the notable exception of $n = 2$ which cannot decrease its bandwidth. Typical examples of bandwidth sharpening are shown in Figure 4-18. Notice that $n = 2, 4, 8$ reach the minimum possible bandwidth, 1. In support of the non-equilibrium hypothesis, the cases $n = 16$ and $n = 32$ have not yet attained this bound.

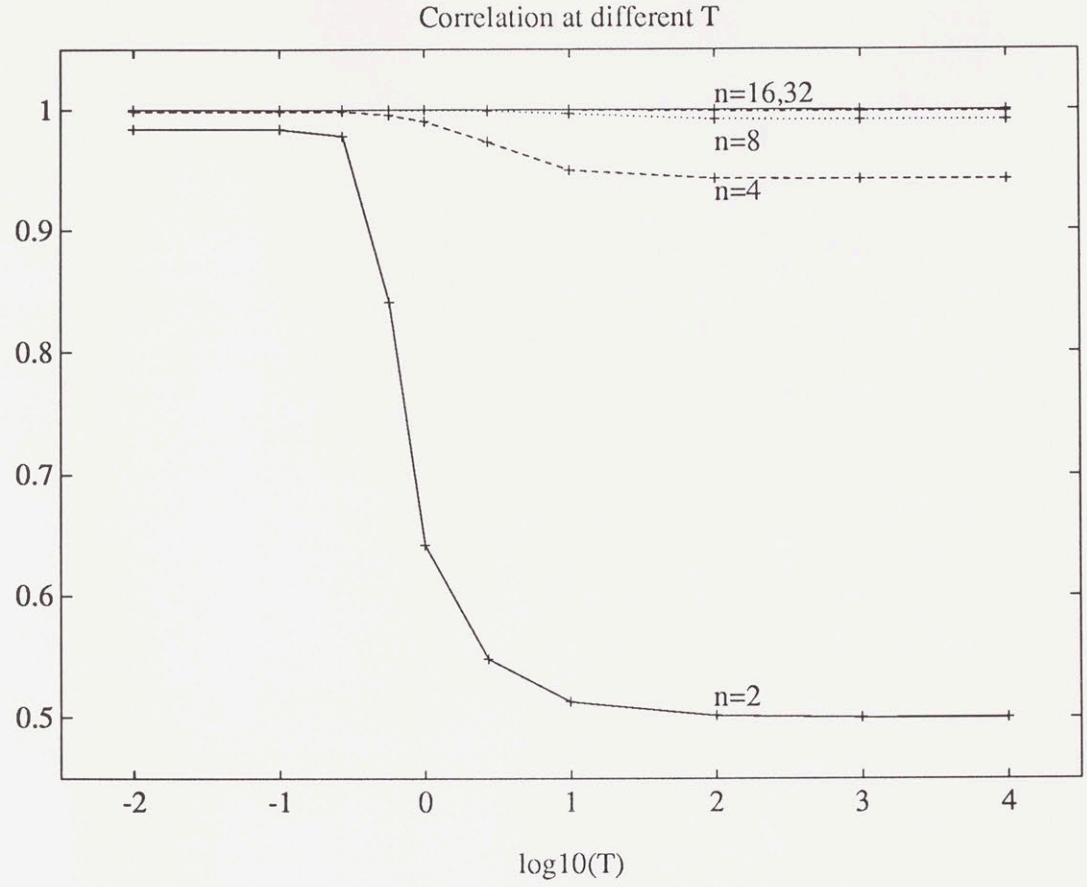

Figure 4-17: The average correlation exhibits a strong transition for the binary case, and much smaller transitions for higher numbers of graylevels.

In Chapter 6 we will show analytically that the aura matrix is trying to diagonalize for the attractive field. This analysis will explain the tendency for the bandwidth and entropy to decrease, and for the correlation and trace to increase. We will also show analytically that the matrix tends to become anti-diagonal for the repulsive field. The features for the repulsive field respond accordingly.

4.5 Periodic patterns with temperature variations

Since states with structure exist within the possible sample space of the MRF it is desirable to find a way to make them appear. We will show that by partitioning the plane and by using various kinds of temperature scaling, that a variety of periodic and near-periodic textures can be created.

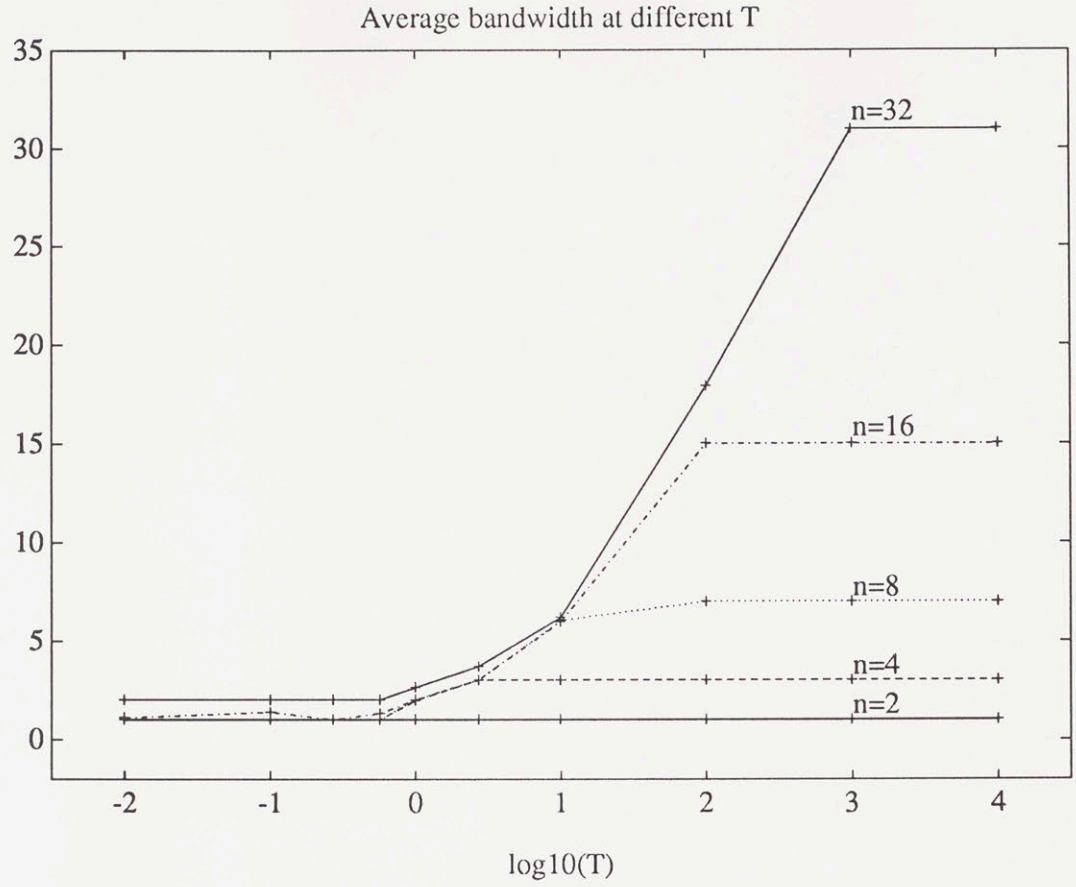

Figure 4-18: The bandwidths descend from n at high temperature to 1 at low temperature.

Suppose one wanted to synthesize a periodic texture. The obvious way would be to tesselate the plane with the texture primitives. In practice this gives a texture that looks too perfect to be natural. Nonlinear warping can help modify the periodicity, but it is a costly alternative and does not mitigate the artificial boundaries imposed by the tesselation.

The MRF gives an elegant solution to both these problems. Since the MRF is formulated on a toroidal lattice (the top of the grid is assumed connected to the bottom; the sides to each other), there are no artificial boundaries induced by tesselating with Gibbs samples. With annealing or other temperature scaling, the samples can be taken at slightly different temperatures, or sometimes even at the same temperature, so that they are not perfect replicas of each other. Note that sampling at different temperatures can give a greater variety of effects than just taking different stochastic

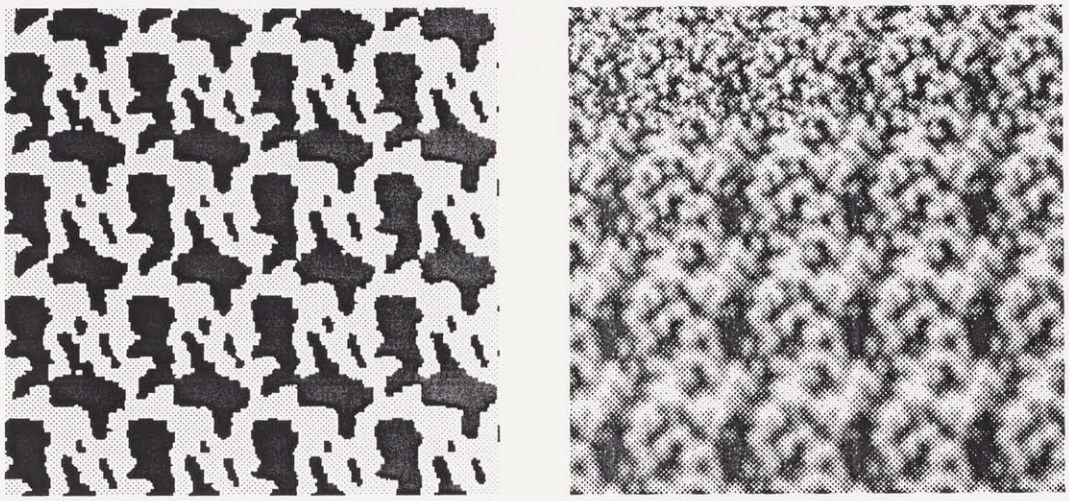

Figure 4-19: These two patterns were made by replicating a 4×4 array of 64×64 samples of Gibbs distributions. They illustrate the use of temperature to create a natural-looking, i.e., not perfectly periodic texture.

---

samples of the same state. One can think of temperature as a sort of "control knob" for changing the pattern smoothly.

In Figure 4-19 are shown two examples of textures formed by replicating Gibbs samples with annealing and temperature scaling. The effect is more natural than perfect replication of a texture primitive. In addition the texture patterning can be controlled so as to duplicate many interesting effects. For instance, by introducing a temperature gradient from top to bottom (as was done in the right-hand image of Figure 4-19) one can produce a perspective type of scaling.

Note that although the examples in Figure 4-19 are synthesized with replication, it is possible to have the random field produce the periodicity by partitioning it into independent regions prior to running the Monte Carlo synthesis. Each region is then its own "closed" system synthesizing its own random field. One can also conceive of hierarchies of such closed systems, building up increasingly complex textures. Given the same initial configurations in each region, the patterns of Figure 4-19 could be achieved using this partitioning idea.

Chapter 5

Transition temperatures

5.1 Introduction

Important changes in physical systems are characterized by their critical temperatures. For example, in purified mercury the critical temperature marks where the metal has zero resistivity and becomes superconducting. Critical points also mark the temperatures where ice becomes water and where water becomes steam, i.e., the points of *phase transition.*

In crystallization the freezing point is the critical temperature at which the solution crystallizes into a solid. This point marks where a random arrangement of particles becomes structured – an especially interesting transition to emulate with a random field texture model.

In statistical mechanics the critical points are defined to be the singularities of Z, the partition function. When Z is known, the critical temperature(s) can be found analytically. To date, Z is only known for the binary Ising model with zero external field. For this case there is one critical temperature, $T_c = 2.27$, and it corresponds to the maximum value of the temperature at which the center of the lattice is affected by the boundary conditions [36].

In general Z is unknown and its singularities cannot be determined. Also, one dimension of the lattice needs to go to infinity for a phase transition to exist. Thus, the finite textures modeled here do not have a critical temperature. Nevertheless, the

patterns still exhibit abrupt changes in behavior that mimic that of a phase transition. We call the temperature where the behavior changes a *transition temperature* and denote it by T_*.

Several people have suggested the importance of exploring phase transition phenomena for the Markov/Gibbs random field (MRF) in image processing[38, 20]. The critical point for the repulsive case of the Ising model with a small positive external field was examined empirically by Carnevali *et. al.* [8]. A similar phenomenological method was used by Van Den Bout and Miller [65], where they also showed that most of the optimization for their graph partitioning problem occurred around the critical temperature.

However, the methods used in these two cases and elsewhere in physics depend on changes in magnetism or spin averages, i.e., first order statistics. When an image histogram is constrained, then these first-order methods will not work. In contrast, critical phenomena for the Ising model was studied by Pickard [53] using correlation. We will form a new second-order statistics approach based on the aura matrix.

In Section 5.2 we develop and analyze new empirical methods of identifying transition temperatures for an isotropic texture. The idea of transition temperature is used to explain problems with the previously used texture convergence criteria in Section 5.3. Section 5.4 briefly discusses some ways that the knowledge of the transition temperature can be used to synthesize non-minimum energy textures. Section 5.5 addresses the isotropic estimation problem and summarizes some of our temperature characterization results.

5.2 Transition temperature

The problem of locating the transition temperature T_* for an isotropic field is examined in this section. As mentioned, this problem cannot be solved analytically since the partition function is unknown. It is also difficult to solve by simulation since there are an infinite number of possible parameter combinations to explore. We restrict our attention to a first order isotropic auto-binomial MRF, with $\beta = 1$, and

to the consideration of the Gibbs energy and miscibility matrix properties. Some of the following results for the binary case also appeared in [52].

5.2.1 Specific heat

In physics, the *specific heat* measures the change of energy with respect to temperature at a given volume or pressure. In simulated annealing this quantity has been approximated and found to have a large value when the state of order of the system was changing. Kirkpatrick *et. al.* [37] interpreted this point as the place where freezing begins and where the process should be cooled the slowest. At a genuine critical temperature, the specific heat would be infinite. For our finite textures, the peaks of the specific heat should correspond to transition temperatures. We explain the formulation of this quantity for textures, and show simulations of its computation.

Formulation

The specific heat is formulated as follows. In statistical mechanics the average energy is

$$< E(T) > = \frac{-d \ln Z}{d(1/k_{\mathbf{B}}T)}.$$

The rate of change of the energy with respect to temperature gives the size of typical fluctuations in the energy at a given T [37],

$$\frac{d < E(T) >}{dT} = \frac{< E(T)^2 > - < E(T) >^2}{k_{\mathbf{B}}T^2}.$$

This quantity is used in physics to measure the specific heat. For texture measurements we normalize by the lattice size and omit the Boltzmann constant, obtaining

$$C(T) = \frac{(< E(T)^2 > - < E(T) >^2)}{T^2|\mathcal{S}|},$$

the specific heat for an MRF sample. Since the synthesis algorithm samples with the Boltzmann factor, $\exp(-E/T)$, the evaluation of the mean of the energy at T,

$< E(T) >$, is just the sum

$$< E(T) > = \frac{\sum_{i=1}^{i_{eq}} E_i(T)}{i_{eq}},$$

where $E_i(T)$ is the Gibbs energy at the current temperature and iteration, and i_{eq} is the number of iterations performed at each temperature during annealing.

Equilibrium at a given temperature

We compared the effects of varying i_{eq} on measures of the specific heat and found that its peak characteristics changed, but its peak position was relatively constant.

In Figure 5-1 typical plots of the specific heat are shown for $i_{eq} = 10, 20, 50, 1000$ and $n = 2$ for a first order isotropic auto-binomial MRF with $\beta = 1$. The total number of iterations for each plot is $1000 i_{eq}$, with log annealing at rate constant $c = 2.7$. At the right, the initial value of temperature is very high. The values are denser at the lower temperatures due to the log annealing which effectively spends more time at lower temperatures.

The value of T corresponding to the peak in each plot was measured and the average of these four values was found to equal $\log_{10}(T_*) = -0.245$, or $T_* = 0.569$. The primary effect of the larger i_{eq} is a raising of the specific heat around the peak; however, it does not appear to affect the position of the peak.

For the different i_{eq} in this example the resulting texture patterns were not noticeably affected. Representative texture examples for the case $i_{eq} = 10$ are shown in Figure 5-2. Each sample corresponds to $i = 10$, 100, 1000, 10000, iterations and $\log_{10}(T) = 0.59$, 0.054, -0.23, -0.40, respectively. A quick glance reveals that above T_* the pattern does not develop much, whereas below T_* a definite separation of black and white has occurred. A possible physical analogy to this behavior is that the system is a gas at high temperature and a solid at low temperature.

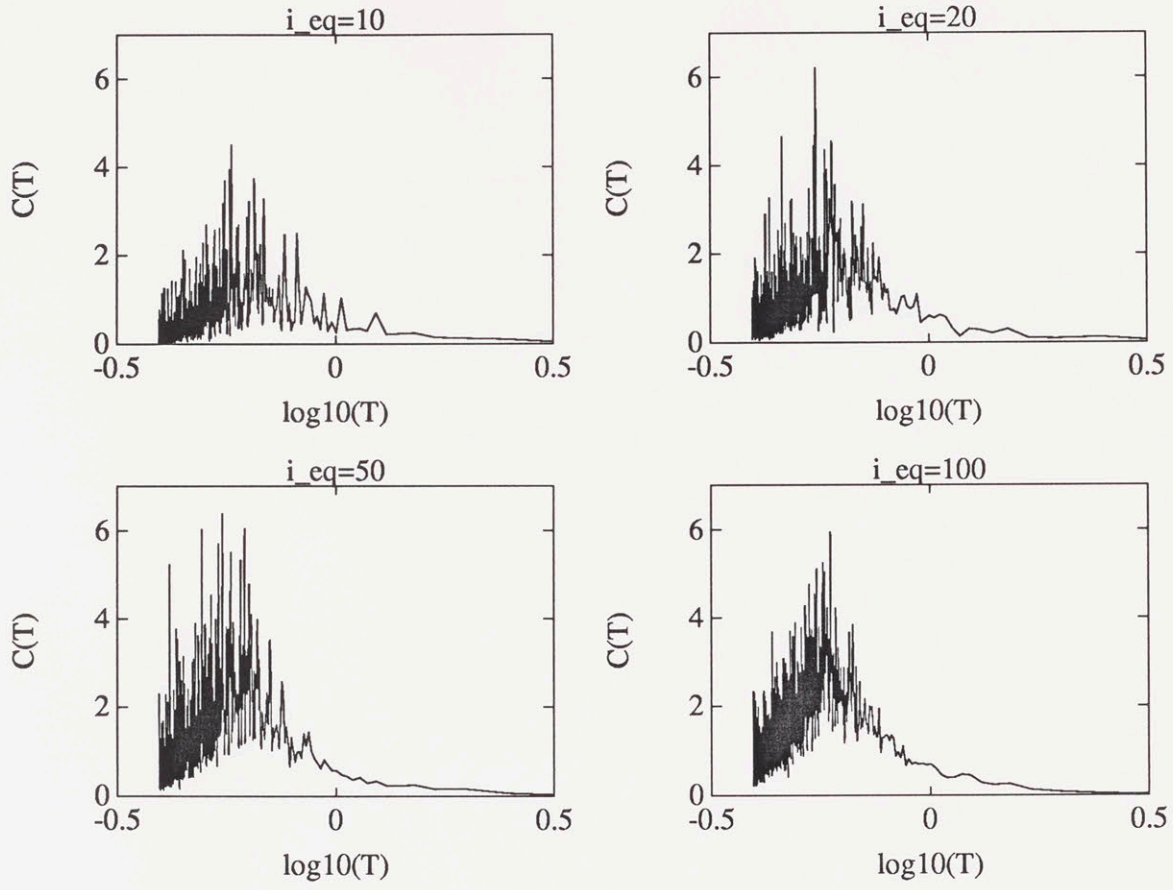

Figure 5-1: Specific heat for the binary isotropic auto-binomial model with $\beta = 1$ for different equilibrating lengths, $i_{eq} = 10, 20, 50, 100$.

Comparison between T_c and T_*

As mentioned before, the critical temperature for the binary Ising model, T_c is known. We now show a simple equivalence mapping between the binary auto-binomial MRF and the Ising model which allows comparison between the the theoretical value T_c and the empirical value T_* determined by the specific heat.

We start with the auto-binomial joint probability with zero external field and $\beta = 1$,

$$\frac{1}{Z} \exp\left(\frac{1}{T} \sum_{s \in \mathcal{S}} \sum_{r \in \mathcal{N}_s} x_s x_r\right).$$

Substituting the mapping $x_s = (\sigma_s + 1)/2$ gives the probability in terms of the Ising

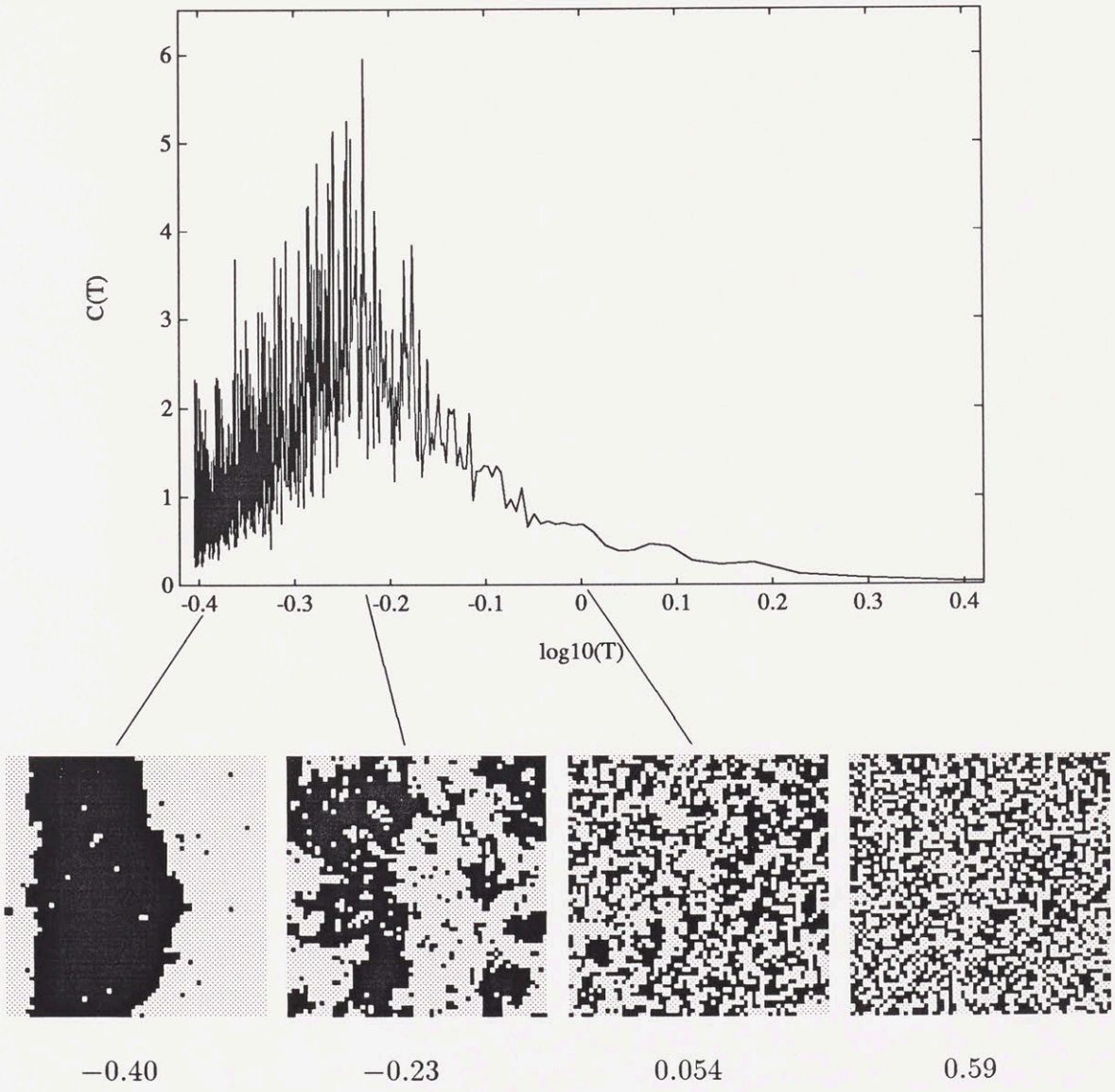

Figure 5-2: Isotropic samples and their corresponding log temperatures. The specific heat is shown for comparison of patterns relative to peak position. Each image is 64×64.

variables, $\sigma_s, \sigma_r \in \{-1, 1\}$,

$$\frac{1}{Z} \exp\left(\frac{1}{4T} \sum_{s \in \mathcal{S}} \sum_{r \in \mathcal{N}_s} (\sigma_s + 1)(\sigma_r + 1)\right).$$

All terms in the energy which are single site or constant terms contribute to the external field or normalization and can be ignored. The remaining terms yield

$$\frac{1}{Z} \exp\left(\frac{1}{T_I} \sum_{s \in \mathcal{S}} \sum_{r \in \mathcal{N}_s} \sigma_s \sigma_r\right),$$

where $\frac{1}{T_I} = \frac{1}{4T}$. When $\mathcal{N}_s$ is the four nearest neighbors, this is the Ising model (cf. (2.5)). Let T_* be the transition temperature of the auto-binomial model. At the critical temperature for the Ising model, $T_I = T_c$, we desire

$$\frac{1}{T_c} = \frac{1}{4T_*}.$$

The critical temperature for the 2-D Ising model with zero external field was solved by Onsager [48] and is the solution to $\sinh(2/T_c) = 1$. Solving this and substituting in the above gives

$$T_* = \frac{T_c}{4} = \frac{1}{2\ln(1 + \sqrt{2})} = 0.567.$$

The theoretical value is very close to the peak found empirically at $T = 0.569$.

For higher numbers of graylevels the critical temperature is not known. In Chapter 4, however, transition behavior was seen in aura matrix features for all n. Let us now examine some ways of locating transition points for higher n.

5.2.2 Multiple transitions and specific heat

The specific heat was very successful in locating the transition temperature for $n = 2$. However, we found three basic problems with using the specific heat when $n > 2$.

First, we found that the peaking behavior of the specific heat depends on c, the annealing rate. When c is "low," e.g., if $c = 2.7$ and $n > 2$, then the pattern

will change rapidly in the beginning and the specific heat will be dominated by a huge initial peak at high temperature, followed by noisy behavior as it cools. We determined that if $c \geq (n-1)^2$ for a pattern of graylevel n, then the specific heat will have behavior more similar to that of the binary case, i.e., it will start small, and be peaked when $T = 0.569$. However, the peak is not sharp as it was for $n = 2$, but rather broad and noisy, with breadth increasing with n.

Once the annealing rate is appropriately chosen, the second problem is to reach equilibrium at that rate. The higher c, the slower the annealing rate. A typical example of this is shown in Figure 5-3 for an $n = 8$ texture. In this example annealing was run with $i_{eq} = 100$, and the specific heat was plotted. After 100,000 iterations of annealing the specific heat has only been measured down to $T = 7.1$, midway in the transition region. To lower to $T = 0.5$ at this annealing rate would take on the order of e^{98} iterations!

Of course there are alternatives, such as to sample the temperature less often. However, with the specific heat method, less samples increases the likelihood of missing the peaks – a third problem with this method.

For $n > 2$ we have found that the specific heat is generally high throughout the temperatures where the bandwidth changes. The first three bandwidth transitions for the $n = 8$ example are shown above the specific heat in Figure 5-3. We looked for peaks in the specific heat corresponding to these transitions for many n and c and only found them sporadically.

Because it takes so long to study patterns when annealing is used, we chose instead to synthesize for long times at constant temperature over a variety of temperatures, $T \in \{0.1, 0.27, 0.57, 1, 2.7, 10, 100, 1000, 10000\}$. We formed averages of the specific heats over 50,000 iterations of constant temperature synthesis for a wide variety of graylevels and temperatures. Typical plots of these are shown in Figure 5-4.

The specific heats, $C(T)$ shown here are all normalized by $(n-1)^4$ and plotted on a log-log scale for closer comparison. At high temperature the specific heat is minimum. For $n = 2, 4$ the energy variance is actually zero and $\log_{10} C(T)$ is not

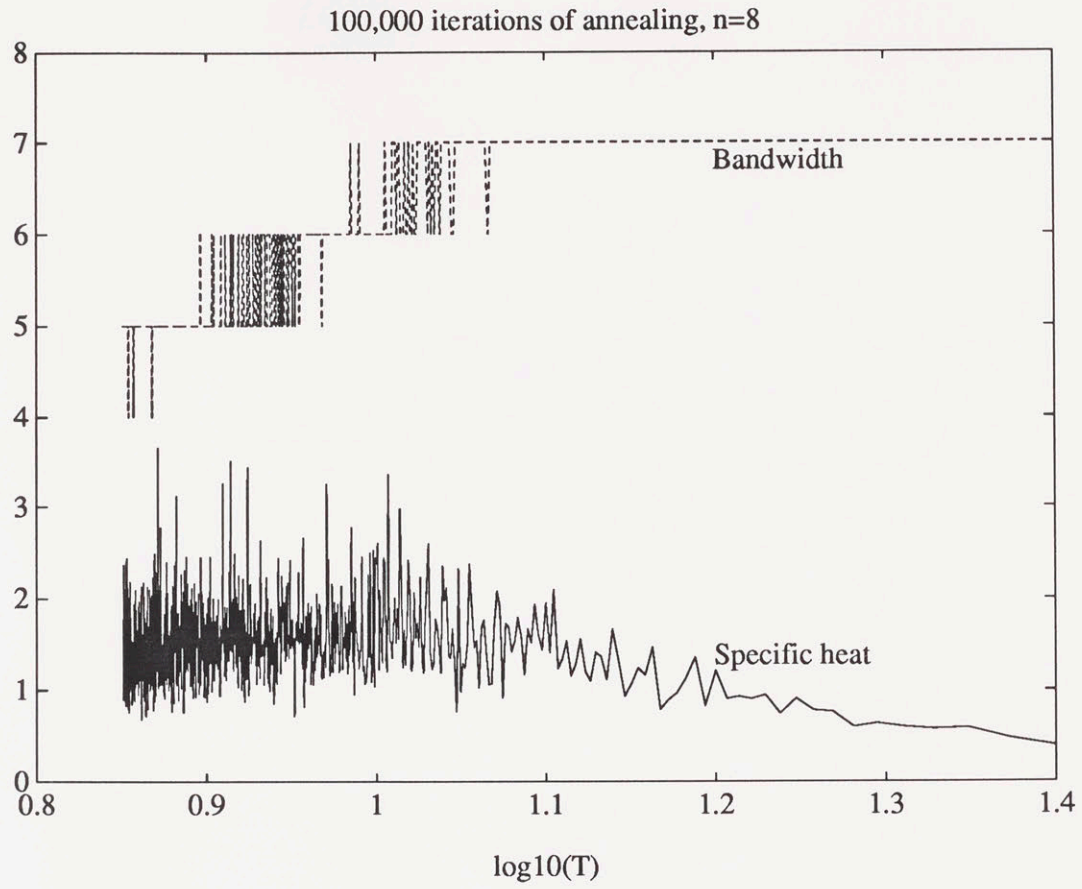

Figure 5-3: For $n > 2$ the specific heat shows high values throughout the temperature range where the bandwidth changes. This is in contrast to $n = 2$ where one peak is evident and the bandwidth is constant.

---

shown. Observe that for $n < 32$ the increase in $C(T)$ is linear from the minimum at the right to the first peak moving left. This behavior on the log-log plot is self-similar; we will comment further on this below. On the far left at cold temperature $C(T)$ drops. For $n = 16$ and $n = 32$ it is still high. Since equilibrium time grows with $(n-1)/T$, it is reasonable to expect that these points are not in equilibrium yet.

Notice that there is a strong sharp peak at $\log_{10}(T) = -0.245$ for $n = 2$, (one of the temperatures at which the features were sampled). This is consistent with the earlier results obtained by annealing. We also point out that this temperature is the "leftmost" point of the peaked region for *all* the plots.

Consistent with the choice of $c \geq (n-1)^2$, we found empirically that the rightmost

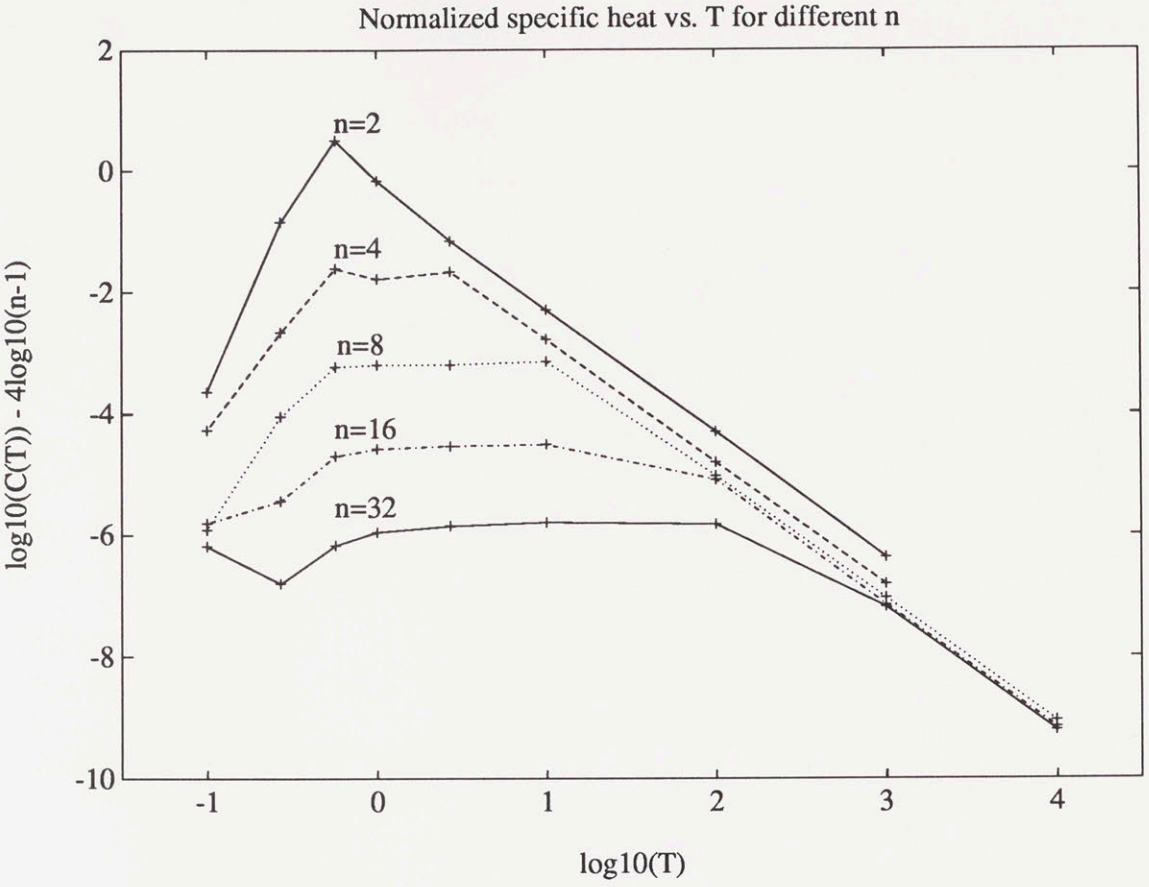

Figure 5-4: Normalized log of specific heat at each temperature for five different graylevels.

---

point of the peaked region always occurred at

$$T \leq \frac{T_c(n-1)^2}{4},$$

where T_c is the critical point for the Ising model. This behavior is also consistent with the high temperature normalization developed in Section 4.4.1.

This ratio also accounts for the behavior we have seen where the transitions occur at higher temperature for larger n. The changing of a critical point by adding something (like more graylevels) to a solution is not new. The addition of salt to ice is a commonly occurring example in New England – the resulting mixture lowers the freezing point.

Observe that for $n = 4$ the plateau looks like it might actually be comprised of

two peaks. In the next section we will offer more support for this observation.

Self similarity over temperature

Linearity on a log-log scale is a sign of self-similarity and indicates that the pattern is fractal over the linear range. This range is $T \in \{0.57, 1, 2.7, 10, 100, 1000\}$ for $n = 2$. The fractal dimension is determined by the slope of this line, -2.115, indicating that the relationship over this range between temperature, T and specific heat, $C(T)$, is well approximated by

$$\frac{C(T)}{(n-1)^4} = .943 \left(\frac{1}{T}\right)^{2.115}.$$

Self-similar behavior appears to be a feature for all the graylevels, with the linear region gradually shifting right with increasing n.

5.2.3 Multiple transitions and bandwidth

For $n > 2$ the bandwidth of the aura matrix decreases as was shown in Figure 4-18. We have found that the specific heat is high during the entire region where the bandwidth is decreasing. This suggests that the temperatures at the bandwidth discontinuities might also be transition temperatures.

There is a physical pattern-motivated reason that also supports this suggestion. At the bandwidth discontinuities the textures undergo a sharp change in their miscibility properties. For example, at the first transition the color white stops mixing with black. (If the lattice were permitted to break, total separation could also happen when $n = 2$.) For a texture of n graylevels there are $n - 1$ bandwidth drops, and thus $n - 1$ ways in which a color can "drop out" of the mixing.

This behavior is analogous to the crystallization analogy of Chapter 1 where temperature was used to control solubility. When the temperature was lowered below a certain point one component of the mixture precipitated out.

If the lattice were allowed to break it would break at exactly these bandwidth discontinuities. Consider the new matrix formed by looking at just the miscibilities

for the black and white elements when $n > 2$,

$$\begin{bmatrix} m(0,0) & m(0,n-1) \\ m(0,n-1) & m(n-1,n-1) \end{bmatrix}.$$

When $m(0,n-1) \rightarrow 0$ then this matrix becomes irreducible, signaling a disconnected lattice.

The precipitating behavior is illustrated for $n = 6$ in Figure 5-5. It can be seen that at each bandwidth decrease a new graylevel ceases to mix with black. The mixing and separation behaviors for an n graylevel texture are thus grouped into $n-1$ regions.

Recall the plots of Figure 4-18 where the bandwidth at a given temperature and graylevel was plotted. From high temperature to low, substantial drops occur. In Figure 5-6 typical bandwidths are shown during annealing, a more gradual temperature change. For each n, a 64×64 sample was synthesized with $i_{eq} = 100$ and rate constant $c = (n-1)^2$ for 50,000 iterations. We found that this value was sufficiently large to allow all the bandwidth discontinuities to occur. All the bandwidths are normalized by their maximum, $n-1$.

The stairstep effect in this figure reflects diagonalization of the matrices. Consider the behavior for $n = 32$. The unnormalized bandwidth drops from 31 to 20 over the temperature range $2.2 < \log 10(T) < 3.2$ in 11 visible levels. Although the downward trend is clear, the bandwidth may fluctuate quite a bit at each temperature. For $n = 16$ there are 5 visible steps from bandwidth 15 down to 10. For $n = 8$ there are 2 visible steps from 7 to 5. For $n = 4$ the drop is from 3 to 2 in one step.

For $n = 4, 8$ the transition from one bandwidth to the next is sharp. That is, a given bandwidth corresponds to a given temperature region. This behavior is consistent and can thus be used for temperature estimation in these regions. The estimation also works for higher n, but the resolution decreases as each bandwidth corresponds to a larger range of temperature. In this case band separation is sacrificed. This poorer performance may also be due to the cases $n = 16, 32$ being slightly further

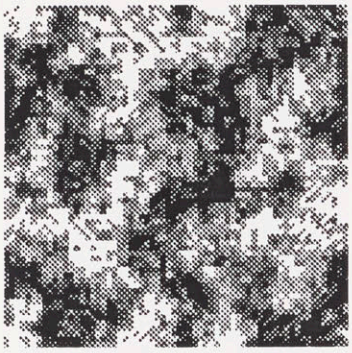

$$\mathbf{A} = \begin{bmatrix} 1454 & 859 & 345 & 60 & 10 & 0 \\ 859 & 908 & 685 & 229 & 42 & 5 \\ 345 & 685 & 848 & 596 & 201 & 53 \\ 60 & 229 & 596 & 870 & 632 & 341 \\ 10 & 42 & 201 & 632 & 974 & 869 \\ 0 & 5 & 53 & 341 & 869 & 1476 \end{bmatrix}$$

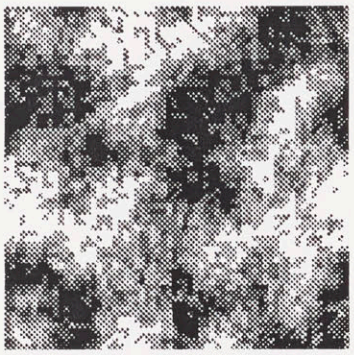

$$\mathbf{A} = \begin{bmatrix} 1714 & 839 & 160 & 15 & 0 & 0 \\ 839 & 1104 & 658 & 124 & 3 & 0 \\ 160 & 658 & 1128 & 661 & 116 & 5 \\ 15 & 124 & 661 & 1136 & 631 & 161 \\ 0 & 3 & 116 & 631 & 1104 & 874 \\ 0 & 0 & 5 & 161 & 874 & 1704 \end{bmatrix}$$

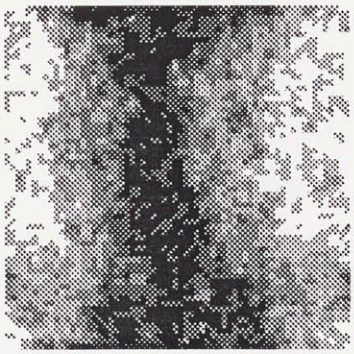

$$\mathbf{A} = \begin{bmatrix} 1868 & 822 & 37 & 1 & 0 & 0 \\ 822 & 1418 & 466 & 22 & 0 & 0 \\ 37 & 466 & 1550 & 649 & 25 & 1 \\ 1 & 22 & 649 & 1524 & 496 & 36 \\ 0 & 0 & 25 & 496 & 1440 & 767 \\ 0 & 0 & 1 & 36 & 767 & 1940 \end{bmatrix}$$

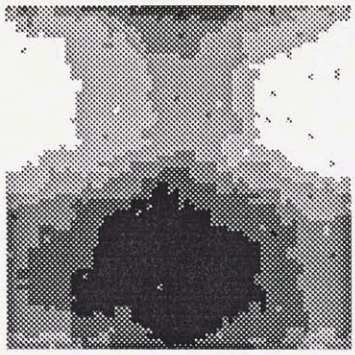

$$\mathbf{A} = \begin{bmatrix} 2546 & 182 & 0 & 0 & 0 & 0 \\ 182 & 2288 & 258 & 0 & 0 & 0 \\ 0 & 258 & 2248 & 222 & 0 & 0 \\ 0 & 0 & 222 & 2256 & 250 & 0 \\ 0 & 0 & 0 & 250 & 2292 & 186 \\ 0 & 0 & 0 & 0 & 186 & 2558 \end{bmatrix}$$

Figure 5-5: Patterns and aura matrices corresponding to a six graylevel MRF at transitions from bandwidth four down to bandwidth one. For example, bandwidth four with $m(0,5) = 0$ restricts black and white pixels from occuring in the same neighborhood.

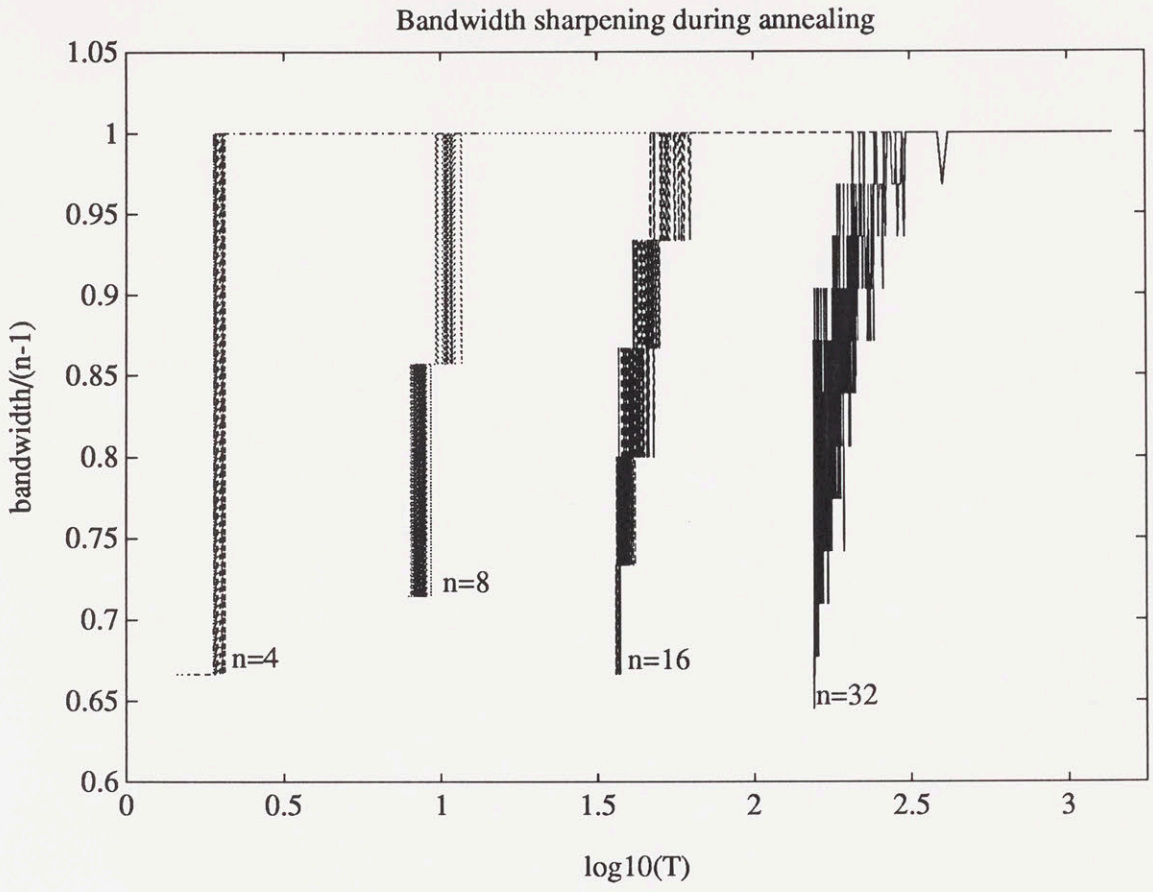

Figure 5-6: Bandwidths of aura matrices changing with temperature.

---

from equilibrium.

Bandwidth and annealing rates

In the last section, we mentioned that one problem with using peaks of the specific heat to determine transition temperature is that the peaks of $C(T)$ change with c, the annealing rate. For faster annealing rates (lower values of c) the bandwidth will plummet initially, skipping over intermediate levels.

A typical example of this behavior is illustrated in Figure 5-7 where $n = 4$ and aura bandwidths are shown for three different rates of log annealing for 100,000 iterations. The initial state for all three has aura bandwidth 3. The bottom curve is the specific heat from Figure 5-4. As mentioned before, the specific heat is peaked during the bandwidth transitions.

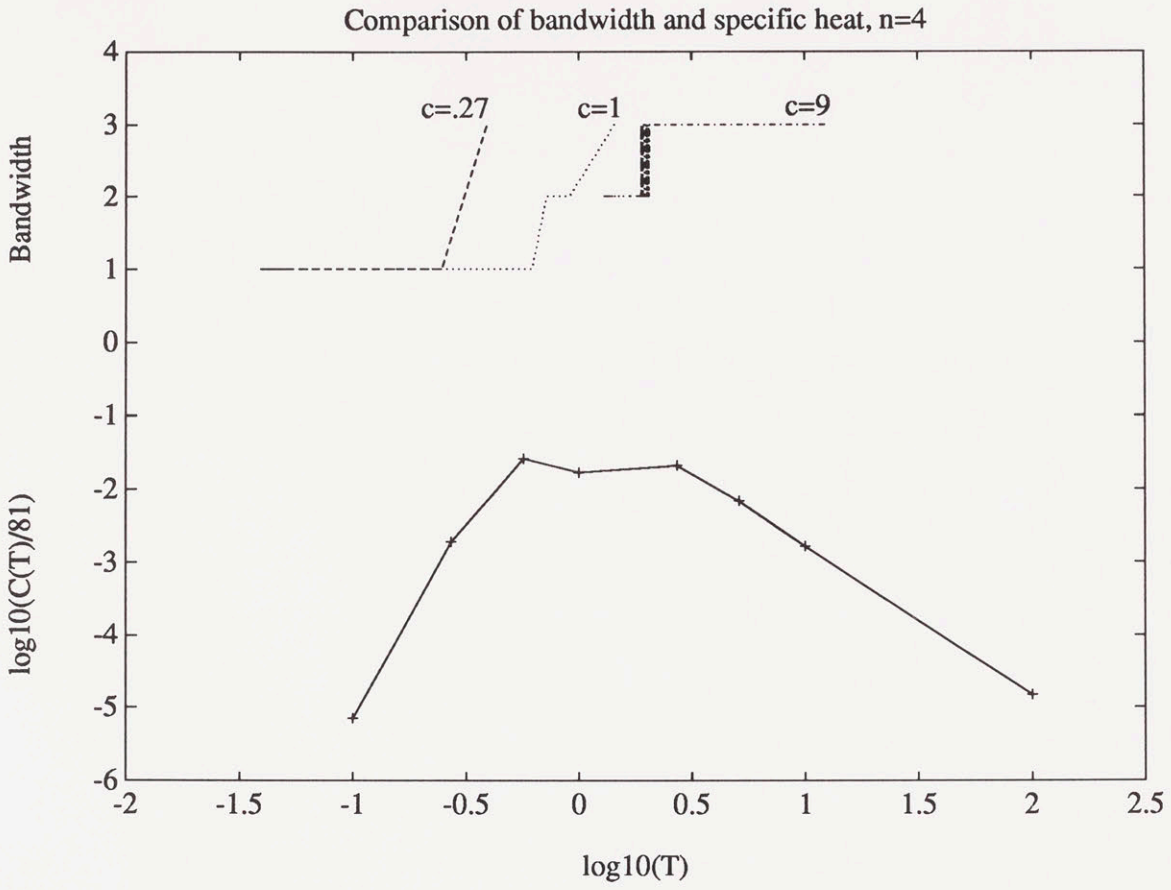

Figure 5-7: The top three curves correspond to the bandwidth of the aura matrix at three different annealing rates with log annealing for 100,000 iterations. The bottom curve is the specific heat from Figure 5-4. The bandwidth transitions occur during the peaked region of the specific heat. The fastest rate, $c = .27$, starts at a temperature just left of the peak in the specific heat; it does not stop at the intermediate bandwidths, 3 and 2. The slowest, $c = 9$ will stop at all intermediate bandwidths, but will take a long time to do so.

The fastest rate, $c = .27$, starts at a temperature just left of the peak in the specific heat; it does not pause at either of the intermediate bandwidths, 3 and 2, but drops on the first iteration to the minimum bandwidth of 1. The next fastest, $c = 1$, starts in the middle of the peaked region of the specific heat. It plunges on the first iteration to level 2, where it lingers before dropping to level 1. The slowest rate, $c = 9$, lingers at level 3, then at level 2, and would be expected to drop to level 1 if we would wait on the order of e^{15} more iterations until the annealing reached the temperature at the left side of the peak.

Although the bandwidth transitions do correspond to discontinuous changes in the pattern, and they do occur during the peaked region of the specific heat, we were not able to obtain sharp peaks at each drop to support that they correspond to "true" transition temperatures. Obtaining these sharp peaks in the specific heat is difficult because of the vast length of time involved. For texture modeling, what is more important is that we have bounded the region where the texture undergoes these $n-1$ abrupt changes. Although these bounds are empirical, they were found to be consistent over all samples examined.

Notice that Figure 5-7 also illustrates why the problem of estimating the "rates" is nonlinear. One could consider an estimate of the rate as the ratio of "bandwidth change" to "temperature change". Since all bandwidth changes take place within the bounded region of the specific heat peak, these rate estimates will saturate rapidly outside the peak region. For example, any "rate" slower than $c = 9$ will undergo changes virtually identical to the case shown for $c = 9$. Any rate faster than $c = .27$ will also drop the bandwidth from $n-1$ to 1 in one iteration.

5.3 Convergence criteria and temperature dependence

The number of iterations required for the texture pattern to "converge" has been a point of confusion in the literature. The confusion seems to be partly due to different definitions of convergence and equilibrium, and partly due to a lack of understanding of the nonlinear effect of temperature.

For texture synthesis it is intuitively satisfying to stop the Monte Carlo iterations when the pattern has stopped changing. There are two events which will cause this: First, if it gets "stuck" in a local minimum of the energy function. Second, if it reaches its $T = 0$ equilibrium state, or "ground state". The second event is the desired one in most applications; this event is typically considered to be the "converged" state, the state of minimum energy.

The concept of "equilibrium" is trickier. When annealing is done, the texture

is iterated i_{eq} times at the current temperature so that it will approximate a sample of the Gibbs distribution at that temperature. As mentioned in Section 4.4.1, equilibrium has also been associated with the energy level being constant.

In thermodynamics, a system is in equilibrium if no further changes occur in it when it is isolated [39]. At this point all its properties are homogeneous – there is no turbulence or pressure gradient; there is no diffusion, no reaction, no temperature gradient. The presence of any of these is the study of non-equilibrium states, often called "irreversible thermodynamics." We believe that these non-equilibrium states are a rich supply of texture patterns, and suggest their study in Chapter 8.

Intervals of sloping energy can be associated with non-equilibrium. Also, even when the texture is in equilibrium it will be constantly changing until it reaches its $T = 0$ equilibrium state. Thus, "equilibrium" implies "convergence" only at $T = 0$.

The texture studies in the literature have stopped the synthesis process after ten to twenty iterations claiming "convergence" has occurred. We caution that this convergence is different from the one described above. The literature studies [16, 17, 26], defined convergence as either of the two following criteria being met:

- The number of pixels which are swapping in the Metropolis algorithm is sufficiently small;
- The estimated parameters of the synthetic texture are close to the desired parameters.

The first criterion suffers from two problems: First, percent pixels swapping is temperature and graylevel dependent. Textures that are hotter than the transition temperature(s) will have a high number of pixels swapping and increasing the graylevel (like lowering the temperature) makes the percent swapping decrease faster. Second, if a texture gets "stuck" in a local minimum, the number of pixels swapping will satisfy the first criterion even though the MRF has not converged to its maximum probability configuration. A better pixel swapping criterion would be "the percent swapping is constant." This would correspond to an equilibrium condition.

The second criterion suffers from the problem that the bonding parameters do

not uniquely correspond to a given texture sample. We illustrated this in Section 4.2, and showed in (4.4) that each parameter β_k controls the rate of mixing or separation in a particular direction. Moreover, we have shown in this chapter that these rates are also affected by their position relative to the transition region. The maximum likelihood estimator described in Section 2.4.1 does not account for this nonlinear variation with temperature.

Some of the problems encountered in the parameter estimation of [26] can be explained with temperature. They noticed that their parameter estimates were low when $n > 2$. By scaling their Metropolis decision rule by an arbitrary factor of 0.5 their parameter estimates increased and were closer to the synthesizing parameters in the range of around 12 iterations. They suggested this problem might be due to the use of the different codings in the maximum likelihood estimator.

We investigated this problem by including temperature in the MRF model. We found that their ad hoc scale factor is equivalent to letting $c = 0.5$, i.e., synthesizing at a lower temperature than the "no temperature default", $c = 1$. Since decreasing the temperature has the same effect as increasing the parameter β, this explains why it raised the values of their estimated parameters.

The structure of the new aura matrix will give a better measure of convergence, at least if the ground state is the desired pattern. This structure is the focus of the next chapter.

5.4 Non-minimum energy texture synthesis

We have observed that qualitatively different textures correspond to temperatures above and below the region where the specific heat peaks. Using the bandwidth for $n > 2$, we have also shown that qualitatively different textures occur during the peaked region of the specific heat. The trend of the bandwidth to decrease to 1 with decreasing temperature has already been shown empirically and will be derived analytically in the next chapter. We will show in Section 6.3 that given a sufficiently large lattice, the texture pattern which minimizes the auto-binomial Gibbs energy

will have aura bandwidth 1.

Since textures of bandwidth 1 are very restrictive, one will want to be able to synthesize "non-minimum energy" patterns. At this point one may adjust the constraints of the problem, or possibly alter the energy function so that the new minimum is the desired texture. Alternatively, one can use the temperature characterization in this chapter.

The temperature characterization gives approximate bounds on the transition region. Consider again the plots in Figure 5-7. Suppose the desired pattern has aura matrix with bandwidth 2. By synthesizing at a temperature in the range $-.25 < \log_{10}(T) < 0.3$ corresponding to the right side of the peaked region, the long term "equilibrium" behavior of the synthesis should produce a pattern with the desired bandwidth. Synthesizing at higher temperature is more likely to produce patterns with full bandwidth, and synthesizing at lower constant temperature is more likely to produce patterns with bandwidth 1.

5.5 Temperature estimation

Parameter estimation is not the focus of this thesis, and yet by our new temperature characterizations some new progress has been made toward solving this problem. For the isotropic MRF, temperature estimation and bonding parameter estimation are equivalent problems. Bonding parameter estimation is known to be quite difficult; it is nonlinear and the many methods that exist have been noted to have serious shortcomings. We discuss briefly a few of the problems, summarizing some of the ways the temperature characterization is helpful.

First, we refer the reader back to Figure 4-14. From this plot of energies, it can be seen that at both low and high temperature, there exists a plateau where the temperature may change but the energy is constant. Moreover, the four features of the aura matrix in Figures 4-15-4-18 have nearly identical flat regions for these temperature ranges.

The first problem concerns uniqueness of the estimate. If the aura matrix does

not change then the pattern does not change, and all temperatures in the plateau regions will correspond to the same pattern. It follows from $T = 1/\beta$, with T in the plateau region, that many different bonding parameters will also correspond to these patterns. This saturation at both ends is analogous to ice (steam) remaining the same as the temperature is lowered (raised) past the freezing (boiling) point.

A second problem concerns equilibrium. As we have now indicated several times, most of the patterns synthesized in the texture modeling literature do not appear to have been in equilibrium or in their minimum energy configurations. Hence, the parameters estimated for them will generally not correspond to the parameters used to synthesize them. With our temperature and graylevel results, one ought to be able to characterize equilibrium and account for these differences.

Some MRF estimation algorithms require all clique configurations to be represented in the samples presented for estimation. We have shown that systematic bandwidth decreases occur which directly violate this condition. Such estimation methods will thus fail in these temperature (parameter) regions. In contrast, all of the aura matrix features are monotonic with respect to temperature in these regions. They can be used for recovering temperature even when all the configurations are not represented.

When the bandwidth changes are sharp, they partition the temperature scale into regions that can be considered to correspond to pure phases of the pattern. In these regions, the patterns should be well characterized by their temperatures. The final chapter of new results in this thesis examines the relationship of the aura matrix structure to energy, and how this structure changes during convergence. All of the features we have discussed, including Gibbs energy, relate directly to the aura matrix structure.

Chapter 6

Ground state texture patterns

6.1 Introduction

At zero temperature equilibrium the Markov/Gibbs random field (MRF) texture patterns will be in their "ground state," or state with minimum energy. Can texture patterns that occur in the ground states of the MRF be characterized? The answer is "yes" under some conditions.

In this chapter we will consider characterizing the patterns by specifying the structure of the aura matrix as the energy is minimized. The physical texture behavior described in Section 3.5 can then be used to provide intuition about the kinds of patterns which correspond to a given aura matrix structure.

By normalizing the aura matrix, and decomposing it into permutations, we are able to describe the structure of the aura matrix as the energy is minimized. We show that a "sharpening" process occurs, where the matrix moves from full-band to tridiagonal for an attractive auto-binomial isotropic field. An analogous sharpening along the anti-diagonal occurs for the repulsive case.

Because of the relation between aura and co-occurrence matrices, a zero in the aura matrix implies a corresponding zero in the co-occurrence matrix. The presence of a zero at $m(i,j)$ in the matrix corresponds to a restriction on colors i,j being neighbors – a very severe restriction for a texture model. Thus the results of the aura matrix structure have important implications for the kinds of textures which occur

as the Gibbs energy is optimized. This may also affect the patterns modeled by an MRF prior within an optimization context.

The assumptions which are specific to this chapter appear in Section 6.2. Derivations of the tridiagonal and anti-tridiagonal structure proceed in Section 6.3 for the auto-binomial model and in Section 6.4 for the Potts model. Important consequences of the matrix structure for texture modeling are discussed in Section 6.5.

6.2 Assumptions

The assumptions of Section 2.2.2 still hold in this chapter, as does the property of irreducibility of the aura matrix which was described in Section 3.2.4. The following discussion should elucidate the remaining assumptions.

6.2.1 Isotropy

Initially we assume isotropy so that $\beta_k = \beta$, leaving only one parameter in the energy function. This parameter will act as a scale factor in the isotropic optimization; only its sign is important. After deriving the structure for the isotropic case we will generalize to the anisotropic case.

6.2.2 Histograms, image and neighborhood sizes

We assume that the histogram is constrained to be uniform throughout the pattern formation, i.e., we use the maximum entropy prior with Metropolis exchange or equivalently constrained synthesis method. We further assume that the image size is "large" compared to both the neighborhood size and number of graylevels. This assumption can be formalized by letting the lattice dimension $N \to \infty$ while ν, n take typical image processing values $4 \leq \nu \leq 20$ and $2 \leq n \leq 256$. In practice, images of size 64×64 are large enough to demonstrate the MRF behavior.

Because the lattice is connected and $n \geq 2$ there are boundaries between the different graylevels. The "length," $m(g, g')$, can be associated with the boundary

between sets of color g and g'. Upper and lower bounds for $m(g, g')$ can be determined easily in some cases.

Example 6.1 *Consider the binary case with four nearest neighbors on an $M \times N$ lattice. The minimum boundary occurs when the colors clump into two regions. The boundary between the two regions will be as straight as possible, attaining in the limit a minimum length of $m(0,1) = 2\min(M, N)$. Note that if we did not assume a periodic boundary, then the minimum length would be $m(0,1) = \min(M, N)$ since the regions would no longer share an edge along the lattice boundary.*

Similarly, the maximum boundary length occurs when the two colors form a checkerboard; it has length $2NM$.

6.3 Structure of the auto-binomial aura matrix

6.3.1 Miscibility matrix and its decomposition into permutations

In Chapter 3 it was shown that the MRF energy function could be rewritten as a linear combination of aura measures. If the linear form is applied, then the problem of minimizing a homogeneous, isotropic, auto-binomial MRF energy is the same as

$$\begin{aligned} \max_{\mathbf{x}\in\Omega} \quad & \beta\left(\sum_{g\in\Lambda} g^2 m(g,g) + 2\sum_{g<g'} gg' m(g,g')\right) \\ \text{subject to} \quad & |\mathcal{S}_g| = \gamma = \frac{N^2}{n}, \ \forall g \in \Lambda = \{0, 1, \ldots, n-1\}. \end{aligned} \tag{6.1}$$

The maximization is over the set of image configurations; these configurations determine the values of the aura measures, $m(g, g')$. Only the histogram constraints are stated explicitly.

Let $\mathbf{g} = [0, 1, \ldots, n-1]^T$ be the vector of graylevel values and $\mathbf{A}$ be the aura

matrix. Then we have

$$\beta \left(\sum_{g \in \Lambda} g^2 m(g,g) + 2 \sum_{g<g'} g g' m(g,g') \right) = \beta \mathbf{g}^T \mathbf{A} \mathbf{g}. \tag{6.2}$$

The intent of this chapter is to show what kind of structure will occur in $\mathbf{A}$ as (6.1) is solved.

Normalizing $\mathbf{A}$ by the uniform histogram level γ and the neighborhood size ν makes $\mathbf{A}$ into a doubly stochastic *miscibility matrix*,

$$\mathbf{M} = \frac{1}{\gamma \nu} \mathbf{A}. \tag{6.3}$$

We have been denoting the elements of $\mathbf{A}$ by $m(i,j)$; we denote the elements of $\mathbf{M}$ by $\mathbf{m}(i,j)$.

The optimization problem in (6.1) now becomes

$$\begin{aligned} \max_{\mathbf{x} \in \boldsymbol{\Omega}} \quad & \beta \mathbf{g}^T \mathbf{M} \mathbf{g} \\ \text{subject to} \quad & |\mathcal{S}_g| = \gamma, \ \forall g \in \Lambda. \end{aligned} \tag{6.4}$$

When the model parameter $\beta > 0$ the field interaction is attractive, and when $\beta < 0$ it is repulsive. Since a constant scale factor in (6.4) does not change its solution, we assume $|\beta| = 1$.

The following result by Birkhoff is the key new insight used to derive the structure in the aura matrix.

Proposition 6.2 *Every doubly stochastic matrix is a convex combination of permutation matrices.*

Proof: A proof appears in [60]. ∎

A review of the basic usage of permutations is provided in Appendix A.

Let $\mathcal{P}_n$ be the group of all permutations of the set $\Lambda = \{0, 1, \ldots, n-1\}$. Denote by $\mathbf{P}_\sigma \in \Re^{n \times n}$ the permutation matrix corresponding to $\sigma \in \mathcal{P}_n$. From Proposition 6.2,

$\mathbf{M}$ can be decomposed as

$$\mathbf{M} = \sum_{\sigma \in \mathcal{P}_n} \alpha_\sigma \mathbf{P}_\sigma, \tag{6.5}$$

where the α_σ's satisfy the constraints,

$$\begin{aligned} &\alpha_\sigma \geq 0 \\ &\sum_{\sigma \in \mathcal{P}_n} \alpha_\sigma = 1. \end{aligned}$$

Combining (6.5) with (6.4) gives

$$\begin{aligned} \max_{\mathbf{x} \in \Omega} \quad & \beta \sum_{\sigma \in \mathcal{P}_n} \alpha_\sigma \mathbf{g}^T \mathbf{P}_\sigma \mathbf{g} \\ \text{subject to} \quad & |\mathcal{S}_g| = \gamma, \ \ \forall g \in \Lambda \\ & \alpha_\sigma \geq 0 \\ & \sum_{\sigma \in \mathcal{P}_n} \alpha_\sigma = 1. \end{aligned} \tag{6.6}$$

We will focus on solving the problem in (6.6) subject to the assumptions of Section 6.2.

6.3.2 Aura matrix structure: example

Before proceeding with derivations it is helpful to consider an example of the aura matrix structure. Returning to Figure 4-1, we compute the aura matrices for each of the four patterns in column (b). Each pattern is isotropic with $\beta = 0.5$. The four aura matrices are shown in Figure 6-1.

Suppose the elements along each diagonal of $\mathbf{M}$ are summed,

$$M_\delta = \sum_{i-j=\delta} \mathbf{m}(i,j), \quad \delta = -(n-1), \ldots, 0, \ldots, n-1.$$

If M_δ vs. δ were plotted with respect to energy, then it would be observed to "sharpen" around $\delta = 0$ as the energy is decreased. This corresponds to the matrices becoming more and more diagonal dominant; Figure 6-2 shows the M_δ for the aura matrices of Figure 6-1.

$$i = 0: \quad \mathbf{A} = \begin{bmatrix} 2264 & 1847 & 1574 & 1311 & 1093 & 922 & 696 & 533 \\ 1847 & 1652 & 1497 & 1395 & 1225 & 1026 & 896 & 702 \\ 1574 & 1497 & 1426 & 1367 & 1259 & 1216 & 1004 & 897 \\ 1311 & 1395 & 1367 & 1332 & 1270 & 1266 & 1248 & 1051 \\ 1093 & 1225 & 1259 & 1270 & 1304 & 1300 & 1421 & 1368 \\ 922 & 1026 & 1216 & 1266 & 1300 & 1352 & 1519 & 1639 \\ 696 & 896 & 1004 & 1248 & 1421 & 1519 & 1618 & 1838 \\ 533 & 702 & 897 & 1051 & 1368 & 1639 & 1838 & 2212 \end{bmatrix}$$

$$i = 10: \quad \mathbf{A} = \begin{bmatrix} 5742 & 2886 & 1133 & 377 & 91 & 11 & 0 & 0 \\ 2886 & 3212 & 2301 & 1217 & 472 & 119 & 29 & 4 \\ 1133 & 2301 & 2822 & 2148 & 1205 & 495 & 119 & 17 \\ 377 & 1217 & 2148 & 2568 & 2181 & 1216 & 460 & 73 \\ 91 & 472 & 1205 & 2181 & 2534 & 2132 & 1247 & 378 \\ 11 & 119 & 495 & 1216 & 2132 & 2718 & 2358 & 1191 \\ 0 & 29 & 119 & 460 & 1247 & 2358 & 3210 & 2817 \\ 0 & 4 & 17 & 73 & 378 & 1191 & 2817 & 5760 \end{bmatrix}$$

$$i = 100: \quad \mathbf{A} = \begin{bmatrix} 8200 & 1944 & 95 & 1 & 0 & 0 & 0 & 0 \\ 1944 & 5584 & 2450 & 260 & 2 & 0 & 0 & 0 \\ 95 & 2450 & 4614 & 2587 & 489 & 5 & 0 & 0 \\ 1 & 260 & 2587 & 4414 & 2658 & 316 & 4 & 0 \\ 0 & 2 & 489 & 2658 & 4320 & 2529 & 242 & 0 \\ 0 & 0 & 5 & 316 & 2529 & 4986 & 2302 & 102 \\ 0 & 0 & 0 & 4 & 242 & 2302 & 5682 & 2010 \\ 0 & 0 & 0 & 0 & 0 & 102 & 2010 & 8128 \end{bmatrix}$$

$$i = 1000: \mathbf{A} = \begin{bmatrix} 8758 & 1466 & 16 & 0 & 0 & 0 & 0 & 0 \\ 1466 & 7006 & 1753 & 15 & 0 & 0 & 0 & 0 \\ 16 & 1753 & 6680 & 1782 & 9 & 0 & 0 & 0 \\ 0 & 15 & 1782 & 6508 & 1883 & 52 & 0 & 0 \\ 0 & 0 & 9 & 1883 & 6520 & 1818 & 10 & 0 \\ 0 & 0 & 0 & 52 & 1818 & 6804 & 1562 & 4 \\ 0 & 0 & 0 & 0 & 10 & 1562 & 7516 & 1152 \\ 0 & 0 & 0 & 0 & 0 & 4 & 1152 & 9084 \end{bmatrix}$$

Figure 6-1: Aura matrices corresponding to the four textures in Figure 4-1 (b).

Is this behavior typical? The derivations which follow indicate "yes." We will show that for the isotropic attractive case, under suitable assumptions, this sharpening will always occur. For the isotropic repulsive case it will also occur, but along the anti-diagonal. For anisotropic cases the behavior will be a combination of these "sharpening" effects.

6.3.3 Attractive case

For the attractive case, $\beta = 1$, we want to characterize the σ's which maximize the sum of positive numbers,

$$\sum_{\sigma \in \mathcal{P}_n} \alpha_\sigma \mathbf{g}^T \mathbf{P}_\sigma \mathbf{g}, \tag{6.7}$$

subject to the constraints and assumptions already stated. The resulting set of $\mathbf{P}_\sigma$'s which maximizes (6.7) will provide the structure of the ground state aura matrix.

"Best" solution is infeasible

Since $\mathbf{P}_\sigma$ is a permutation matrix it is orthogonal and preserves the norm, i.e., $\|\mathbf{P}_\sigma \mathbf{g}\| = \|\mathbf{g}\|$. Hence, the dot product $\mathbf{g}^T \mathbf{P}_\sigma \mathbf{g}$ is equal to $\|g\|^2 \cos\theta_\sigma$ where θ_σ is the angle between $\mathbf{g}$ and $\mathbf{P}_\sigma \mathbf{g}$. Observe that the maximum of this dot product occurs when $\cos\theta_\sigma = 1$, corresponding to $\mathbf{P}_\sigma = \mathbf{I}$, the identity matrix. Using only the identity permutation, σ_I, there is a trivial solution which maximizes (6.7): $\aleph = \{\alpha_\sigma \mid \alpha_\sigma = 1,\ \sigma = \sigma_I,$ and $\alpha_\sigma = 0$ for all other $\sigma \in \mathcal{P}_n\}$.

However, the trivial solution is infeasible. By assumption of a connected lattice $\mathbf{M}$ must be irreducible; thus, $\mathbf{M}$ cannot be diagonal, and consequently, it cannot be constructed from only a weighted identity matrix.

To summarize, although the identity matrix maximizes the objective function it is not a feasible solution. If it were feasible the "sharpening process" would yield an M_δ that is just an impulse at $\delta = 0$.

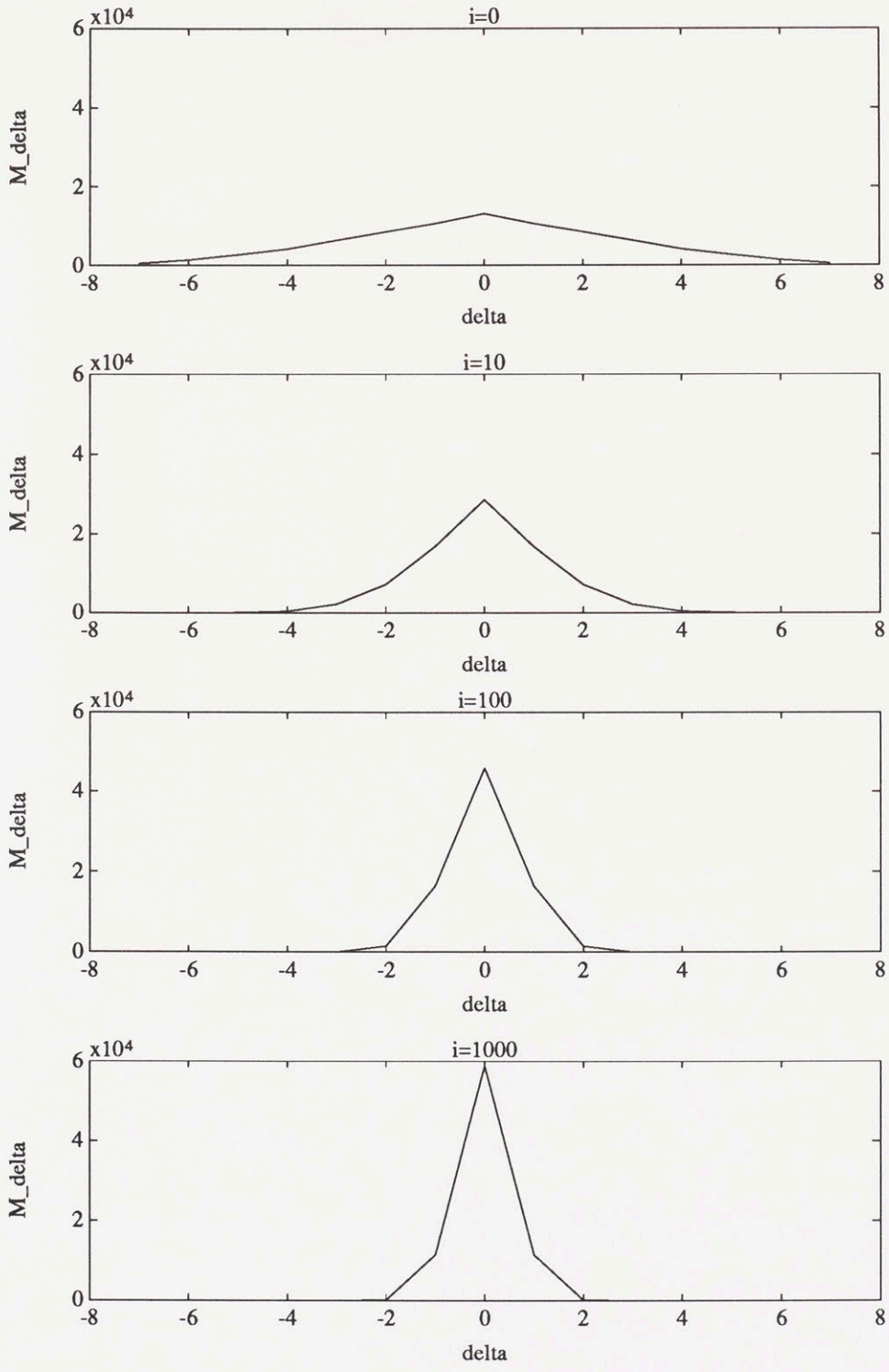

Figure 6-2: Sharpening of the bandwidth function, M_δ, for the four textures in Figure 4-1 (b).

"Next best" solution

Now we characterize the permutations which give the "next best" maximum of the objective function. With a sufficiently large lattice, these do provide a feasible solution.

Note that maximizing (6.7) is the same as minimizing

$$\mu = \mathbf{g}^T\mathbf{g} - \sum_{\sigma \in \mathcal{P}_n} \alpha_\sigma \mathbf{g}^T \mathbf{P}_\sigma \mathbf{g}. \tag{6.8}$$

which can also be written as

$$\begin{aligned} \mu &= \sum_{\sigma \in \mathcal{P}_n} \alpha_\sigma \left(\mathbf{g}^T\mathbf{g} - \mathbf{g}^T \mathbf{P}_\sigma \mathbf{g} \right) && (6.9) \\ &= \sum_{\sigma \in \mathcal{P}_n} \alpha_\sigma \mu(\sigma), && (6.10) \end{aligned}$$

because $\sum_{\sigma \in \mathcal{P}_n} \alpha_\sigma = 1$.

It suffices now to find the "next best" maximum by choosing $\mathbf{P}_\sigma \neq \mathbf{I}$ that minimizes the "mismatch,"

$$\mu(\sigma) = \mathbf{g}^T\mathbf{g} - \mathbf{g}^T \mathbf{P}_\sigma \mathbf{g}. \tag{6.11}$$

Intuitively we must find the permutations which make $\mathbf{P}_\sigma \mathbf{g}$ as close as possible to $\mathbf{g}$ but not equal to it. A standard result from algebra [31] states that every permutation can be written as a product of its disjoint cycles $\sigma = \sigma_1 \sigma_2 \ldots \sigma_k$.

Let Λ_j denote the set of elements in Λ which the cycle σ_j permutes. Clearly we have

$$\bigcup_{1 \leq j \leq k} \Lambda_j = \Lambda, \tag{6.12}$$

and since the cycles are disjoint, the Λ_j form a partition of Λ. Observe that if $q \in \Lambda_j$, then $\sigma_j(q) \in \Lambda_j$. Also, $\forall q \notin \sigma_j$, we have $\sigma_j(q) = q$.

Let the length of a cycle σ_j be the number of elements of Λ_j and denote this length by l_j. Denote the set of adjacent transpositions (cycles which contain only two adjacent elements from Λ) by $\mathcal{P}_\tau \subset \mathcal{P}_n$. Note that for all $\sigma \in \mathcal{P}_\tau$, the corresponding permutation matrix $\mathbf{P}_\sigma$ is tridiagonal.

Example 6.3 *Consider the case where $n = 4$. Then the following three permutation matrices correspond to $\sigma \in \mathcal{P}_\tau$:*

$$\begin{bmatrix} 0 & 1 & 0 & 0 \\ 1 & 0 & 0 & 0 \\ 0 & 0 & 1 & 0 \\ 0 & 0 & 0 & 1 \end{bmatrix} \qquad \begin{bmatrix} 1 & 0 & 0 & 0 \\ 0 & 0 & 1 & 0 \\ 0 & 1 & 0 & 0 \\ 0 & 0 & 0 & 1 \end{bmatrix} \qquad \begin{bmatrix} 1 & 0 & 0 & 0 \\ 0 & 1 & 0 & 0 \\ 0 & 0 & 0 & 1 \\ 0 & 0 & 1 & 0 \end{bmatrix}.$$

Now we will show that the $n-1$ transpositions in $\mathcal{P}_\tau$ minimize the mismatch $\mu(\sigma)$. Moreover, these give feasible solutions to the optimization problem. In other words the set $\mathcal{P}_\tau^* = \mathcal{P}_\tau \cup \{\mathbf{I}\}$ both maximizes (6.6) and satisfies all the constraints. The structure of the matrices in this set provides the structure of the ground state aura matrix.

We have the following two results based on the lemmas in Appendix A.

Proposition 6.4 *Let σ be a permutation different from the identity. Write the decomposition of σ into disjoint cycles as $\tau_1 \dots \tau_t \sigma_1 \dots \sigma_k$, where $\tau_1, \dots, \tau_t$ represent the disjoint cycles which are adjacent transpositions. Denote the lengths of $\sigma_1, \dots, \sigma_k$ by $l_1, \dots, l_k \geq 2$, respectively. Then*

$$\mu(\sigma) \geq t + \sum_{j=1}^{k} l_j.$$

Corollary 6.5 *Let $\sigma \in \mathcal{P}_n$ be an arbitrary permutation. Then $\mu(\sigma) = 1$ if and only if σ is an adjacent transposition.*

It follows that the adjacent transposition has the minimum mismatch of all permutations except the identity permutation. Therefore, for all $\sigma \in \mathcal{P}_\tau$, the "next best" maximum of (6.7) is given by $\mathbf{P}_\sigma$.

Now we revisit the optimization problem in (6.6) for the attractive case, keeping only the elements of $\mathcal{P}_n$ which are adjacent transpositions and the identity permutation. Let $w_0 = \mathbf{g}^T \mathbf{I} \mathbf{g}$, and let $w_1 = \mathbf{g}^T \mathbf{P}_\sigma \mathbf{g}$, $\sigma \in \mathcal{P}_\tau$. Because σ is an adjacent

transposition, by Corollary 6.5 $w_1 = w_0 - 1$. We now have

$$\begin{aligned} \max \quad & \alpha_0 w_0 + \left(\sum_{i=1}^{n-1} \alpha_i\right)(w_0 - 1) \\ \text{subject to} \quad & \alpha_0, \alpha_i > 0 \\ & \alpha_0 + \sum_{i=1}^{n-1} \alpha_i = 1. \end{aligned} \tag{6.13}$$

Consider (6.13) now for the two cases, $n = 2$, and $n > 2$. For $n = 2$ we have

$$\begin{aligned} \max \quad & (\alpha_0 + \alpha_1)w_0 - \alpha_1 \\ \text{subject to} \quad & \alpha_0, \alpha_1 > 0 \\ & \alpha_0 + \alpha_1 = 1. \end{aligned} \tag{6.14}$$

so that the goal is to minimize $\alpha_1 > 0$. Observe that α_1 corresponds to the value of the miscibility matrix $\mathbf{m}(0,1)$. This value has a lower bound determined by the geometry of the problem. From Section 6.2.2 the lower bound for the order $p = 1$ field on the $N \times N$ lattice is

$$\mathbf{m}(0,1) = \frac{2N}{(\frac{N^2}{2})4} = \frac{1}{N}.$$

For $n > 2$ observe that the expected values of $\alpha_1, \alpha_2, \ldots, \alpha_{n-1}$ are equal since their weights, $w_0 - 1$, are constant. We need only to characterize α_0 and the expected value of the others, $\alpha_1 = \mathrm{E}(\alpha_i)$. The problem can be rewritten as,

$$\begin{aligned} \max \quad & [\alpha_0 + (n-1)\alpha_1]w_0 - (n-1)\alpha_1 \\ \text{subject to} \quad & \alpha_0, \alpha_1 > 0 \\ & \alpha_0 + (n-1)\alpha_1 = 1. \end{aligned} \tag{6.15}$$

By writing the problem in this form, it is evident that the problem is solved by minimizing α_1, i.e., setting it equal to the lower bound of $\mathbf{m}(0,1)$.

From miscibility analysis we know that $\gamma\nu\mathbf{m}(0,1)$ is bounded below by the mini-

mum boundary length between the two graylevels. The only reason we would not be able to find alphas which solve (6.15) is if there are not enough elements of graylevel 1 to surround the set of graylevel 0. If there are not enough 1's, then it must be true that $m(0,i) > 0$ for some other graylevel $i > 1$. If this were the case then the matrix would not be tridiagonal.

Minimum boundary approximations

In the plane, the minimum boundary around a set $\mathcal{S}_g$ of size γ is approximately the circumference of a circle of area γ. The circumference can be roughly approximated by the aura measures for the $p = 1, 2$ order neighborhoods. Let $\gamma = \pi r^2$ so that $r = \sqrt{\gamma/\pi}$, and the circumference is $c = 2\sqrt{\gamma\pi}$. For approximately $\gamma > c$, i.e., $\gamma > 4\pi$, the set $\mathcal{S}_g$ can be surrounded by the set $\mathcal{S}_{g'}$.

For higher order MRF's these approximations also need to incorporate the width, ω, of the neighborhood. The intuition is that the measure is formed over a wider neighborhood. If it is to only contain one color, then there will be need to be enough of that color to surround the set of 0's throughout the width of that neighborhood. Thus we would need approximately $\gamma > 4\pi\omega$.

With the uniform histogram constraint, we require $|\mathcal{S}_g| = NM/n > 4\pi\omega$. For $\omega = 1$ the 64×64 image is sufficiently large to show the structure for a standard 8 bit image.

Minimum boundary configurations

The general problem of determining these configurations is very difficult. With the assumptions we have made, where $\gamma = NM/n$ is sufficiently large, then there are orderly configurations for the colors which always permit the tridiagonal structure. The "formula" for such a configuration when $n > 2$ is as follows:

1. Color 0 forms a blob, and is surrounded by color 1.

2. Color $n-1$ forms a blob, and is surrounded by color $n-2$.

3. The remaining colors, $2, \ldots, n-2$ form ordered stripes between colors 1 and $n-2$.

The patterns which were shown in Figure 3-3 obey this "formula."

The above derivations are summarized by the following statement:

Proposition 6.6 *For $NM/n \gg 4\pi\omega$ the ground state aura matrix of the isotropic attractive auto-binomial MRF is tridiagonal.*

Given the aura matrix structure, its trace can also be characterized.

Corollary 6.7 *The trace of the ground state aura matrix of the isotropic attractive auto-binomial MRF will increase linearly with respect to the number of graylevels. Let α_0 be the weight of the identity permutation. Then,*

$$\sum_{i=0}^{n-1} m(i,i) = \gamma\nu \sum_{i=0}^{n-1} \mathbf{m}(i,i) = \gamma\nu[n + (2\alpha_0 - 2)].$$

Proof: From the decomposition of the ground state miscibility matrix we have,

$$\mathbf{M} = \alpha_0 \mathbf{I} + \alpha_1 \sum_{\sigma \in \mathcal{P}_\tau} \mathbf{P}_\sigma.$$

Each of the $n-1$ nearest-neighbor permutation matrices has $n-2$ elements remaining on the diagonal. Summing, and using the constraint on the alphas, its trace is

$$\begin{aligned} \sum_{i=0}^{n-1} \mathbf{m}(i,i) &= n\alpha_0 + (n-2)(n-1)\alpha_1 \\ &= n\alpha_0 + (n-2)(1-\alpha_0) \\ &= n + 2\alpha_0 - 2. \end{aligned}$$

The aura matrix trace follows by scaling the miscibility matrix entries. ∎

The trace for the ground state aura matrix is bounded above by n, and could only equal n if $\alpha_0 = 1$, i.e., the aura matrix becomes reducible.

If the relative bounds are not satisfied then the new structure can be predicted by continuing the analysis method set forth in this thesis. For example, the "next

best" set of permutations are those in the set $\mathcal{P}_n - \mathcal{P}_\tau^*$ with minimum mismatch. For $n \geq 4$ this would be the permutations comprised of two adjacent transpositions, i.e., $\mu(\sigma) = 2$. Use of these would still preserve the tridiagonal structure. The structure will increase to penta-diagonal at the point where cycles of length 3 are required, and so forth.

In the next section where $\beta < 0$, we will show that there is a nice symmetry which enables this same analysis to be applied "at the other end", finding the permutations with *maximum* mismatch. These also have the property of maximizing miscibilities, hence maximizing boundary lengths.

6.3.4 Repulsive case

For the repulsive case, $\beta = -1$, we want to characterize the σ's which minimize the sum of positive numbers,

$$\sum_{\sigma \in \mathcal{P}_n} \alpha_\sigma \mathbf{g}^T \mathbf{P}_\sigma \mathbf{g}, \tag{6.16}$$

subject to the constraints and assumptions already stated. For $n = 2$, the minimum value 0 is reached by setting

$$\mathbf{P}_\sigma = \begin{bmatrix} 0 & 1 \\ 1 & 0 \end{bmatrix}.$$

Observe that for $n > 2$ the minimum is strictly positive; both $\mathbf{g}$ and $\mathbf{P}_\sigma \mathbf{g}$ are in the positive orthant of $\Re^n$. Observe also that minimizing the above sum is equivalent to maximizing the mismatch, $\mu(\sigma)$ of (6.11).

Let ρ be the permutation that reverses the order of the components of the vector $\mathbf{g}$. For $i \in \Lambda$, we have $\rho(i) = n - 1 - i$. We will show now that the mismatch of the reversing permutation $\mu(\rho)$ is an upper bound on $\mu(\sigma)$, $\sigma \in \mathcal{P}_n$. We will also show that $\mu(\rho\tau)$, where τ is an adjacent transposition, is an upper bound on $\mu(\sigma)$, $\sigma \in \mathcal{P}_n - \{\rho\}$.

In order to accomplish this we consider the difference,

$$\Delta(\sigma) = \mu(\rho) - \mu(\rho\sigma) = \sum_{i=0}^{n-1} i[\rho\sigma(i) - \rho(i)]. \tag{6.17}$$

Note that every permutation $\xi \in \mathcal{P}_n$ can be reversed, and written as $\xi = \rho\sigma$ where $\sigma \in \mathcal{P}_n$.

Lemma 6.8 *Let $\sigma \in \mathcal{P}_n$. Then*

$$\Delta(\sigma) = \mu(\sigma).$$

Proof:

$$\begin{aligned}
\Delta(\sigma) &= \sum_{i=0}^{n-1} i[\rho\sigma(i) - \rho(i)] \\
&= \sum_{i=0}^{n-1} i[n-1-\sigma(i) - (n-1-i)] \\
&= \sum_{i=0}^{n-1} i[i - \sigma(i))] \\
&= \mu(\sigma).
\end{aligned}$$

■

This lemma elucidates a nice symmetry in the permutations which enables the use of results from the attractive case to solve the repulsive case. In particular, because of the bounds on $\mu(\sigma)$ given in Proposition 6.4, the following is also true.

Proposition 6.9 *Let σ be a permutation different from the identity. Write the decomposition of σ into disjoint cycles as $\tau_1 \ldots \tau_t \sigma_1 \ldots \sigma_k$, using $\tau_1, \ldots, \tau_t$ to represent the disjoint cycles which are adjacent transpositions. Denote the lengths of $\sigma_1, \ldots, \sigma_k$ by $l_1, \ldots, l_k \geq 2$, respectively. Then*

$$\Delta(\sigma) \geq t + \sum_{j=1}^{k} l_j.$$

It follows that the difference $\Delta(\sigma) = \mu(\rho) - \mu(\rho\sigma)$ is bounded below by a positive number so that $\mu(\rho)$ is the maximum mismatch. The "next best" maximum is given by the adjacent transposition, which has mismatch of 1.

Corollary 6.10 *Let $\sigma \in \mathcal{P}_n$ be an arbitrary permutation. Then $\mu(\rho\sigma) = \mu(\rho) - 1$ if and only if $\rho\sigma$ is an adjacent transposition.*

We conclude that the permutations $\rho\sigma$, $\sigma \in \mathcal{P}_\tau$ have the maximum mismatch of all permutations except the reversing permutation, ρ. Thus, for all $\sigma \in \mathcal{P}_\tau$, we have that $\mathbf{P}_{\rho\sigma}$ gives the "next best" minimum of (6.16).

Symmetry between attractive and repulsive solutions

As mentioned, we have found that there is a nice symmetry present in the solutions to the repulsive and attractive cases. Let $\mathbf{r} = \mathbf{P}_\rho \mathbf{g}$, and note also $\mathbf{g} = \mathbf{P}_\rho \mathbf{r}$.

Proposition 6.11 *Let* $\aleph = \{\alpha_\sigma^* \geq 0, \sigma \in \mathcal{P}_\tau\}$ *such that* $\sum_{\sigma \in \mathcal{P}_n} \alpha_\sigma^* = 1$. *Then* $\aleph$ *is a solution of*

$$\min \sum_{\sigma \in \mathcal{P}_n} \alpha_\sigma \mathbf{r}^T \mathbf{P}_\sigma \mathbf{g}$$

if and only if $\aleph$ *is a solution of*

$$\max \sum_{\sigma \in \mathcal{P}_n} \alpha_\sigma \mathbf{g}^T \mathbf{P}_\sigma \mathbf{g}.$$

Proof: Suppose $\aleph$ is a solution of

$$\max \sum_{\sigma \in \mathcal{P}_n} \alpha_\sigma \mathbf{g}^T \mathbf{P}_\sigma \mathbf{g},$$

then it also solves the problem

$$\min \sum_{\sigma \in \mathcal{P}_n} \alpha_\sigma \left[\mathbf{g}^T \mathbf{g} - \mathbf{g}^T \mathbf{P}_\sigma \mathbf{g}\right],$$

which is by definition and by Lemma 6.8,

$$\min \sum_{\sigma \in \mathcal{P}_n} \alpha_\sigma \mu(\sigma) = \min \sum_{\sigma \in \mathcal{P}_n} \alpha_\sigma \Delta(\sigma).$$

The right hand problem is equivalent to

$$\min \sum_{\sigma \in \mathcal{P}_n} \alpha_\sigma \left[\mathbf{g}^T \mathbf{P}_\rho \mathbf{P}_\sigma \mathbf{g} - \mathbf{g}^T \mathbf{P}_\rho \mathbf{g}\right],$$

or noting that $\mathbf{P}_\rho^T = \mathbf{P}_\rho$,

$$\min \sum_{\sigma \in \mathcal{P}_n} \alpha_\sigma \left[\mathbf{r}^T \mathbf{P}_\sigma \mathbf{g} - \mathbf{g}^T \mathbf{r} \right].$$

This problem is equivalent to the maximization,

$$\max \sum_{\sigma \in \mathcal{P}_n} \alpha_\sigma \left[\mathbf{g}^T \mathbf{r} - \mathbf{r}^T \mathbf{P}_\sigma \mathbf{g} \right],$$

which is solved by $\aleph$ if and only if the following is solved by $\aleph$:

$$\min \sum_{\sigma \in \mathcal{P}_n} \alpha_\sigma \mathbf{r}^T \mathbf{P}_\sigma \mathbf{g}.$$

■

Reviewing, we have that the identity permutation is the best unconstrained solution to the symmetric problems:

$$\begin{aligned} &\max_{\sigma \in \mathcal{P}_n} \mathbf{g}^T \mathbf{P}_\sigma \mathbf{g} \\ &\quad = \mathbf{g}^T \mathbf{g} \\ &\quad = \sum_{i=0}^{n-1} i^2, \end{aligned} \tag{6.18}$$

and

$$\begin{aligned} &\min_{\sigma \in \mathcal{P}_n} \mathbf{r}^T \mathbf{P}_\sigma \mathbf{g} \\ &\quad = \mathbf{r}^T \mathbf{g} \\ &\quad = \sum_{i=0}^{n-1} (n-1-i) i. \end{aligned} \tag{6.19}$$

Continuing, let $\mathbf{P}_\tau$ represent any of the matrices computing an adjacent transposition. Then $\mathbf{P}_\tau$ is the solution to the symmetric problems:

$$\begin{aligned} &\max_{\sigma \in \mathcal{P}_n - \{\mathbf{I}\}} \mathbf{g}^T \mathbf{P}_\sigma \mathbf{g} \\ &\quad = \mathbf{g}^T \mathbf{P}_\tau \mathbf{g} \end{aligned} \tag{6.20}$$

$$= \mathbf{g}^T\mathbf{g} - 1,$$

and

$$\begin{aligned} &\min_{\sigma \in \mathcal{P}_n - \{\mathbf{I}\}} \mathbf{r}^T \mathbf{P}_\sigma \mathbf{g} \\ &= \mathbf{r}^T \mathbf{P}_\tau \mathbf{g} \\ &= \mathbf{r}^T \mathbf{g} + 1. \end{aligned} \tag{6.21}$$

Compare the two objective functions in these problems. If we replace $\mathbf{P}_\sigma$ in the minimization with $\mathbf{P}_\sigma \mathbf{P}_\rho$, we obtain

$$\mathbf{r}^T \mathbf{P}_\sigma \mathbf{P}_\rho \mathbf{g} = \mathbf{g}^T \mathbf{P}_\sigma \mathbf{P}_\rho \mathbf{r} = \mathbf{g}^T \mathbf{P}_\sigma \mathbf{g},$$

giving the two problems the same original objective function. The effect of this replacement is that the solution to the minimization is just the solution to the maximization, permuted by ρ, a reflection.

Therefore, when the ground state aura matrix for the attractive case is tridiagonal, then the ground state aura matrix for the repulsive case will be anti-tridiagonal. Given the same assumptions on the optimizations the structure of the ground state matrix for one case will be the reversing reflection of the structure for the other case. In the same way, the sharpening that occurs along the diagonal for the attractive case will occur along the anti-diagonal for the repulsive case.

Combining this symmetry with Proposition 6.6, we can state the following two results.

Proposition 6.12 *For $NM/n \gg 4\pi\omega$ the ground state aura matrix of the isotropic repulsive auto-binomial MRF is anti-tridiagonal.*

Corollary 6.13 *The anti-trace of the ground state aura matrix of the isotropic repulsive auto-binomial MRF will increase linearly with respect to the number of graylevels.*

Let α_0 be the weight of the identity permutation. Then,

$$\sum_{i=0}^{n-1} m(i,i) = \gamma\nu \sum_{i=0}^{n-1} \mathbf{m}(i,i) = \gamma\nu[n + (2\alpha_0 - 2)].$$

6.3.5 Anisotropic case

The previous two sections described the structure which occurs for the isotropic MRF with positive and negative β, respectively. Here we consider the anisotropic case where β may vary both in sign and magnitude for different order neighborhoods.

Let $m(g, g')$ denote the aura measure of an anisotropic MRF. Repeating (3.12), the goal is to maximize

$$\sum_{k=1}^{K} \beta_k \mathbf{g}^T \mathbf{A}^k \mathbf{g}, \tag{6.22}$$

where $\mathbf{A}^k$ is the corresponding symmetric aura matrix of $m^k(g, g')$'s, the measures over the isotropic subneighborhoods. Optimizing (6.22) corresponds to individually optimizing the $\beta_k \mathbf{g}^T \mathbf{A}^k \mathbf{g}$'s since they are over disjoint neighborhoods. Each of these terms then corresponds to an isotropic attractive or repulsive case.

For the first and second order MRF the subneighborhoods are "connected" in the sense that one can get from any neighbor to any other without leaving the neighborhood. In this case, or in the case of higher order neighborhoods and isotropy, the aura matrix is irreducible and the individual attractive or repulsive terms can be optimized as in the preceding sections. If the magnitudes of the bonding parameters, $|\beta_k|$, are constant for all k, and the conditions are such that Propositions 6.6 and 6.12 are valid, then the ground state aura matrices for each of the subneigborhoods will be either tridiagonal or anti-tridiagonal.

An example texture with aura matrices formed over subneighborhoods is shown in Figure 6-3. In this figure the patterns are not yet in their minimum energy configuration although the aura matrix structure is already present.

For the third and fourth order anisotropic MRF, if the anisotropy is such that one or more of the subneighborhoods are not connected, then the aura matrix can become reducible and the lower bound conditions need minor modification. We do

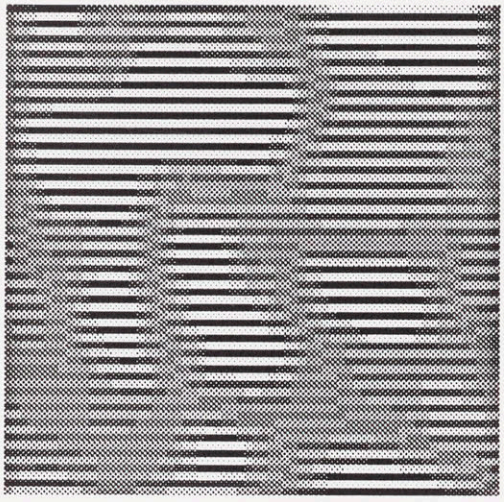

$$\mathbf{A}^1 = \begin{bmatrix} 926 & 98 & 0 & 0 & 0 & 0 & 0 & 0 \\ 98 & 772 & 154 & 0 & 0 & 0 & 0 & 0 \\ 0 & 154 & 690 & 180 & 0 & 0 & 0 & 0 \\ 0 & 0 & 180 & 678 & 166 & 0 & 0 & 0 \\ 0 & 0 & 0 & 166 & 680 & 178 & 0 & 0 \\ 0 & 0 & 0 & 0 & 178 & 690 & 156 & 0 \\ 0 & 0 & 0 & 0 & 0 & 156 & 774 & 94 \\ 0 & 0 & 0 & 0 & 0 & 0 & 94 & 930 \end{bmatrix}$$

$$\mathbf{A}^2 = \begin{bmatrix} 0 & 0 & 0 & 0 & 0 & 0 & 97 & 927 \\ 0 & 0 & 0 & 0 & 0 & 115 & 812 & 97 \\ 0 & 0 & 0 & 0 & 141 & 768 & 115 & 0 \\ 0 & 0 & 0 & 120 & 763 & 141 & 0 & 0 \\ 0 & 0 & 141 & 763 & 120 & 0 & 0 & 0 \\ 0 & 115 & 768 & 141 & 0 & 0 & 0 & 0 \\ 97 & 812 & 115 & 0 & 0 & 0 & 0 & 0 \\ 927 & 97 & 0 & 0 & 0 & 0 & 0 & 0 \end{bmatrix}$$

Figure 6-3: This 64×64 pattern was synthesized using a first order MRF with $n = 8$, $\beta_1 = 2$ (horizontal), $\beta_2 = 2$ (vertical), and $c = 0.1$ with log annealing for 1100 iterations, $i_{eq} = 10$. The aura matrices for the two isotropic subneighborhoods are shown to illustrate their tridiagonal and anti-tridiagonal structure.

not go into detail here, but give an example where this anisotropy will give different aura structure.

Example 6.14 *Suppose that β_6 is different from the other β_k, where $\mathcal{N}_s^6$ is the subneighborhood corresponding to the two horizontal third order elements. This subneighborhood is not connected since sites s and $s-(2,0)$ are separated by an element not in $\mathcal{N}_s^6$. Now consider a lattice with a pattern of binary vertical stripes, alternating every other pixel. Taking aura measures with respect to $\mathcal{N}_s^6$, this pattern will generate the diagonal aura matrix,*

$$\mathbf{A} = \begin{bmatrix} NM & 0 \\ 0 & NM \end{bmatrix}.$$

This matrix is allowed to be reducible since effectively the non-connected neighborhood breaks the lattice.

Special cases like the one in Example 6.14 can be analyzed using the aura framework. Only the interpretation of the pattern behavior requires slight modification. In Example 6.14 the notion of clustering is over the new disconnected neighborhood – so that the "clustering" behavior will be remapped to the geometry of stripes separated by one site. The same principle of "sharpening" will still hold for the aura matrix, but the interpretation of the texture it generates will be a mapping of the mixing/separation behavior onto the new geometry.

For $|\beta_k|$ varying, the terms with largest $|\beta_k|$ will become tridiagonal or anti-tridiagonal fastest following the interpretation in Chapter 4 of bonding parameters as annealing rates. The interaction of different rates in different directions leads to textural behavior that is much more difficult to predict, and often quite a bit more interesting visually.

6.4 Structure of the Potts aura matrix

Although the ground state aura matrix has different structure for the Potts model, it can be derived in a similar way. We make the same assumptions as for the auto-

binomial model. Using the linear form, the problem which arises while minimizing the homogeneous, isotropic, Potts energy is

$$\begin{aligned} \max_{\mathbf{x}\in\Omega} \quad & \beta\left(\sum_{g\in\Lambda} m(g,g) - 2\sum_{g<g'} m(g,g')\right) \\ \text{subject to} \quad & |\mathcal{S}_g| = \gamma = \frac{N^2}{n}, \ \ \forall g \in \Lambda = \{0,1,\ldots,n-1\}. \end{aligned} \tag{6.23}$$

Observe that (6.23) does not distinguish between graylevels other than if they are the same or different. Let $\mathbf{w}$ be an n-vector of 1's, and let $\mathbf{D}$ be a diagonal $n \times n$ matrix of the self-aura measures. Then the objective function to be maximized is alternatively written as

$$\beta\,[3\mathbf{w}^T\mathbf{D}\mathbf{w} - 2\mathbf{w}^T\mathbf{A}\mathbf{w}]. \tag{6.24}$$

6.4.1 Attractive case

Suppose $\beta = 1$ in (6.24). Then we want to minimize $\mathbf{w}^T\mathbf{A}\mathbf{w}$ and maximize $\mathbf{w}^T\mathbf{D}\mathbf{w}$. Clearly the aura matrix will try to become diagonal, maximizing the self-aura measures.

This is the same boundary minimization problem as the auto-binomial case with the exception of the ordering influence of the different graylevels. In other words, even if the aura matrix $\mathbf{A}$ is normalized and decomposed into permutations all the permutations would have the same effect on the energy. Consequently, no permutations are favored for the cross-aura measures. The resulting aura matrix structure is diagonally dominant with uniformly distributed off-diagonal elements.

Notice that if the histogram is not constrained for the Potts energy then the lattice will become unicolor – one element along the aura matrix will dominate, and the rest of the matrix will become zero.

6.4.2 Repulsive case

Suppose $\beta = -1$ in (6.24). Then the goal is to maximize $\mathbf{w}^T\mathbf{A}\mathbf{w}$ and minimize $\mathbf{w}^T\mathbf{D}\mathbf{w}$. For this case $\mathbf{w}^T\mathbf{D}\mathbf{w}$ can usually be driven to zero without violating the

irreducibility of the aura matrix. The resulting aura matrix structure has zeros along the main diagonal with the remainder of the values uniformly distributed along the off-diagonals.

6.4.3 Anisotropic case

The anisotropic Potts case can be obtained from the isotropic cases by examining the energy minimization over the subneighborhoods. Let $\mathbf{D}^k$ be a diagonal $n \times n$ matrix of the self-aura measures over the subneighborhood $\mathcal{N}_s^k$. Then the objective function to be maximized is

$$\sum_{k=1}^{K} \beta_k [3\mathbf{w}^T \mathbf{D}^k \mathbf{w} - 2\mathbf{w}^T \mathbf{A}^k \mathbf{w}]. \tag{6.25}$$

Again, because of the linearity of the energy and the disjointness of the subneighborhoods, the positive and negative terms can be optimized individually. For each direction k, if $\beta_k > 0$ then the synthesis will try to maximize the elements along the diagonal and if $\beta_k < 0$ then it will try to zero the elements along the diagonal.

6.5 Long range implications

These new results on aura structure have important consequences for texture formation. The ground state aura matrix characterize the large scale structure, and the sharpening process introduces zeros in the aura matrix which restrict certain colors from being neighbors.

6.5.1 Restrictions on texture patterns

For the case of tridiagonal structure and $n > 2$, elements of $\mathbf{A}$ that satisfy $|i-j| > 1$ will be zero. This implies that textures in the ground states cannot have any mixing among graylevels g, g' when $|g - g'| > 1$. For the case of anti-tridiagonal structure textures in the ground states cannot have any mixing between graylevels g and $n - 1 - g'$ when $|g - g'| > 1$. For the Potts matrices in the repulsive case, no

two elements of the same color can be neighbors. These are serious restrictions for a texture model!

For anisotropic models, when the ground state aura matrix consists of a linear combination of tridiagonal and anti-tridiagonal matrices and $n \geq 5$, then the aura measures $m(i,j)$ and $m(i,n-1-j)$ with $|i-j| > 1$ will be forced to be zero. This can seriously limit texture patterns formed by energy minimization of MRF's. Patterns are prohibited from having colors g, g' interact, when g and g' are not indices of either a tridiagonal or an anti-tridiagonal element.

The sharpening process which happens throughout the temperature annealing gradually restricts the space of feasible textures. Even as the matrices are *becoming* tridiagonal or anti-tridiagonal (i.e., not yet in their ground states) their intermediate banded structures will restrict pattern formation. This is where knowing transition temperatures is important – these temperatures control these regions of pattern behavior.

We have seen that the ground state structure results in a global pattern unlike the random looking samples usually associated with MRF texture models. Although we can apply the "formula" of Section 6.3.3 to characterize the pattern, the pattern will not be unique. The assumption of the periodic lattice implies that the same pattern could occur in NM different positions. Because the low energy patterns do not really look like a "texture," i.e., they do not look visually similar when translated, these different translations can look like quite different patterns. Nonetheless, the aura matrix will be the same for all these translations.

6.5.2 Implications for co-occurrence structure

In surveys of texture analysis, Haralick [29], Wechsler [68], and Van Gool *et. al.* [66] discuss both co-occurrence matrices and random field methods. Van Gool *et. al.* basically summarize the understanding of the structure of co-occurrence matrices by noting that if the displacement is small relative to the texture coarseness the matrix values cluster near the main diagonal, while for larger displacements, the values are more spread out. None of the surveys recognize any connection between MRF's and

co-occurrences.

The aura matrix establishes the first known link between a texture model and the structure of its co-occurrence matrix. By showing the MRF energy is completely characterized by the aura matrix, we have shown that it is completely characterized by the corresponding set of co-occurrences. Since co-occurrence and MRF aura matrices have only nonnegative elements and the aura matrix is a sum of co-occurrence matrices, then a zero in the aura matrix implies corresponding zeros in the co-occurrence matrices. By showing the structure in the MRF ground state aura matrices, we have shown corresponding structure in the co-occurrence matrices.

Chapter 7

Conclusions

The goal of this thesis was to explore and characterize the effects of temperature on texture synthesized with a Markov/Gibbs random field (MRF). Although MRF's had been studied elsewhere for texture modeling, the influence of temperature on the texture had not been studied. Since the temperature is varied in many applications of MRF's to image processing and computer vision our study of these effects is important.

7.1 Texture characterization – aura matrix and physical behavior

At all temperatures greater than zero all patterns are possible. However, some are more likely than others. Characterizing the patterns is the first hurdle. To do this, in Chapter 3 we introduced a notational framework based on a new local neighborhood concept, the aura set. The aura set allows the traditionally separate tools of co-occurrences, morphological dilation, and random fields to be united in one notational framework. Through applying this new framework, we have established new links between these different tools.

This framework also led to a new tool, the aura matrix. The new aura matrix generalizes the co-occurrence matrix – a popular texture analysis tool. The anisotropic

aura matrix completely specifies the Gibbs energy; thus, the MRF can be completely specified by the set of co-occurrences which comprise the aura-matrix. This is a key new result relating MRF and co-occurrence texture analysis methods.

We showed that the aura matrix is comprised of elements which have physical interpretations as "miscibilities," i.e., how much each graylevel will "mix" with each other graylevel. These physical interpretations augment the traditional texture properties associated with the co-occurrence matrix. The behavior of the aura matrix elements was also shown to be related to the physical behavior of surface minimization, hypothesized to be an important component of natural texture formation.

The connections established between the MRF and its surface/boundary minimization behavior are new for the MRF. In the physics literature they also appear to be the first generalization of the boundary length characterization of the first order binary Ising model of statistical mechanics to any order or number of graylevels.

7.2 Temperature and texture bonding parameters

Previously it has been assumed that the bonding parameters of the MRF represent the texture that it forms. In Chapter 4 we illustrated that this is true in part, but not as previously implied in the literature. We reformulated the Gibbs energy function to show that the bonding parameters play the same role as the temperature annealing rate constant. This gives a new interpretation of pattern formation: the pattern emerges as energy is minimized at different rates in different directions.

This interpretation of pattern formation was also shown to be significant because it pointed to the importance of non-equilibrium pattern formation. In particular, examples were shown where the ground state may be the same for an anisotropic and an isotropic pattern, but the intermediate pattern formation is quite distinct.

Using the Gibbs energy and properties of the aura matrix, we characterized the equilibrium and long-term behaviors of the auto-binomial MRF for different temperatures. This demonstrated that most texture patterns shown in the literature have not

been in equilibrium. We also showed that there exists a plateau at both high and low temperatures where the temperature cannot be uniquely determined. The new features also reflect the existence of a transition region where properties are monotonic with respect to temperature.

7.3 Transition temperatures

The idea of critical temperature has immense importance in physical pattern formation; it delimits the regions of different phases, or for textures, different textures. In analogy to the critical temperature for an infinite system, in Chapter 5 we introduced the idea of transition temperature for a finite texture. We showed that the transition temperature for a binary texture can be determined by measuring the specific heat of the field.

We showed some problems with the specific heat method for graylevel textures, and suggested an adaptive normalizing term to help in some cases. We observed that the aura bandwidth changes occur during the peak of the specific heat, and proposed that these changes might correspond to $n-1$ transition temperatures for a n graylevel texture. Physical justification, via an analogy to crystallization, was given for the distinct behaviors of the MRF between the different transition temperatures. The temperatures mark the events where the miscibilities undergo discontinuous changes, and are thus a new way of providing "control" over the texture formation.

7.4 Ground state patterns

When the temperature goes to zero and the field is in equilibrium only one pattern is possible: the ground state. An exact solution for this state is in general an extremely difficult nonlinear integer optimization problem. By exploiting the new aura matrices, we performed what we believe is the first characterization of these ground state textures.

The characterization, given in Chapter 6, follows from the structure of the aura

matrix as the Gibbs energy is minimized. The ground state aura matrix structure was derived analytically by decomposing the aura matrix into a convex combination of permutation matrices. Under certain conditions this structure forces zeros in the aura matrices which imply severe limitations for the ground state patterns of the MRF model. These implications are new and important for image modeling. We have also shown that these ground states do not look like the kinds of stochastic textures generally associated with random field models.

Via the relationship between aura matrices and co-occurrence matrices, these results also give the first analytic connection between ground state MRF's and their co-occurrence texture features.

7.5 Non-minimum energy texture formation

Often MRF's are used as priors in Bayesian optimization where the aim is to minimize a cost function which includes the texture energy. Our results imply that the current method of minimizing energy forms only a limited number of interesting natural looking textures.

We discussed some ways around this problem. One way is to carefully constrain the problem to avoid these ground states which restrict texture formation. We have mentioned analogies to this problem in natural pattern formation such as on gel surfaces – the "interesting" patterns form at states which are non-equilibrium and/or constrained away from minimum energy.

We have also shown that synthesizing at a constant temperature at or above the transition region can give different kinds of non-minimum energy patterns. Features of the aura matrix, especially its bandwidth structure for the auto-binomial model, can characterize the current state of the pattern. These features provide an index into the temperature region most likely to synthesize such a texture.

Chapter 8

Future research suggestions

8.1 Introduction

In the world of possible texture models we have restricted our research to random field methods and in particular, to studying the role of temperature in the Markov/Gibbs random field (MRF). Although we have made some new strides in characterizing the behavior of these models, there is still much to learn about texture modeling.

8.2 Markov/Gibbs model and relation to other models

There are a lot of texture models and many more textures to be modeled, but there is still relatively little understanding of which models are best for which class of textures. As part of an effort to "unify" the field we suggest exploration of more of the model equivalences, as we have tried to do by relating MRF's, co-occurrences, and morphological dilation. The aim should be to try to determine where there is model overlap that is wasteful and/or advantageous.

The MRF has been shown to be "structurally and probabilistically" equivalent to a regular grammar [46]. Grammars have been studied quite a bit for production

of textures involving primitives and rules of organization [24]. It is possible that the regular grammar equivalence might give some additional hooks into the MRF to control pattern formation and vice-versa.

There are relationships between non-causal auto-regressive models and MRF's that under certain conditions allow you to go back and forth between the two models [71, 33]. In many applications random fields have been implemented as auto-regressive models. In some cases we have found that stochastic noise filtering methods can produce the same patterns as the MRF with vastly fewer computations. In the other direction, one might expect that certain MRF behaviors might lead to interesting behaviors with their difference equation counterparts. A preliminary investigation also suggests that there might be some interesting relationships between stability of the auto-regressive model and singularity of the partition function.

8.3 Energy minimization

It is still an open question how best to choose the energy function of the MRF. This is the same open problem that occurs in optimization when one trys to formulate the right objective function.

Because of the similarity in many different patterns in nature, it is plausible that there exists some fundamental set of primitive "control knobs" that can be used to adjust different pattern forming mechanisms, and hence with which to construct an energy function.

In Chapter 3 we tried to illustrate that the basic mechanism working in the minimization of the auto-MRF energy is a boundary minimization or maximization (depending on the sign), giving the appearance of separation or mixing. This mixing or separation can be controlled by the temperature. This is one plausible mechanism; however, the problem of finding the full set of mechanisms, and the energy function to represent them, is still open.

The MRF energy function is flexible and can take many forms. For example, the finite element shape primitives of Terzopoulos [62] can be incorporated, letting clique

potentials function as the relative weights of gradient terms. Geman and Geman [27] used a line process to constrain boundary length. Srolovitz *et. al.* [58] add a finite element elastic term to the energy of a next-nearest neighbor Ising model to study the influence of an externally applied stress.

Returning to the gel analogy, the following energy function is proposed by Tanaka *et. al.* [61] for the surface pattern deformation. Let the vertical axis be z, and the surface fluctuation be $\Delta z = w(x, y, z)$. The lower surface of the gel is assumed to be constrained mechanically to a square slab, having value $w = 0$ at $z = 0$ and maximum value $w(x, y)$ at $z = h$, the height of the gel. The mechanical potential energy of the gel with this deformation is given by

$$V = \int\int\int \frac{1}{2}\left\{\frac{Ez^2}{9}[\Delta w]^2 - P[\nabla w]^2 + E\frac{w^2}{h^2}\right\} \mathrm{d}\mathbf{r} \quad . \tag{8.1}$$

This energy has three terms corresponding to three hypothesized mechanisms. The first term is the bending energy, the second represents the energy of compression, and the third represents the energy due to local vertical stretching.

Pattern constraints

We suggest that the choice of *constraints* of the system may be even more important for pattern formation than the actual choice of energy.[1] Finding these kinds of constraints is at the heart of what Stevens [59] summarizes,

> We thus see that the specific mechanism that brings a pattern or form into being is not as important to its overall appearance as how its constituent parts relate in space: if the parts are free to adjust and find equilibrium, they arrange themselves in a configuration of minimum energy.

If the lattice is large enough for the MRF ground state patterns to occur, then they will have predictable forms that are generally uninteresting, at least for the auto-binomial model. However, it was the earlier non-minimum energy, and sometimes the

[1] Note that the constraints may be incorporated directly into the energy via penalty methods, so the distinction between energy function and constraints can be weakened.

non-equilibrium patterns that looked like a greater variety of natural textures. The important question then is "what is the set of constraints that makes these patterns the solution to the problem?"

The gel can be kept from its equilibrium patternless state by externally constraining the system. A pea losing water will shrivel only because its surface area is not allowed to shrink. To get water in a bathtub to go to a highly ordered vortex requires a drain, a boundary condition. Thaxton *et. al.* [63] emphasize the importance of boundary conditions to constrain a system away from equilibrium so that ordered structure is formed. In Murray's essay on why the leopard has spots [47], the combination of reaction (against different boundary conditions) with diffusion is considered as the mechanism for pattern formation.

We think much future work needs to be done on understanding and incorporating constraints into these energy minimization models. Exploration of the model on generalized grids and in 3-D space, free from the rectangular lattice constraints should also prove interesting.

8.4 Non-equilibrium temperature

The use of temperature in this thesis was restricted to systems assumed to be in thermal equilibrium without a temperature gradient. In natural patterns regions with greater surface area tend to cool faster. It would be interesting to add this capability to the model to see if an MRF is able to reproduce the growth that occurs in these non-equilibrium conditions. It may also be interesting to explore differences in melting and freezing points which have been associated with clusters in materials, and the effect of increasing distance between hot and cold regions to simulate convection and introduce order.

The relation of temperature to correlation is important in materials studies. For example, correlation has been used to study order-disorder transitions in spinodal decomposition of binary alloys and to identify structure such as bicontinuity, which describes the existence of a connected path from one side of the lattice to the other

[11]. This type of property, plus the development of the MRF on a general graph, could lead to interesting developments for graph theoretic problems.

Theoretically the MRF is independent of the initial state; nonetheless, Garand and Weinman [26] were able to put structure into their cloud models by incorporating low frequency Fourier components in the initial state of their MRF's. We believe temperature is the agent in results such as these. It would be interesting to characterize the conditions under which this initial state structure technique can be used.

8.5 Temperature and parameter estimation

Although this was not the topic of this thesis, it is clearer after our characterization of temperature why this nonlinear problem is so difficult. We have showed in isotropic cases how the behavior divides into different temperature regions marked by transition temperatures, and that the temperature is unique in only some of these regions.

It would be interesting to explore a constant energy Monte Carlo sampling algorithm such as the microcanonical method of Creutz [15] for purposes of estimating temperature. This method employs a demon that keeps the energy level constant by traveling around on the lattice, giving and taking bits of energy needed for flipping in such a way as to keep the total energy constant. The temperature of the field can be determined from the average energy the demon carries. We would expect these results to confirm the temperatures we found at which the energy leveled off for different graylevels.

8.6 Ground state patterns

The results on ground state structure in Chapter 6 depend on the lattice being large enough to allow the minimum energy configuration. It is an open question how to characterize the configurations when this condition is not met. It is also undetermined how different assumptions on the lattice boundary conditions will affect

these configurations.

8.7 Structural textures

When the external field is nonhomogeneous, one can show that the maximization of $P(\mathbf{x})$ tries to match the external field to the values on the lattice. The relative weights of the external and internal fields can be adjusted for enhancing or mitigating these external influences.

We have investigated some of these tradeoffs and found that the external field can be used to put structure into the texture. However, because it functions as a matching process, it does not appear to put any structure into the texture that is not already in the external field. What would be more interesting would be to investigate external influences that create flow, turbulence, and other ordering phenomenon.

Appendix A

Permutation theory

A.1 Permutations, cycles, transpositions

A *permutation* of the vector $\mathbf{g} = [0, 1, \ldots, n-1]^T$ gives a rearrangement of its elements.

Example A.1 *The vector* $\mathbf{g} = [0, 1, 2, 3, 4]^T$ *permuted by* $\sigma_1 = (3, 1, 0)$ *is represented by the product of the* permutation matrix $\mathbf{P}_{\sigma_1}$ *with* $\mathbf{g}$, $\mathbf{P}_{\sigma_1}\mathbf{g} =$

$$\begin{bmatrix} 0 & 0 & 0 & 1 & 0 \\ 1 & 0 & 0 & 0 & 0 \\ 0 & 0 & 1 & 0 & 0 \\ 0 & 1 & 0 & 0 & 0 \\ 0 & 0 & 0 & 0 & 1 \end{bmatrix} \begin{bmatrix} 0 \\ 1 \\ 2 \\ 3 \\ 4 \end{bmatrix} = \begin{bmatrix} 3 \\ 0 \\ 2 \\ 1 \\ 4 \end{bmatrix}.$$

The permutation σ_1 is also a *cycle* of length 3; it can equivalently be written as $(3, 1, 0) = (0, 3, 1) = (1, 0, 3)$. It is a well known result in algebra [31] that any permutation can be written as a product of its disjoint cycles.

Example A.2 *The permutation*

$$\mathbf{P}_{\sigma_2} = \begin{bmatrix} 0 & 0 & 1 & 0 & 0 \\ 0 & 1 & 0 & 0 & 0 \\ 1 & 0 & 0 & 0 & 0 \\ 0 & 0 & 0 & 0 & 1 \\ 0 & 0 & 0 & 1 & 0 \end{bmatrix},$$

can be written as the product of its disjoint cycles,

$$\sigma_2 = (0,2)(3,4).$$

In Example A.2 the cycles are called *transpositions* because they have length 2. The cycle $(3,4)$ is also an *adjacent transposition* since it transposes two elements $j, j+1$.

If the cycles are not disjoint then they are applied from right to left.

Example A.3 *Let σ_1 and σ_2 be the same as in Examples A.1 and A.2. Applying the new permutation $\sigma_3 = \sigma_2\sigma_1$ to $\mathbf{g}$ yields,*

$$\begin{aligned} \mathbf{P}_{\sigma_2}\mathbf{P}_{\sigma_1}\mathbf{g} &= \mathbf{P}_{\sigma_2}[3,0,2,1,4]^T \\ &= [2,0,3,4,1]^T. \end{aligned}$$

A.2 Proof of Proposition 6.4

The following three lemmas appeared first in [51]. These are used to prove Proposition 6.4 in Chapter 6. Recall the following definition of the *mismatch* of a permutation σ,

$$\mu(\sigma) = \mathbf{g}^T\mathbf{g} - \mathbf{g}^T\mathbf{P}_\sigma\mathbf{g},$$

where $\mathbf{g} = [0, 1, \ldots, n-1]$ and $\mathbf{P}_\sigma$ is the matrix which performs the permutation σ.

Lemma A.4 *Let $\sigma \in \mathcal{P}_\tau$ be an adjacent transposition. Then*

$$\mu(\sigma) = 1.$$

Proof: Assume that σ exchanges the adjacent elements $j, j+1 \in \Lambda$. Then its mismatch

$$\begin{aligned}
\mu(\sigma) &= \sum_{i=0}^{n-1} [i^2 - i\sigma(i)] \\
&= \sum_{i \in \{j,j+1\}} [i^2 - i\sigma(i)] + \sum_{i \in \Lambda - \{j,j+1\}} [i^2 - i\sigma(i)] \\
&= j^2 - j(j+1) + (j+1)^2 - (j+1)j \\
&= (j - (j+1))^2 \\
&= 1.
\end{aligned}$$

■

Is there any other permutation that has a mismatch this small? The answer is no, and comes from the next two lemmas by Elfadel. The first lemma gives a lower bound on the mismatch associated with a cycle that is not an adjacent transposition. The second shows that the mismatch of a permutation will be the sum of the mismatches of its cycles.

Lemma A.5 *Let $\sigma \in \mathcal{P}_n - \mathcal{P}_\tau^*$ be a cycle of length l. Then*

$$\mu(\sigma) \geq l. \tag{A.1}$$

Proof: The proof is by induction on the length. First, assume that σ has $l = 2$ but is not adjacent. Let $j, k \in \Lambda$, with $|j - k| \geq 2$. Then

$$\begin{aligned}
\mu(\sigma) &= \sum_{i=0}^{n-1} [i^2 - i\sigma(i)] \\
&= \sum_{i \in \{j,k\}} [i^2 - i\sigma(i)] + \sum_{i \in \Lambda - \{j,k\}} [i^2 - i\sigma(i)] \\
&= j^2 - jk + k^2 - kj \\
&= (j - k)^2
\end{aligned}$$

$$\geq 4.$$

Next, consider the two possible arrangements for cycles having $l = 3$: $\sigma_1 = (i, j, k)$ and $\sigma_2 = (i, k, j)$. Then

$$\begin{aligned}
\mu(\sigma_1) &= i^2 - ij + j^2 - jk + k^2 - ki \\
&= \frac{1}{2}[(i-j)^2 + (j-k)^2 + (k-i)^2] \\
&\geq 3,
\end{aligned}$$

and

$$\begin{aligned}
\mu(\sigma_2) &= i^2 - ik + k^2 - kj + j^2 - ji \\
&= \frac{1}{2}[(i-k)^2 + (k-j)^2 + (j-i)^2] \\
&\geq 3,
\end{aligned}$$

so (A.1) is true for $l = 2, 3$.

Finally, assume that (A.1) is true for length $l \geq 3$, and show that it is true for length $l+1$. Let σ have length $l+1$. We can always shift the cycle until its maximum element is written in the last position, $\sigma = (i_0, i_1, \ldots, i_l)$, where $i_l = \max\{i_0, i_1, \ldots, i_l\}$. Now, form the l-length cycle, $\sigma' = (i_0, i_1, \ldots, i_{l-1})$. By the induction assumption, $\mu(\sigma') \geq l$. But

$$\begin{aligned}
\mu(\sigma) &= \sum_{j=0}^{l}[i_j^2 - i_j\sigma(i_j)] \\
&= \sum_{j=0}^{l-2}[i_j^2 - i_j\sigma(i_j)] + [i_{l-1}^2 - i_{l-1}i_l] + [i_l^2 - i_l i_0] \\
&= \sum_{j=0}^{l-2}[i_j^2 - i_j\sigma(i_j)] + [i_{l-1}^2 - i_{l-1}i_0] + i_{l-1}i_0 - i_{l-1}i_l + [i_l^2 - i_l i_0] \\
&= \sum_{j=0}^{l-1}[i_j^2 - i_j\sigma'(i_j)] + i_l^2 - i_l i_0 - i_{l-1}i_1 + i_{l-1}i_0 \\
&= \mu(\sigma') + (i_l - i_{l-1})(i_l - i_0) \\
&\geq l + 2 > l + 1.
\end{aligned}$$

■

Lemma A.6 *Let $\sigma = \sigma_1 \ldots \sigma_k$ be the decomposition of the permutation σ into its disjoint cycles. Then*

$$\mu(\sigma) = \sum_{j=1}^{k} \mu(\sigma_j).$$

Proof: Let Λ_j be the set of elements permuted by cycle σ_j. Since the cycles are disjoint the Λ_j form a partition of Λ. When $i \in \Lambda_j$, $\sigma(i) = \sigma_j(i)$ and when $i \in \Lambda - \Lambda_j$, $\sigma(i) = i$. Thus,

$$\begin{aligned}
\mu(\sigma) &= \sum_{i \in \Lambda} [i^2 - i\sigma(i)] \\
&= \sum_{j=1}^{k} \sum_{i \in \Lambda_j} [i^2 - i\sigma_j(i)] \\
&= \sum_{j=1}^{k} \sum_{i \in \Lambda} [i^2 - i\sigma_j(i)] \\
&= \sum_{j=1}^{k} \mu(\sigma_j).
\end{aligned}$$

■

From Lemma A.6, the bound on the permutation $\mu(\sigma)$ will come from the sum of the bounds on its disjoint cycles. From Lemma A.4, each of the t adjacent transpositions contributes a mismatch of 1, and from Lemma A.5, the other k cycles contribute mismatches which are at least their lengths, l_j. Thus, the statement given in Proposition 6.4 follows.

Bibliography

[1] E. H. Adelson and J. R. Bergen. The plenoptic function and the elements of early vision. In M. Landy and J. A. Movshon, editors, *Computational Models of Visual Processing*. M.I.T. Press, (In Press 1991).

[2] R. J. Baxter. *Exactly Solved Models in Statistical Mechanics*. Academic Press, Inc., London, 1982.

[3] E. Ben-Jacob and P. Garik. The formation of patterns in non-equilibrium growth. *Nature*, 343(6258):523–530, 1990.

[4] J. R. Berry, Jr. and J. Goutsias. A comparative study of matrix measures for maximum likelihood texture classification. *IEEE Trans. Systems, Man, and Cybernetics*, 21:252–261, 1991.

[5] J. Besag. Spatial interaction and the statistical analysis of lattice systems (with discussion). *J. Royal Statistical Society, series B*, 36:192–236, 1974.

[6] C. Bouman and B. Liu. Multiple resolution segmentation of textured images. *IEEE Trans. Pattern Analysis and Machine Intell.*, PAMI-13(2):99–113, 1991.

[7] C. D. Bunks. *Random field modeling for interpretation and analysis of layered data*. PhD thesis, M.I.T., 1987.

[8] P. Carnevali, L Coletti, and S. Patarnello. Image processing by simulated annealing. In M. A. Fischler and O. Firschein, editors, *Proc. in Computer Vision*. Morgan Kaufmann, 1987.

[9] R. Chellappa. "Two-dimensional discrete Gaussian Markov random field models for image processing". In L. N. Kanal and A. Rosenfeld, editors, *Progress in Pattern Recognition 2*. Elsevier Science Publishers B. V. (North Holland), 1985.

[10] R. Chellappa and S. Chatterjee. Classification of textures using Markov random field models. In *Proc. ICASSP*, pages 32.9.1–32.9.4, San Diego, 1984.

[11] S-H. Chen, S-L. Chang, and R. Strey. Simulation of bicontinuous microemulsions: Comparison of simulated real space microstructures with scattering experiments. *J. Appl. Crystallography*, Oct. 1991. To appear.

[12] F. Cohen and D. Cooper. Simple parallel hierarchical and relaxation algorithms for segmenting noncausal Markovian random fields. *IEEE Trans. Pattern Analysis and Machine Intell.*, PAMI-9(2):195–219, 1987.

[13] F. S. Cohen, Z. Fan, and M. A. Patel. Classification of rotated and scaled textured images using Gaussian Markov random field models. *IEEE Trans. Pattern Analysis and Machine Intell.*, PAMI-13(2):192–202, 1991.

[14] R. W. Conners and C. A. Harlow. A theoretical comparison of texture algorithms. *IEEE Trans. Pattern Analysis and Machine Intell.*, PAMI-2(3):204–222, 1980.

[15] M. Creutz. Microcanonical Monte Carlo simulation. *Phys. Rev. Letters*, 50(19):1411–1414, 1983.

[16] G. R. Cross. *Markov Random Field Texture Models.* PhD thesis, Michigan State University, 1980.

[17] G. R. Cross and A. K. Jain. Markov random field texture models. *IEEE Trans. Pattern Analysis and Machine Intell.*, PAMI-5(1):25–39, 1983.

[18] L. S. Davis, S. A. Johns, and J. K. Aggarwal. Texture analysis using generalized co-occurrence matrices. *IEEE Trans. Pattern Analysis and Machine Intell.*, PAMI-1(3):251–259, 1979.

[19] H. Derin and H. Elliott. Modeling and segmentation of noisy and textured images using Gibbs random fields. *IEEE Trans. Pattern Analysis and Machine Intell.*, PAMI-9(1):39–55, 1987.

[20] R. C. Dubes and A. K. Jain. Random field models in image analysis. *Journal of Applied Statistics*, 16(2):131–163, 1989.

[21] I. M. Elfadel and R. W. Picard. Miscibility matrices explain the behavior of grayscale textures generated by Gibbs random fields. In *Proc. SPIE Conference on Intelligent Robots and Computer Vision*, Boston, MA, Nov. 1990.

[22] I. M. Elfadel and R. W. Picard. Auras Part I: Theory and relation to morphology and co-occurrence. Vision and Modeling Group TR #149, M.I.T. Media Laboratory, Feb. 1991.

[23] P. A. Flinn. Monte Carlo calculation of phase separation in a two-dimensional Ising system. *J. of Statistical Physics*, 10(1):89–97, 1972.

[24] K. S. Fu. *Syntactic Methods in Pattern Recognition.* Academic Press, Inc., New York, 1974.

[25] E. B. Gamble, D. Geiger, T. Poggio, and D. Weinshall. Integration of vision modules and labeling of surface discontinuities. *IEEE Trans. Systems, Man, and Cybernetics*, 19(6):1576–1581, 1989.

[26] L. Garand and J. A. Weinman. A structural-stochastic model for the analysis and synthesis of cloud images. *J. of Climate and Applied Meteorology*, 25:1052–1068, 1986.

[27] S. Geman and D. Geman. Stochastic relaxation, Gibbs distributions, and the Bayesian restoration of images. *IEEE Trans. Pattern Analysis and Machine Intell.*, PAMI-6(6):721–741, 1984.

[28] C. C. Gotlieb and H. E. Kreyszig. Texture descriptors based on co-occurrence matrices. *Computer Vision, Graphics, and Image Process.*, 51:70–86, 1990.

[29] R. Haralick. Statistical and structural approaches to texture. *Proc. of the IEEE*, 67:786–804, May 1979.

[30] M. Hassner and J. Sklansky. The use of Markov random fields as models of texture. *Computer Graphics and Image Process.*, 12:357–370, 1980.

[31] I. M. Herstein. *Topics in Algebra.* Wiley, New York, 1975.

[32] E. Ising. Beitrag zur theorie des ferromagnetismus. *Zeitschrift Physik*, 31:253–258, 1925.

[33] A. K. Jain. *Fundamentals of Digital Image Processing.* Prentice Hall, New Jersey, 1989.

[34] F.-C. Jeng and J. W. Woods. Compound Gauss-Markov random fields for estimation. *IEEE Trans. Acoustics, Speech, and Signal Process.*, pages 683–697, March 1991.

[35] B. Julesz. Visual pattern discrimination. *Proc. of IRE*, 8(2):84–92, 1962.

[36] R. Kindermann and J. L. Snell. *Markov Random Fields and their Applications.* American Mathematical Society, Providence, Rhode Island, 1980.

[37] S. Kirkpatrick, C. D. Gelatt, Jr., and M. P. Vecchi. Optimization by simulated annealing. *Science*, 220(4598):671–680, 1983.

[38] W. M. Lawton and M. Lee. Random field models for use in scene segmentation. Technical report, Jet Propulsion Laboratory, March 1985.

[39] J. E. Lay. *Thermodynamics.* C. E. Merrill Books, Inc., Columbus, Ohio, 1963.

[40] B. B. Mandelbrot. *The Fractal Geometry of Nature.* W. H. Freeman and Company, New York, 1983.

[41] P. A. Maragos and R. W. Schafer. Morphological systems for multidimensional signal processing. *Proc. of the IEEE*, pages 690–710, April 1990.

[42] J. L. Marroquin. *Probabilistic Solution of Inverse Problems.* PhD thesis, M.I.T., 1985.

[43] J. L. Marroquin, S. Mitter, and T. Poggio. Probabilistic solution of ill-posed problems in computational vision. *J. of the American Statistical Association*, 82:76–89, 1987.

[44] W. L. Masterton and E. J. Slowinski. *Chemical Principles.* W. B. Saunders Co., Philadelphia, 1977.

[45] N. Metropolis, A. Rosenbluth, M. Rosenbluth, A. Teller, and E. Teller. Equation of state calculations by fast computing machines. *J. of Chemical Physics*, 21(6):1087–1092, 1953.

[46] M. Miller, B. Roysam, K. Smith, and J. Udding. On the equivalence of regular grammars and stochastic constraints: Applications to image processing on massively parallel processors. In *AMS-IMS-SIAM Joint Conf. on Spatial Statistics and Imaging*, American Mathematical Society, July 1988.

[47] J. D. Murray. How the leopard gets its spots. *Scientific American*, 258(3):80–87, March 1988.

[48] L. Onsager. Crystal statistics I. A two-dimensional model with an order-disorder transition. *Physical Review*, 65:117–149, 1944.

[49] S. Peleg, J. Naor, R. Hartley, and D. Avnir. Multiple resolution texture analysis and classification. *IEEE Trans. Pattern Analysis and Machine Intell.*, PAMI-6(4):518–523, 1984.

[50] A. P. Pentland. Fractal-based description of natural scenes. *IEEE Trans. Pattern Analysis and Machine Intell.*, PAMI-6(6):661–674, 1984.

[51] R. W. Picard and I. M. Elfadel. On the structure of optimal aura matrices. Vision and Modeling Group TR #160, M.I.T. Media Laboratory, Feb. 1991.

[52] R. W. Picard, I. M. Elfadel, and A. P. Pentland. Markov/Gibbs texture modeling: Aura matrices and temperature effects. In *Proc. IEEE Conference on Computer Vision and Pattern Recognition*, Maui, HI, June 1991.

[53] D. K. Pickard. Inference for discrete Markov fields: the simplest nontrivial case. *J. of the American Statistical Association*, 82(397):90–96, 1987.

[54] A. Rosenfeld, R. A. Hummel, and S. W. Zucker. Scene labeling by relaxation operations. *IEEE Trans. Systems, Man, and Cybernetics*, SMC-6(6):420–433, 1976.

[55] A. Rosenfeld and A. C. Kak. *Digital Picture Processing, Volume 2.* Academic Press, Inc., Orlando, 1982.

[56] D. H. Rothman and J. M. Keller. Immiscible cellular-automaton fluids. *J. of Statistical Physics*, 52(3/4):1119–1127, 1988.

[57] F. Spitzer. Markov random fields and Gibbs ensembles. *American Mathematics Monthly*, 78:142–154, 1971.

[58] D. J. Srolovitz, G. N. Hassold, and J. Gayda. Monte Carlo simulation of modulated phases. In S. Komura and H. Furukawa, editors, *Dynamics of Ordering Processes in Condensed Matter*. Plenum, NY, 1988.

[59] P. S. Stevens. *Patterns in Nature*. Little, Brown and Co., Boston, MA, 1974.

[60] G. Strang. *Introduction to Applied Mathematics*. Wellesley-Cambridge Press, Cambridge, MA, 1986.

[61] T. Tanaka, S-T. Sun, Y. Hirokawa, S. Katayama, J. Kucera, Y. Hirose, and T. Amiya. Mechanical instability of gels at the phase transition. *Nature*, 325(6107):796–798, 1987.

[62] D. Terzopoulos. The computation of visible-surface representations. *IEEE Trans. Pattern Analysis and Machine Intell.*, PAMI-10(4):417–438, 1988.

[63] C. B. Thaxton, W. L. Bradley, and R. L. Olsen. *The Mystery of Life's Origin*. Philosoph. Lib., New York, 1984.

[64] C. W. Therrien. An estimation-theoretic approach to terrain image segmentation. *Computer Vision, Graphics, and Image Processing*, 22:313–326, 1983.

[65] D. E. Van Den Bout and T. K. Miller, III. Graph partitioning using annealed neural networks. *IEEE Trans. Neural Networks*, 1(2):192–203, 1990.

[66] L. Van Gool, P. Dewaele, and A. Oosterlinck. Texture analysis anno 1983. *Computer Vision, Graphics, and Image Processing*, 29:336–357, 1985.

[67] A. L. Vickers and J. W. Modestino. A maximum likelihood approach to texture classification. *IEEE Trans. Pattern Analysis and Machine Intell.*, PAMI-4(1):61–68, 1982.

[68] H. Wechsler. Texture analysis – a survey. *Signal Processing*, 2(3):271–282, 1980.

[69] T. A. Witten. Structured fluids. *Physics Today*, 43(7):21–28, 1990.

[70] Chee Sun Won. *Unsupervised Segmentation of Noisy and Textured Images Modelled with Gibbs Random Fields*. PhD thesis, Univ. of Mass., 1990.

[71] J. W. Woods. Two-dimensional discrete Markovian fields. *IEEE Trans. Information Theory*, IT-18(2):232–240, 1972.

[72] F. Y. Wu. The Potts model. *Reviews of Modern Physics*, 54:235–268, 1982.

[73] S. W. Zucker and D. Terzopoulos. Finding structure in co-occurrence matrices for texture analysis. *Computer Vision, Graphics, and Image Process.*, 12:286–308, 1980.